



Terms and Conditions of Use of Digitised Theses from Trinity College Library Dublin

Copyright statement

All material supplied by Trinity College Library is protected by copyright (under the Copyright and Related Rights Act, 2000 as amended) and other relevant Intellectual Property Rights. By accessing and using a Digitised Thesis from Trinity College Library you acknowledge that all Intellectual Property Rights in any Works supplied are the sole and exclusive property of the copyright and/or other IPR holder. Specific copyright holders may not be explicitly identified. Use of materials from other sources within a thesis should not be construed as a claim over them.

A non-exclusive, non-transferable licence is hereby granted to those using or reproducing, in whole or in part, the material for valid purposes, providing the copyright owners are acknowledged using the normal conventions. Where specific permission to use material is required, this is identified and such permission must be sought from the copyright holder or agency cited.

Liability statement

By using a Digitised Thesis, I accept that Trinity College Dublin bears no legal responsibility for the accuracy, legality or comprehensiveness of materials contained within the thesis, and that Trinity College Dublin accepts no liability for indirect, consequential, or incidental, damages or losses arising from use of the thesis for whatever reason. Information located in a thesis may be subject to specific use constraints, details of which may not be explicitly described. It is the responsibility of potential and actual users to be aware of such constraints and to abide by them. By making use of material from a digitised thesis, you accept these copyright and disclaimer provisions. Where it is brought to the attention of Trinity College Library that there may be a breach of copyright or other restraint, it is the policy to withdraw or take down access to a thesis while the issue is being resolved.

Access Agreement

By using a Digitised Thesis from Trinity College Library you are bound by the following Terms & Conditions. Please read them carefully.

I have read and I understand the following statement: All material supplied via a Digitised Thesis from Trinity College Library is protected by copyright and other intellectual property rights, and duplication or sale of all or part of any of a thesis is not permitted, except that material may be duplicated by you for your research use or for educational purposes in electronic or print form providing the copyright owners are acknowledged using the normal conventions. You must obtain permission for any other use. Electronic or print copies may not be offered, whether for sale or otherwise to anyone. This copy has been supplied on the understanding that it is copyright material and that no quotation from the thesis may be published without proper acknowledgement.

Instrumentation and Techniques In Confocal Microscopy

By

Aaron Mac Raighne

A thesis submitted for the degree of Doctor of Philosophy at the University of

Dublin Trinity College

School of Physics

Trinity College Dublin

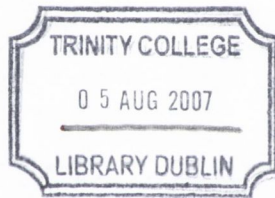
University of Dublin

Dublin 2.



October

2006



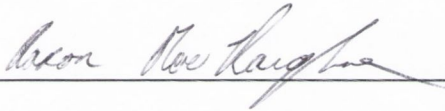
THESIS

8132

Declaration

This thesis has not been submitted as an exercise for a degree at any other University. The work described is entirely my own, except for the assistance mentioned in the acknowledgements and the collaborative work noted in the list of publications. I agree that Trinity College Library may lend or copy this thesis on request.

Aaron Mac Raighne.



Abstract

Liquid crystal variable focal length microlenses are designed, fabricated and tested for inclusion into the confocal system. Their emerging light fields are imaged and examined. This proves a novel, efficient and thorough examination of the optical properties, the results of which are compared to those found using interferometric methods. The aberrations present are noted and possible causes discussed. It is also found that by increasing the driving frequency of the applied voltage across the liquid crystal lenses the optical performance can be enhanced by up to 30%, allowing diffraction-limited microlenses to be achievable at greater focal length ranges. The inclusion of these lenses as a high throughput aperture array with a fibre bundle as the corresponding pinhole array at the detector is experimentally investigated. The use of the microlens arrays as an array of objective lenses is also discussed and the depth discriminating properties examined by use of the axial response. The fibre bundle is shown to be an efficient pinhole array and an imaging conduit in confocal systems. The mapping of the entrance and exit positions of an incoherent fibre bundles is undertaken for the proposed application as a pinhole and image conduit. Using fluorescent confocal and conventional microscopy, defect analysis and the size determination of dye-doped melamine formaldehyde microspheres by spectral analysis is performed. High contrast confocal fluorescent lifetime imaging of gold nanoparticles by novel sample preparation is examined and the possible uses of this technique in the future discussed.

List of Publications

“Emerging light fields from liquid crystal microlenses”

Aaron Mac Raighne, Toralf Scharf and Eithne Mc Cabe. Review of scientific instruments Vol. 77, 055103, 2006.

“Confocal microscopy using variable-focal-length microlenses and an optical fiber bundle.”

Lisong Yang, **Aaron Mac Raighne**, Eithne Mc Cabe, L. Andrea Dunbar and Toralf Scharf. Applied Optics Vol. 44, 28, pg. 59287, 2005.

“Variable focal length microlenses for confocal microscopy.”

Aaron Mac Raighne, Jiangang Wang, Eithne Mc Cabe and Toralf Scharf. Proc. SPIE Vol. 5860, p. 74-80, Confocal, Multiphoton, and Nonlinear Microscopic Imaging II, 2005.

“Variable-focus microlenses: Issues for confocal microscopy.”

Aaron Mac Raighne, Jiangang Wang, Eithne Mc Cabe and Toralf Scharf. Proc. SPIE Vol. 5827, p. 12-22, Opto-Ireland 2005: Photonic Engineering

“Variable-focal-length microlens arrays in confocal microscopy”

Aaron Mac Raighne, Jiangang Wang, Eithne Mc Cabe and Toralf Scharf. Proc. SPIE Vol. 5701, p. 93-100, Three-Dimensional and Multidimensional Microscopy: Image Acquisition and Processing XII.

“Confocal microscopy and variable-focal-length microlenses”

Aaron Mac Raighne, Lisong Yang, L. Andrea Dunbar, Eithne Mc Cabe and Toralf Scharf. Proc. SPIE Vol. 5324, p. 55-64, Three-Dimensional and Multidimensional Microscopy: Image Acquisition and Processing XI.

“Three dimensional confocal microscopy of fluorescent microspheres: imaging and size determination”

Yury Rakovich, Lisong Yang, Cian Taylor, Andrea. Dunbar, **Aaron Mac Raighne**, John Donegan, Eithne Mc Cabe. Proc. SPIE Vol. 5827, p. 299-304, Opto-Ireland, 2005.

“Imaging of Quenched Luminescence of Quantum Dots by Nanostructured Gold Nanoparticles.”

Aaron Mac Raighne, Yury Rakovich and Eithne Mc Cabe. Photon 06, Online Proceedings, <http://www.photon06.org/QEP%20P2.6.pdf>

Acknowledgements

The work done in this thesis would not be possible without the help and encouragement from many people.

First and foremost I would like to thank my family for all their support and help in getting me to this position. I would also like to thank Edel for all her support during my studies and in particular for putting up with me when writing up my thesis.

I would like to thank Professor Eithne McCabe for all her support, direction and encouragement over the years. I would also like to thank Science Foundation Ireland, Enterprise Ireland and Trinity College Dublin for the financial support without which this research could not have been carried out.

I would also like to thank all the staff and students in the School of Physics; you have helped and taught me so much during my studies in Trinity. I am indebted to you all.

I have made many friends during my studies and would like to thank them all for all the fun we had and the impromptu brain storming sessions to help me solve the many problems that arose during a PhD.

Oh, and cheers Denis.

Contents

CHAPTER 1.....	9
INTRODUCTION.....	9
1.1 A short history of microscopy.....	9
1.2 High resolution microscopy.....	10
1.3 Scanning optical microscopy and three dimensional imaging.....	13
1.4 Far-field optical imaging techniques.....	16
1.5 Areas of research addressed in this thesis.....	19
CHAPTER 2.....	21
BASIC THEORY AND EQUATIONS.....	21
2.1 Propagation of an optical wavefront through space.....	21
2.2 Propagation of an optical wavefront through a thin lens.....	23
2.2 Coherent Imaging with a single lens.....	26
2.5 Imaging in the confocal microscope.....	29
2.7 Summary.....	33
CHAPTER 3. LIQUID CRYSTAL VARIABLE FOCAL LENGTH LENS SYSTEMS.....	34
3.1 Introduction: Variable focal length systems.....	34
3.2 Liquid crystal variable focal length lenses.....	38
3.3 Fabrication.....	39
3.4 Experimental set-up and theory.....	41
3.5 Optical characterization.....	47
3.6 Increase in optical quality by control of the frequency of driving voltage.....	54
3.7 Conclusions.....	59
CHAPTER 4.....	63
APPLICATION OF VARIABLE FOCAL LENGTH SYSTEMS TO THE CONFOCAL MICROSCOPE SYSTEM.....	63
4.1 Introduction.....	63
4.2 VFL microlens arrays as high throughput aperture arrays with fibre optical bundle.....	65
4.21 Fibre bundle characterisation.....	65
4.22 Fibre bundle coupling with VFL microlens array.....	68
4.23 Confocal system with VFL lens array and fibre bundle.....	75
4.3 VFL microlens arrays as an array of objective lenses.....	78
4.4 Conclusions.....	86
CHAPTER 5.....	88
IMAGING AND SIZE DETERMINATION OF A SPHERICAL MICROCAVITY BY CONFOCAL FLOURECENCE MICROSCOPY.....	88
5.1 Introduction.....	88
5.2 Background and theory.....	90
5.3 Experimental set-up.....	94
5.4 Confocal Imaging.....	96

5.5 Spectral analysis and size determination.....	98
5.6 Conclusions.....	109
CHAPTER 6.....	111
IMAGING WITH INCOHERENT FIBER BUNDLES.....	111
6.1 Introduction.....	111
6.1.1 <i>Imaging bundles</i>	112
6.1.2 <i>Fabrication</i>	113
6.1.3 <i>Imaging with incoherent bundles</i>	114
6.2 Fibre bundle mapping.....	115
6.3 Image reconstruction.....	118
6.4 Conclusions.....	120
CHAPTER 7.....	122
F.L.I.M CONFOCAL MICROSCOPY ON MODIFIED FLOURESCENCE OF QUANTUM DOTS.....	122
7.1 Introduction and background.....	122
7.2 Experimental set-up.....	125
7.3 Sample Preparation.....	126
7.3.1 <i>Gold nanoparticle preparation</i>	126
7.3.2 <i>Sample preparation for F.L.I.M. imaging</i>	127
7.4 Confocal F.L.I.M.....	129
7.6 Discussion and Future work.....	133
CHAPTER 8.....	136
CONCLUSIONS.....	136
APPENDIX A.....	141
APPENDIX B.....	143
APPENDIX C.....	146
Section A1.....	146
Section A2.....	150
Section A3.....	152
REFERENCES.....	155

CHAPTER 1

Introduction

1.1 A short history of microscopy

The lens or the simple magnifier has been in use for many years with Aristophanes referring to ‘burning glasses’ in a play written *circa* 400 B.C.¹. The invention of the first compound microscope is now commonly given to the spectacle makers, Zaccharias Janssen and son Hans Janssen, in the Netherlands between the years 1590 and 1610. The compound microscope created a great deal of excitement when the English physicist Robert Hooke began making detailed analysis of structures as seen through his compound microscope. The results of these observations were tabulated in *Micrographia*, the first book describing observations as made through the microscope. This ability to see new structures invisible to the naked eye was a revelation to scientists however the compound microscope was limited in its performance by chromatic aberrations. The most powerful microscope of the time was the simple magnifier as built by Van Leeuwenhoek who placed the samples under investigation on a pin point close to small beads of glass through which he viewed his samples. It was not until the 18th century that the compound microscope overtook the resolving power of the single lens microscope. This came about by the discovery that the careful placement of lenses in the optical path could correct the chromatic effects.

In the 1870s Carl Zeiss employed the help of Prof. Ernst Abbe of the University of Jena to try to understand some of the physical parameters of microscopes. It was during this time that Abbe formed the well known limiting law of diffractive imaging that bears his name. By

studying the imaging of periodic gratings with different lenses he noted that the minimum resolvable distance, d , was

$$d = \frac{\lambda}{2N.A.}$$

Where λ is the wavelength transmitted through the objective. In a point of interest he was also the first to coin the term numerical aperture N.A. for the value $n\sin\theta$ where n is the refractive index and θ is the angle of acceptance of light of the lens. Reaching and indeed breaking this limit has become the interest of modern high resolution microscopy.

1.2 High resolution microscopy

Abbe's limit has been over-come using light with the Near-Field Scanning Optical Microscope (NSOM). This microscope places a sub-wavelength aperture at sub-wavelength distances from the sample surface. The possibility to perform such imaging was first recognised by John Aloysius O'Keefe in 1955² He proposed that if a sample is brought close to an aperture, the sample will block the light emitting from the aperture; if this sample is laterally scanned the near-field microscope can resolve dimensions down to that of the aperture diameter. O'Keefe recognised that this set-up would mean that the optical microscope would be able to resolve with powers far greater than that given by Abbe but also noted the difficulty of moving the sample in such small dimensions when it is so close to the aperture. These difficulties have been overcome and the NSOM is now implemented³ with a view to single molecule imaging³. The use of NSOM has made it necessary to describe two different types of optical microscopy,

that of near-field and far-field. Near-field is when the sample is placed within a wavelength distance of the imaging optics, where diffraction is negated. Far-field microscopy utilises diffraction as a form of image formation. The resolution is much increased over far-field optical microscopes and the effects of photobleaching are also reduced³. The trade-off that come with the NSOM are the small sample sizes that can be imaged, the complexity of the set-up and also the fact the sample height variation must be quite small.

Another form of microscopy closely related to that of NSOM is atomic force microscopy (AFM) and scanning tunnelling microscopy (STM). They are similar in that a very fine probe is scanned across the surface of the sample and the interaction at minute distances can be monitored. In STM the tunnelling current is measured across a fine tip and a metallic sample. In AFM a fine tipped probe is moved across a surface and the interacting forces, electric or mechanical, between the surface and the probe are measured which allows the measurement of non-metallic samples⁴.

Another type of high resolution microscope, the electron microscope focuses accelerated electrons rather than light. The de Broglie wavelength of the electrons can be as small as 0.005 nm and is easily controllable by an acceleration voltage of typically 50-100 kV. Presently, electron microscopes are limited by spherical aberrations rather than by the wavelength⁵, somewhat resembling the situation of the light microscope in the mid of the 19th century. Transmission electron microscopes (TEM) can attain resolutions of typically 10nm but the sample must be kept quite thin, typically 10 to 100nm so that the electrons do not slow down appreciably⁴. Using the scanning electron microscope (SEM) imaging is performed by

detecting what are commonly called secondary electrons, which are emitted from the surface of the sample. Thus it is possible to image the surface of bulk objects. The resolution is typically an order of magnitude lower than in TEM.

The imaging resolution of the probe scanning near-field techniques and the electron microscope is far greater than that achieved by far-field techniques. So what advantages do the far-field optical microscopes have over their near-field counterparts? There are inherent drawbacks with the use of the techniques described above. The electron microscopes need strict sample preparation technique where the samples must be dehydrated and placed in a vacuum. This excludes the investigation of living cells. In TEM the samples must be kept quite thin whereas in SEM non-conducting samples must be coated by a metallic layer. Scanning probe microscopes are considered slow and the scanning tip can be difficult to control. In addition, the interpretation of the image is not straightforward, for example in STM a high degree of knowledge of the sample must be known to interpret the results of the scan. The most striking drawback of electron and scanning probe microscopes, however, is that they are restricted to investigations on the specimen surface⁶. The interior of an intact specimen is accessible to neither of them. This is particularly serious in biomedical research, for in most of biomedical applications it is less exciting to investigate the specimen surface, as compared to the interior. The most attractive feature of a far-field light microscope is its ability to gather information from the inside of the specimen. Focused light can penetrate translucent specimens without harming them. It has also proved useful in all areas of research and industry where non-invasive depth discrimination is required. Therefore the optical microscope will remain an integral part of scientific research across the board.

1.3 Scanning optical microscopy and three dimensional imaging

A far-field scanning optical microscope was first described by Young and Roberts with their flying spot microscope. Here a tiny spot of light was raster scanned over the sample and any radiation transmitted through the sample was collected by a photocell and the results displayed on a TV display⁷. This allowed a range of sample sizes to be imaged with a constant variable magnification. It also allowed the digital storage of the image and made for easier processing, for example contrast enhancement.

In 1955 Marvin Minsky was studying neurons and the nervous system⁸. In particular he wanted to map the cells in the central nervous system and study their interconnections. The central nervous system was so densely packed and interwoven with cells that it was impossible for Minsky to image the cells with any microscope that was available to him. Minsky's greatest challenge was the scattering of light in his sample, unless the view could be confined to a very thin plane he would see a meaningless blur with a low signal to noise ratio. In an attempt to resolve this problem Minsky designed a microscope that would investigate the light scattered or absorbed by a single point only. To achieve this goal a pinhole was placed in front of the sample to exclude all rays of light from the source not initially aimed at the focal point under investigation. Unfortunately, some of the initially focused light was scattered by out-of-focus specimen points onto other points in the image plane. This was solved when using a second pinhole aperture which was placed in the image plane that lies beyond the exit side of the objective lens whose focus was made to meet the same position on the sample as the probe objective lens, thus they were considered 'confocal'. The resulting optical set-up is shown schematically in Figure 1.1.

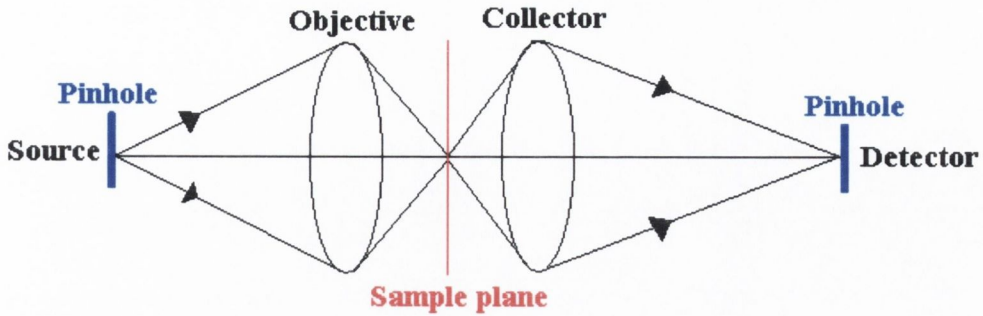


Figure 1.1 Schematic diagram of the confocal set-up in transmission mode.

With the insertion of the pinholes into the microscope a bright light source was required. Minsky used the brightest source available to him, the carbon-arc lamp, and a military surplus radarscope as a detector. The radarscope displayed the image for approximately 10 seconds, the same length that it took for one single scan in the lateral direction. Thus the first confocal microscope was born. Although the images were not digitally stored as Minsky felt the time for a scan to be made was more important than the exposure time needed to store the images, the microscope had all the advantages of the scanning optical microscopes. There were also some very important improvements made by the introduction of the pinholes and the 'confocal' arrangement. Due to the introduction of the pinholes the lateral resolution was increased beyond that of the conventional microscope as both lenses played equal roles in the imaging, this will be discussed in Chapter 2. Arguably the most important result was the axial resolution made possible by the rejection of out-of-focus light. This is shown schematically in Figure 1.2 for the reflected type confocal microscope. The reflected-light confocal microscope is similar to the transmission type shown above in Figure 1.1 except that the one lens now plays dual roles and the inclusion of a beam splitter is necessary for the detection of the reflected light.

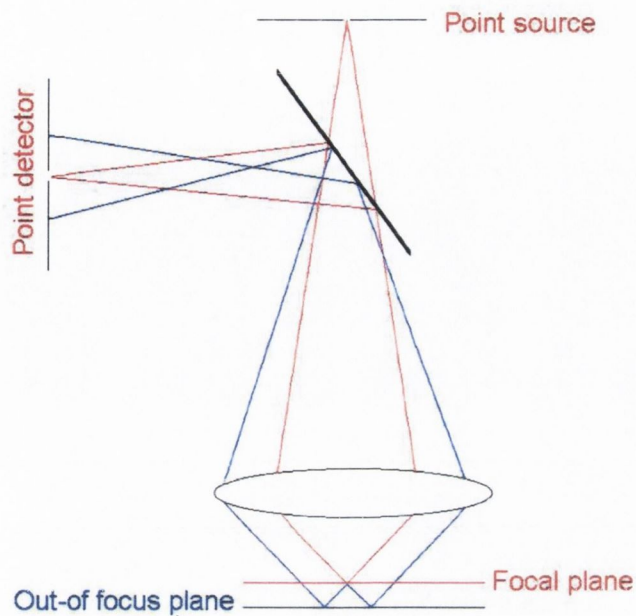


Figure 1.2 Schematic diagram showing the origins of optical sectioning

The light emitted from outside the focal point is largely rejected by the detection pinhole whereas the light reflected from the focal point is focussed to the pinhole. A large signal results from the in-focus plane. This allows thin sections from within a translucent sample to be viewed with high resolution. This is called optical sectioning and is a non-invasive procedure which can image the sample in 3D if a number of lateral scans are done at different axial positions inside the sample. Minsky was performing fluorescence confocal microscopy staining his sample with a fluorescent dye. This confocal microscope can be used also for transmittance and reflected light. With the invention of the laser and illumination of the sample with sufficiently high intensities the confocal microscope became indispensable to biomedical imaging and also found uses in most areas of research where the depth discrimination and increased lateral resolution of the microscope was required.

1.4 Far-field optical imaging techniques

Other far-field optical imaging techniques have been demonstrated since the invention of the confocal microscope and I will briefly summarise them in this section. I will initially describe techniques that have become useful for high resolution 3D imaging and then will briefly mention some other techniques including one which has broken the Abbe limit in the far-field using fluorescent diffraction imaging.

The importance of imaging inside samples is paramount to the ever increasing diagnosis and treatment of illness by medical staff across the globe. This is evident with the now widespread use of ultrasound, magnetic resonance imaging and positron emission tomography in hospitals and clinics everywhere the technology can be afforded. These imaging processes have great depth of penetration but very low resolution compared to light microscopy. The highest resolution is attainable with computed tomography and with ultrasound, where there is a trade-off between depth of penetration and resolution. A limit of $\sim 10\mu\text{m}$ resolution is attainable with $\sim 1\text{mm}$ depth of penetration with ultrasound imaging techniques. If resolutions greater than this are required optical techniques are necessary. A relatively new form of imaging, optical coherence microscopy (OCT) can image with axial resolution with an order of magnitude greater than ultrasound and with penetration depths of between that of confocal microscopy and ultrasound imaging. The OCT scanner uses a Michelson interferometer which is illuminated by a low coherence source. The sample is placed in one arm of the interferometer and a reference mirror is placed in the other arm⁹. By scanning the mirror and reading the resulting interferogram information on the reflections from inside the sample can

be read. Interferometric signal is detected when only when the reflections from the sample and reference arm of the interferometer are nearly matched in time-of-flight. This leads to a high resolution in the axial position of the reflection in the sample⁹. Lateral images can be brought about by the scanning of the beam in the directions perpendicular to the optical axis, but resolutions are quite low. It has proven useful to combine confocal imaging with OCT for regions where the depth of penetration of confocal imaging can match the OCT imaging such as in ophthalmology¹⁰. I would like to point out at this point that although confocal microscopy and optical sectioning has become important to bio-medical imaging it has also been useful in many different areas of industry and research.

Optical sectioning is also possible with a technique known as two-photon microscopy¹¹. Two-photon microscopy relies on the fact that with certain high intensities of light the fluorophore can absorb two photons and reach a highly excited state. The molecule in the excited state has a high probability of emitting a photon during relaxation to the ground state. Due to vibrational energies of the molecules the fluorescence is usually of a longer wavelength. The high intensities necessary for multi-absorption are found with high power pulsed lasers. The absorption process is dependant of the square of the intensity of the illuminating pulse which falls off sharply away for the focal point of the illuminated light on the sample, which is in contrast to single photon absorption microscopy where the process is linear. This compares with the linear relation between intensity and absorption of a single photon, therefore the intensity of the fluorescence is contained to a small volume around the focal point which gives a three dimensional imaging capability to the technique. The quadratic relationship between absorption and light intensity also reduces the amount of photobleaching in the sample¹¹. The

main drawbacks encountered with two-photon microscopy are the costs of the pulsed lasers and the optical components required. Due to the high intensities of the illuminating light fields special optical components are required.

Confocal microscopy is commonly used with fluorescence, as with its original application by Minsky⁸. Fluorescence microscopy is carried out by determining the different spectral intensities from the fluorophores present in a sample and their spatial displacement. But each fluorophore can also be characterised by its fluorescence lifetime, which is an intrinsic property of the fluorophore and not dependant on its concentration in the sample¹². Therefore fluorescent lifetime imaging (FLIM) is a powerful technique and can be used in conjunction with many other techniques, in particular with fluorescence intensity imaging and confocal microscopy, as will be discussed in some detail in Chapter 7. The interaction of fluorophores with their environment leads to a change in lifetime which is the basis for fluorescent energy transfer or FRET microscopy. Here two or more fluorophore markers are used, where their emission and excitation spectra overlap. In this case the energy from the first fluorophore goes directly into the second fluorophore, known as the donor and acceptor fluorophores respectively. This is a very effective quenching mechanism that is highly dependant on the distance between the donor and acceptor molecules. These markers and the fluorescence captured by the microscopical set-up can give quantitative information as to the relative positions of the markers from each other.

As I mentioned at the beginning of this section there has been a technique demonstrated in fluorescence far-field microscopy which has surpassed Abbe's limit of diffraction. This is

known as stimulated-emission-depletion fluorescence microscopy or STED microscopy. It was noticed that the resolution of the microscope is determined by the size of the point of light which illuminates the sample and therefore the region in which excitation and fluorescence can occur. By limiting the size of this spot of light, or the point spread function as it is called, (see Chapter 2), the resolution can be increased. The size of the spot incident on the sample can no longer be decreased as it is limited by diffraction, but the size of the spot allowed to fluoresce can be varied. A laser separate to that of the excitation laser is focused to an annular pattern around the edge of the excitation spot. This overlaps with the excitation spot leaving a smaller spot in the centre undisturbed by this second laser. The second laser stimulates emission of the excited states before the samples can fluoresce. Therefore the centre of the spot which is undisturbed by the second laser is free to fluoresce. As only information from this section is collected the resolution has been enhanced.

1.5 Areas of research addressed in this thesis

The use of variable focal length (VFL) microlens arrays in the confocal set-up is investigated. The inclusion of microlenses is investigated as high throughput aperture arrays in Section 4.22, these can form an array of virtual pinholes into which a vast amount of the light incident on the array is focused. The use of pinhole arrays is commonly used to decrease the time needed for lateral scans and to approach real-time imaging, the most successful being the tandem-scanning microscope⁷. There is vast light loss due to the nature of these pinholes which can be addressed by the use of microlens array. The use of a fibre bundle as a pinhole array in conjunction with these microlenses is also investigated in Section 4.23. VFL

microlenses as arrays of objective lenses are studied in Section 4.3. The integration of these lenses into the system allows for the opportunity to axial scan the sample controlled electronically and without moving parts. The lenses used are characterized in Chapter 3, giving the most in depth investigation into the optical properties these type of lenses to date, to the author's knowledge. This is done by the novel method of imaging their emergent light fields in the region of the focal point and is used to observe the aberrations present in the lenses. A method found to improve the optical performance of these lenses is also found.

The mapping of the fibres in a light guide is undertaken with a view to using these fibre bundles as imaging guides. This would greatly decrease the cost of imaging bundles and perhaps become useful in single-use fibre bundles for confocal endoscopes that will become available in the future.

The versatility of the confocal technique is also investigated in Chapter 5 and Chapter 7. In Chapter 5 the confocal imaging is combined with fluorescence spectroscopy to determine the size of a spherical micro-cavity by the fitting of spectral data to theoretical models. In Chapter 7 the first steps into a promising study in the use of confocal FLIM imaging for surface plasmon supporting structures is described.

CHAPTER 2

BASIC THEORY AND EQUATIONS

In this chapter a basic outline is given as to the origin of the equations that are commonly used in describing confocal systems and will come to be used in this thesis. As this is an outline the reader is referred to the texts “Theory and Practice of Scanning Optical Microscopy”⁷ and “Principles of Optics”¹³ for a full approach to the derivation of these equations.

2.1 Propagation of an optical wavefront through space

The Huygens-Fresnel principle states that every unobstructed point of a wavefront, at any given instant, serves as a source of spherical secondary wavelets. The amplitude of the optical field at any point beyond is the superposition of all these wavelets at that point¹. When dealing with paraxial optics this theory can be stated in terms of a scalar field amplitude, this is known as Kirchoff’s diffraction formula, which can be written as,

$$U_2(x_2, y_2) = \int \int_{-\infty}^{+\infty} \frac{1}{j\lambda R} U_1(x_1, y_1) \exp(-jkR) dx_1 dy_1 \quad \text{Eqn. 2.1}$$

Here $U_2(x_2, y_2)$ is the optical wavefront at the position (x_2, y_2) shown in Figure 2.1. Where the exponential term divided by R describes spherical waves of amplitude U_1 arising from positions, (x_1, y_1) . The double integrals shows that U_2 is the summation of all the described propagating secondary wavelets from position (x_1, y_1) . Here k is the wavenumber, λ is the wavelength and R is the distance between the optical disturbance at (x_1, y_1) and (x_2, y_2) as shown in the Figure 2.1.

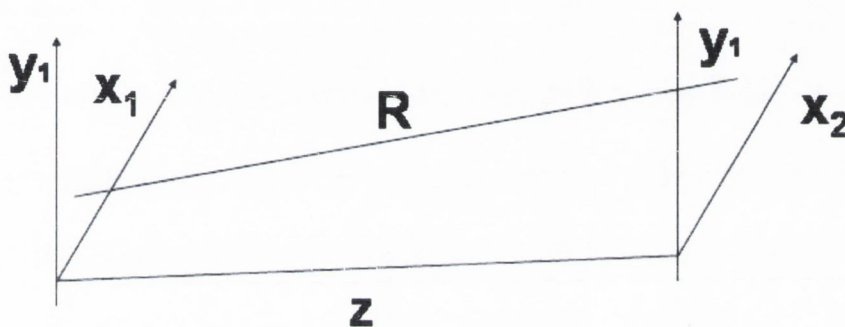


Figure 2.1: Schematic to show the origins and propagation path of the light.

The distance, R , can be described in terms of the coordinates by $R^2 = z^2 + (x_2 - x_1)^2 + (y_2 - y_1)^2$, here it is assumed that $z^2 \gg (x_2 - x_1)^2 + (y_2 - y_1)^2$, thus using the first two values from the binomial expansion of R we can rewrite the propagation of light in terms of the positions of the point in space,

$$U_2(x_2, y_2) = \frac{\exp(-jkz)}{j\lambda z} \int_{-\infty}^{+\infty} \int_{-\infty}^{+\infty} U_1(x_1, y_1) \exp \frac{-jk}{2z} \left\{ (x_2 - x_1)^2 + (y_2 - y_1)^2 \right\} dx_1 dy_1 \quad \text{Eqn. 2.2}$$

This equation is of paramount importance as it is used to describe the propagation of light between object, lens and image space throughout the chapter.

2.2 Propagation of an optical wavefront through a thin lens

A lens placed in the optical path of the propagating wave is accounted for by the addition of a pupil function, $P(x_2, y_2)$ to Equation 2.2. This accounts for the finite size of the lens aperture which has a value of unity when inside the radius, r , and a value of the zero outside. This is regarded as an aberration free lens as the optical quality of a lens is described by the integration of aberration functions into that of the pupil function.

$$P(x, y) = \begin{cases} 1, & \sqrt{x^2 + y^2} \leq r \\ 0, & \text{otherwise} \end{cases} \quad \text{Eqn. 2.3}$$

The light also undergoes a phase change when passing through the lens such that spherical waves will propagate from the lens to converge on a point a distance, f , away. Therefore the transmittance function of the lens can be given by this phase change and the pupil function.

$$t(x, y) = P(x, y) \exp \frac{jk}{2f} (x^2 + y^2) \quad \text{Eqn. 2.4}$$

The transmittance gives the amplitude of light after the lens if it is illuminated by a uniform plane wave. To calculate the amplitude incident on a screen, $U_2(x_2, y_2)$, a distance removed from the lens Equation 2.2 is used.

$$U_2(x_2, y_2) = \frac{\exp(-jkz)}{j\lambda z} \int_{-\infty}^{+\infty} \int_{-\infty}^{+\infty} P(x_1, y_1) \exp \frac{jk}{2f} (x_1^2 + y_1^2) \exp \frac{-jk}{2z} \left\{ (x_2 - x_1)^2 + (y_2 - y_1)^2 \right\} dx_1 dy_1 \quad \text{Eqn. 2.5}$$

Rearranging this equation it can be given as

$$U_2(x_2, y_2) = \frac{\exp(-jkz)}{j\lambda z} \int_{-\infty}^{+\infty} \int_{-\infty}^{+\infty} P(x_1, y_1) \exp \frac{jk}{2} (x_1^2 + y_1^2) \left(\frac{1}{f} - \frac{1}{z} \right) \exp \frac{jk}{2z} (x_2^2 + y_2^2) \exp \frac{jk}{z} (x_2 x_1 + y_2 y_1) dx_1 dy_1 \quad \text{Eqn. 2.6}$$

When the observation plane is made to coincide with the focal plane the exponential containing the terms in the object plane becomes unity and the image is an aberration free image. Otherwise there is aberration in the image due to defocus. For a circularly symmetrical lens Equation 2.6 can be rewritten in terms of a Bessel or Hankel transform¹⁴

$$U_2(x_2, y_2) = \frac{\exp(-jkz)}{j\lambda z} \exp \left(\frac{-jkr_1^2}{2z} \right) \int_0^{\infty} P(r) \exp \frac{jkr_1^2}{2} \left(\frac{1}{f} - \frac{1}{z} \right) J_0 \left(\frac{2\pi r_1 r_2}{\lambda z} \right) 2\pi r_1 dr_1 \quad \text{Eqn. 2.7}$$

Here the $r_1 = x_1^2 + y_1^2$ and

$$P(r) \exp \frac{jk r_1^2}{2} \left(\frac{1}{f} - \frac{1}{z} \right) \quad \text{Eqn. 2.8}$$

is the defocused pupil function. The entire integral is the radial Fourier transform of the pupil function. This is called the amplitude point spread function of the lens. Using the normalised optical coordinates given as

$$u = ka^2 \left(\frac{1}{f} - \frac{1}{z} \right) \quad \text{Eqn. 2.9}$$

$$v = \frac{2\pi r_2 a}{\lambda f} \quad \text{Eqn. 2.10}$$

Equation 2.7 can be rewritten as

$$U_2(u, v) = -jN \exp(-jkz) \exp\left(\frac{-jv^2}{4N}\right) \int_0^1 2 \exp\left(\frac{1}{2} jup^2\right) J_0(vp) p dp \quad \text{Eqn. 2.11}$$

Here a is the radius of the lens outside of which the pupil function is zero, $p = r_1/a$ and $N = \pi a^2 / \lambda f$. The intensity along the lateral and axial directions through the focal spot can be given by the relationships.

$$I(v, 0) = \left[\frac{2J_1(v)}{v} \right]^2 \quad \text{Eqn. 2.12}$$

and

$$I(0, u) = N^2 \left[\frac{\sin(u/4)}{u/4} \right]^2 \quad \text{Eqn. 2.13}$$

In Equation 2.12 the first exponential term in Equation 2.11 is negligible due to the fact that the Fresnel number is large in most cases which means that $N \gg v^2/4$ and the multiplication terms are neglected when the intensity is normalized to 1. Outside of the axial positions the intensity is given by

$$I(u, v) = N^2 [C^2(u, v) + S^2(u, v)] \quad \text{Eqn. 2.14}$$

where

$$\begin{aligned} C(u, v) &= \int_0^1 2 \cos\left(\frac{1}{2} ju\rho^2\right) J_0(v\rho) \rho d\rho, \\ S(u, v) &= \int_0^1 2 \sin\left(\frac{1}{2} ju\rho^2\right) J_0(v\rho) \rho d\rho \end{aligned} \quad \text{Eqn. 2.15}$$

2.2 Coherent Imaging with a single lens

We now consider the set-up shown in Figure 2.2 where a thin object of transmittance $t(x, y)$, when illuminated with a plane wave of unit strength, is placed at the object position denoted by (x_1, y_1) is placed a distance d_1 behind the lens of the lens and observed at a distance d_2 in front of the lens.

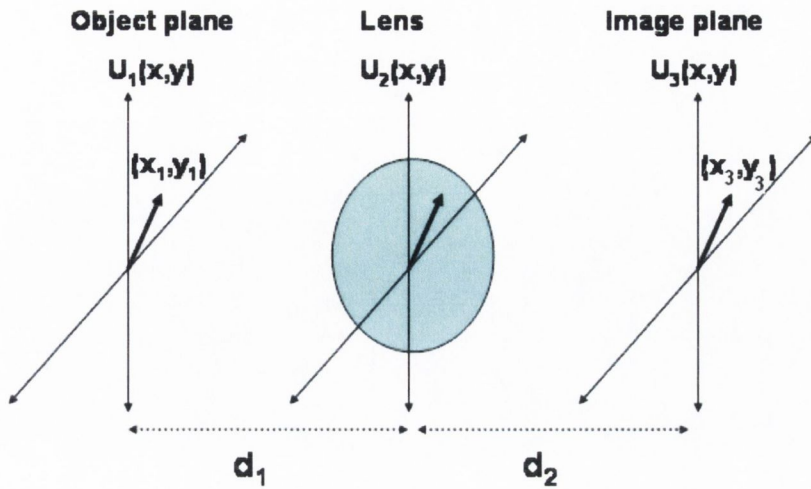


Figure 2.2. Schematic of simple optical system

The amplitude at the observation plane is given as

$$\begin{aligned}
 U_3(x_3, y_3) = & \frac{\exp(jk(d_1 + d_2))}{\lambda^2 d_1 d_2} \iint \int_{-\infty}^{+\infty} P(x_2, y_2) t(x_1, y_1) \\
 & \exp\left\{ \frac{-jk}{2d_1} \left[(x_2 - x_1)^2 + (y_2 - y_1)^2 \right] \right\} \\
 & \exp\left\{ \frac{-jk}{2d_2} \left[(x_3 - x_2)^2 + (y_3 - y_2)^2 \right] \right\} \\
 & \exp\left\{ \frac{jk}{2f} (x_2^2 + y_2^2) \right\} dx_1 dy_1 dx_2 dy_2
 \end{aligned}
 \tag{Eqn. 2.16}$$

The second and the third line of the equation respectively and the premultiplying factor describe the propagation of the wave through the distances d_1 and d_2 . The final exponential function accounts for the phase change produced by the lens. Rearranging Equation 2.17 we get

$$\begin{aligned}
U_3(x_3, y_3) &= \frac{\exp(jk(d_1 + d_2))}{\lambda^2 d_1 d_2} \iint \int_{-\infty}^{+\infty} P(x_2, y_2) t(x_1, y_1) \\
&\quad \exp \frac{-jk}{2d_1} (x_1^2 + y_1^2) \exp \frac{-jk}{2d_2} (x_3^2 + y_3^2) \\
&\quad \exp \frac{jk}{2} \left[\frac{jk}{2} (x_2^2 + y_2^2) \left(\frac{1}{f} - \frac{1}{d_2} - \frac{1}{d_1} \right) \right] \\
&\quad \exp jk \left[x_2 \left(\frac{x_1}{d_1} + \frac{x_3}{d_2} \right) + y_2 \left(\frac{y_1}{d_1} + \frac{y_3}{d_2} \right) \right] dx_1 dy_1 dx_2 dy_2
\end{aligned}
\tag{Eqn. 2.17}$$

Using the well known relation for the magnification $M = d_2/d_1$ and using the term, d_0 , for the defocus given by the equation.

$$\frac{1}{f} - \frac{1}{d_2} - \frac{1}{d_1} = -\frac{1}{d_0}
\tag{Eqn. 2.18}$$

Equation 2.17 can now be written as

$$\begin{aligned}
U_3(x_3, y_3) &= \frac{\exp(jk(d_1 + d_2))}{\lambda^2 d_1 d_2} \exp \frac{-jk}{2d_1 M} (x_3^2 + y_3^2) \\
&\quad \int_{-\infty}^{+\infty} \int_{-\infty}^{+\infty} h' \left(x_1 + \frac{x_3}{M}, y_1 + \frac{y_3}{M} \right) t(x_1, y_1) \exp \frac{-jk}{2d_1} (x_1^2 + y_1^2) dx_1 dy_1
\end{aligned}
\tag{Eqn. 2.19}$$

Here $h(x, y)$ is the APSF and is given by the Fourier transform of the effective pupil function

$$h' \left(x_1 + \frac{x_3}{M}, y_1 + \frac{y_3}{M} \right) = \iint \int \int_{-\infty}^{+\infty} P(x_2, y_2) t(x_1, y_1) \exp \frac{-jk}{2d_0} (x_2^2 + y_2^2) \exp \frac{jk}{d_1} \left[x_2 \left(x_1 + \frac{x_3}{M} \right) + y_2 \left(y_1 + \frac{y_3}{M} \right) \right] dx_2 dy_2 \quad \text{Eqn. 2.20}$$

Here the importance of the APSF can be seen. If the object is a point source the transmittance is given by $t(x_1, y_1) = \delta(x_1)\delta(y_1)$ then the image is given by a constant times the APSF. The intensity at the observation plane is given as square of the convolution of the transmittance and the ASPF.

$$I = |h \otimes t|^2 \quad \text{Eqn. 2.21}$$

If the imaging is incoherent, i.e. there is no phase relation of the light transmitted through the lens then the amplitudes no longer add to give the image but the intensities of the individual point images add to give the final image intensity at each position. This is given by the convolution of the square of both the APSF and the transmittance as shown in Equation 2.21

$$I = |h|^2 \otimes |t|^2 \quad \text{Eqn. 2.22}$$

2.5 Imaging in the confocal microscope

The simple confocal set-up is shown in figure 2.3. A point source fills a probe lens which focuses the light to a scanning object. The transmitted light is then focused via a collector lens

to the point detector. If we neglect the premultiplying constants the amplitude at the detector is given by the

$$U(x_d, y_d; x_s, y_s) = \int_{-\infty}^{+\infty} \int_{-\infty}^{+\infty} h_p(x_0, y_0) t(x_0 - x_s, y_0 - y_s) h_c\left(\frac{x_d}{M} - x_0, \frac{y_d}{M} - y_0\right) dx_0 dy_0 \quad \text{Eqn. 2.23}$$

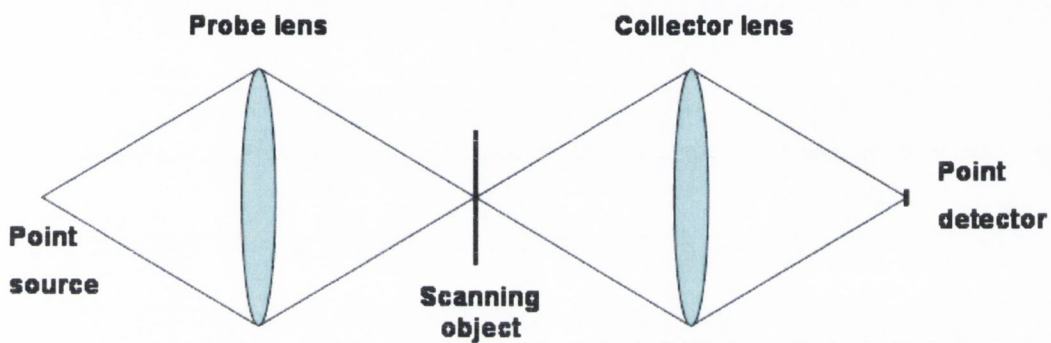


Figure 2.3 Schematic of confocal microscope optical system

Where h_p and h_c are the APSF of the probe lens and collector lens respectively, where $(x_d/M - x_0, y_d/M - y_0)$ represent a distance in object space and M is the linear magnification of the image. The amplitude transmittance is given by $t(x_0 - x_s, y_0 - y_s)$ where (x_s, y_s) represents a certain scan position. Together they describe the amplitude in the object plane, which in convolution with the point spread function of the collector lens give the amplitude at the detector. As we are dealing with a point detector at the focal position of the lens where $x_d = y_d = 0$, the intensity can be described as

$$I(x_s, y_s) = |h_p h_c \otimes t|^2 \quad \text{Eqn. 2.24}$$

Introducing a point detector gives an equal role to both the collector and the probe lens which for two equal circular pupils effectively multiplies the point spread function resulting in a sharpening of the image. The lateral resolution which is given for the conventional microscope as

$$I(v, 0) = \left[\frac{2J(v)}{v} \right]^2 \quad \text{Eqn. 2.25}$$

becomes for the confocal microscope

$$I(v, 0) = \left[\frac{2J(v)}{v} \right]^4 \quad \text{Eqn. 2.26}$$

This results in a sharpening of the image by 28% as measured at the FWHM.

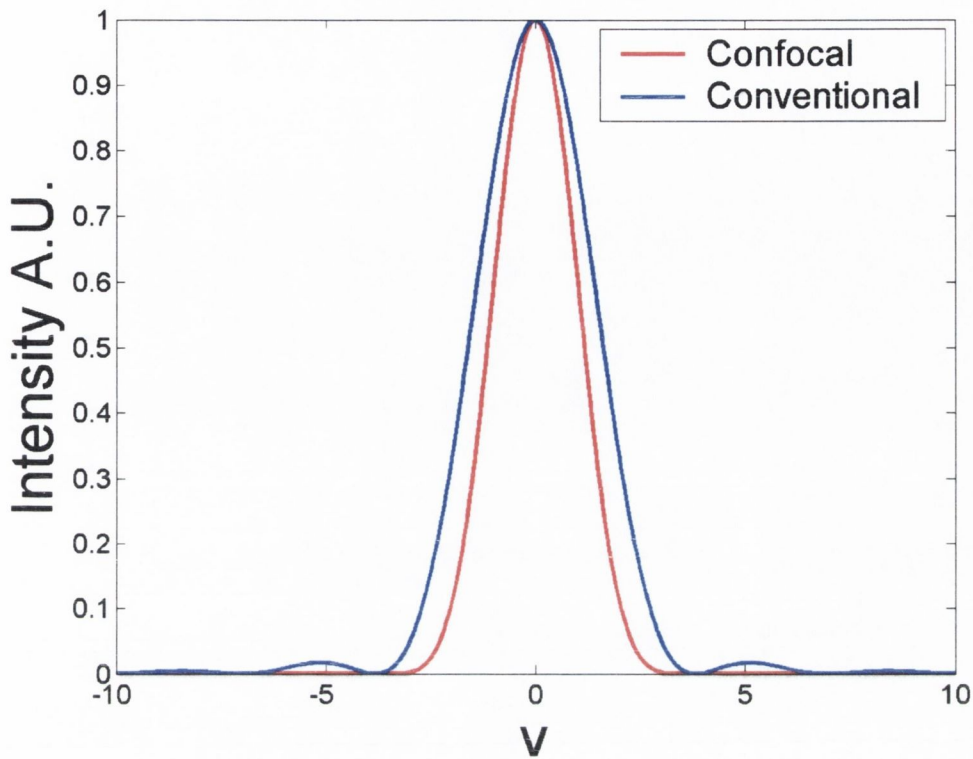


Figure 2.4 Lateral response of a point object in conventional and confocal microscopes.

The intensity in the intensity distribution for a point object along the optical axis is derived in a fashion similar to that of Equation 2.13 and is given by

$$I_{\text{point}}(u, 0) = \left(\frac{\sin u/4}{u/4} \right)^4 \quad \text{Eqn. 2.27}$$

The intensity distribution in the conventional only square root of the response for the confocal microscope as only one of the impulse responses contributes to the intensity distribution. If the depth of field is to be described as the fall-off in the maximum intensity the difference

between both microscope types is evident but not great. Other definitions have been suggested for the depth of focus¹⁵. Integrating the intensity of the image at different positions of defocus describes how the microscope discriminates against objects not in the focal plane. The integrated intensity is defined by the equation

$$I_{\text{int}}(u) = \int_0^{\infty} I(u, v) v dv \quad \text{Eqn. 2.28}$$

The value of the integrated intensity for the conventional microscope is a constant as the total power is collected by the large area detector irrespective of its position. On the other hand with a point detector the integrated intensity for the confocal microscope is given as

$$I_{\text{int}}(u) = \int_0^{\infty} |h_1(u, v)h_2(u, v)|^2 v dv \quad \text{Eqn. 2.29}$$

2.7 Summary

The goal of this chapter was to introduce to the reader the basic equations of characterisation of the confocal microscope and their origins. As the descriptions of the confocal microscope assume that the detector is infinitesimally small these equations describe the ideal case which is not found in practical microscope. The performance of most practical microscopes lie somewhere between that of the conventional and the ideal confocal microscope.

CHAPTER 3. LIQUID CRYSTAL VARIABLE FOCAL LENGTH LENS SYSTEMS

Liquid crystal lenses were designed, fabricated and their optical properties measured. The emerging light fields from the microlenses were imaged and used to study their optical properties in conjunction with an interferometer. We examined their optical quality as described by the Strehl ratio (SR). The captured light fields from the cells illustrate the aberrations present in these microlenses. To measure the values of aberration a specialized fibreised Mach-Zendher interferometer was used with a piezo-controlled stage for obtaining three dimensional (3D) images of the focal spot emergent from the microlens. A further study on the driving frequency of the applied voltage shows that the optical performance can benefit from carefully choosing the correct driving frequency of the applied voltage.

3.1 Introduction: Variable focal length systems

Variable focal length (VFL) systems are generally brought about by the mechanical movement of lenses. For some applications VFL systems that are compact and lightweight are required. VFL lenses were studied for such applications. They have been proposed for a variety of applications ranging from laser diode collimation¹⁶ to binoculars, projectors, and eyeglasses¹⁷.

A VFL lens was first patented by Wright in 1968¹⁸ and realized in 1971¹⁹. This lens operated on the principle of changing the radius of curvature of the lens. A rubber membrane was clamped between two rings and filled with a suitable fluid from a reservoir by a motor-driven pump. It performed quite well with a numerical aperture of 0.33 reported. This was a large lens of diameter 0.32m built for an application in hydroacoustic imaging. Three decades later, this type of lens was revisited applications to optical systems such as microscopy, optical pick-up systems and even as spectacles. Operating on the same principle as the larger lens new fabrication techniques, namely lithography and new membrane materials, most notably polydimethyl-siloxane (PDMS), have made the miniaturisation of these lenses possible. Recently these microlenses have been made into arrays²⁰ and are also being driven at great speeds²¹.

Lenses like those described above have a curved surface or surfaces across which there is a change in refractive index causing deformation of the wavefronts. It is also possible to focus light by a material possessing a gradient refractive index (GRIN lenses). Some electro-optical materials can have this refractive index gradient induced and controlled by application of a voltage across the medium. Thus by altering the voltage the focal length can be varied. This was first proposed by Y. Nishimoto²² in 1984. The proposed applications were in printers, fax machines and photocopiers, where it was surmised, the mechanical movement of lenses would become too slow to keep up with the ever increasing speed of the devices whereas lenses made from electro-optical crystal have sub-microsecond switching speeds. The fabrication of the lenses was realized by Chang *et al.*²³ who constructed a 1D lens from a LiTaO₃ total internal reflection modulator. Due to the fact that the electrodes were placed parallel to the direction of

the light beam the crystal was quite long and the light converged to a point inside the crystal. To overcome this, a thin crystal was prepared with a set of transparent electrodes placed on one side of the crystal with the opposite side grounded^{24, 25}. The crystal of choice became lanthanum-modified lead zirconate titanate (PLZT) because of its large electro-optical coefficient and the fact that it was cheaper than many of the other available crystals. By applying a voltage set across the electrodes a refractive index profile was obtained inside the crystal which then acted as a lens. By bringing two such lenses together a 2D lens was then formed²⁶. Aberration levels of these lenses were quite high due to two main issues. The first issue was that the refractive index distribution created inside the crystal was not smooth at the positions of the electrodes but increased stepwise. The second issue was also a product of the electrode positioning. Due to the periodic spacing of the indium tin oxide (ITO) electrodes there was a diffraction pattern superimposed on the focal spot. These issues were addressed by Song *et al*²⁷ who used the fact that the birefringence is related to the square of the electric field.

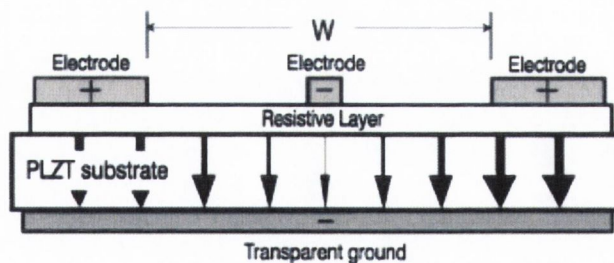


Figure 3.1 Schematic diagram of VFL lens produced by Song *et al*²⁷.

Therefore only a linear variation in the electric field across the crystal will bring about the quadratic distribution of the refractive index needed for a well focused light spot. Three electrodes replaced the large number previously fabricated on the crystal. These were attached

to a crystal via a resistive layer. A negative voltage was placed on the centre electrode and a positive voltage on the outer electrodes. The opposite side of the crystal contained a ground electrode.

This electrode configuration setup the required electric field distribution inside the crystal to focus the light. The centre electrode was kept thin so as to minimise light loss and aberration. Although the main aberration issue seemed to be solved there still remained some issues as to practical use of these type of lenses. The operating voltages were very high, typical voltage ranges were 0-60V²³ and as high as 300V²⁴ in some other cases. Also the numerical apertures (N.A.) were still low, the maximum reported N.A. was 0.06²⁵. Despite some good theoretical work on these lenses, the interest in them lessened.

In 1995 another type of VFL lens was reported²⁸, liquid lenses which worked on the principle of electrowetting. Electrowetting is the term given to the response of a contact angle of a droplet of electrolyte to an introduction of charges at the surface. Initially this was shown for an array of 1 μ L and 1nL droplets of hexadecanethiol under an aqueous sodium perchlorate solution placed on a gold substrate. Applying a voltage across the electrolyte and the gold surface altered the curvature of the droplets. By focusing light through the droplet with a varying curvature a VFL lens was obtained. The interest in these lenses increased with Berge *et al.*²⁹ presenting a high quality lens in a form available for mass production. These lenses were large, with typical diameters in the 1-10mm range and operated under higher voltages (90-200V). Using these type lenses it is also possible to move the focal length laterally by constructing patterned electrodes under the droplet³⁰.

3.2 Liquid crystal variable focal length lenses

VFL liquid crystal (LC) lenses were chosen for this research, since they are small, require low operating voltages and are easily made into arrays. All these traits suit application to the confocal system.

The majority of the research committed to VFL lenses was performed on LC structures. Much of this research over the years has been undertaken by Prof. Susumu Sato who pioneered the technology in 1979³¹. The technique is similar to that of the solid electro-optical lenses; the birefringence of the materials was exploited to make a variable focus GRIN lens. LC molecules are anisotropic birefringent containing a different refractive index along the long axis, ϵ_{\parallel} , and a short axis, ϵ_{\perp} . Incident light will react to a refractive index which will depend on the relative orientation of the polarization of the light to the long and short axes of the LC molecule. Nematic LC molecules are chosen for microlens applications because of their long-range orientational order, which is to say in their relaxed state the molecules tend to lie facing in a similar direction. When a voltage is applied across a LC cell their molecular orientation, or director profile, can be made to align somewhat with the field. If the polarisation of the light traversing the cell is parallel to the extraordinary axis of the birefringent LC the light responds to a different refractive index depending on the position of the LC molecule. Therefore a distribution of the director profile of the LC inside the cell is referred to as a refractive index distribution inside the cell. This refractive index distribution inside the cell is

the essence of the LC GRIN lens. Initial attempts at the design of LC lenses brought about the electric field gradient by a pattern of striped electrodes on the surface of the cell³². One of the main issues with LC VFL lenses was the low numerical apertures available. Attempts at increasing the NA was preformed by using stacked patterned electrode structures³³. Another approach was taken by Selviah *et al.*³⁴, who submersed photorelief microlenses in a LC cell contained between electrodes. By switching the LC the effective refractive index at the surface of the microlenses was altered changing the focal length of the system. See Appendix A for the focal length-voltage relationships measured for these lenses. Varying the voltage the lens system could be seen to switch from a diverging to a converging lens. These type lenses contain a high level of aberration, mainly due to the fact that the LC is anchored with a pretilt along a curved surface. The pretilt is a result of the rubbing procedure in the fabrication of the LC cell. The inside of the cells are coated with polymer and rubbed to allow for strong anchoring and alignment of the LC and an artefact of this is that the LC lie with a slight angle to the surface of the cell, the pretilt angle.

The fabrication method chosen in this study was one which provided a large focal length variation and was expected to produce low levels of aberration.

3.3 Fabrication

A glass slide of thickness 0.55mm was prepared with circular holes of a fixed diameter, d , etched in a hexagonal pattern on a thin chromium film previously evaporated onto one side of

the glass, shown in Figure 3.2. The opposite side of the cell is another glass slide, this one prepared with a thin film of ITO covered by a protective layer of SiO₂. Both slides were spin coated with a polyimide solution and rubbed. This ensures anchoring and alignment of the liquid crystal. Mylar spacers of known thickness (25μm), a , are placed between the glass to determine the depth of the LC layer. The thickness of the glass slides must be sufficient to keep them from deforming away from the Mylar spacers, taking this into account the slide must also be kept thin for the focal spot of the lens to be found outside of the cell. The Mylar spacers are kept in place by glue which is cured a small amount by a UV gun. The sample is then placed in a bag and put in a vacuum (~5mbar) for ~30 seconds. This is done so that as the air is sucked from the bag it distributes an even pressure across the surface of the cell. The cell is glued on three sides and placed in a UV light curing box for 10 minutes. The cell is then placed on a heating plate along with the LC. The reason for this is to heat the LC to the isotropic phase where there is no long range orientation of the LC, or no preferred direction for the molecules in the LC. This transition can be viewed directly, when in the nematic phase the different domains within the LC scatter the light and the LC appears dark. On heating the transition to the isotropic phase is noticed when the LC becomes clear. The LC is injected to the side of the cell and is filled by capillary forces. The remaining side is glued and cured. The LC shows planar alignment on cooling. The LC crystal chosen in this study was BL006 (a nematic liquid crystal from Merck), chosen for its large values of birefringence $\Delta n=0.286$ (589 nm, 20 °C) and dielectric anisotropy $\Delta\epsilon=17.3$ (1 kHz), which have been reported to increase the NA of the LC microlenses³⁵. Two samples with different diameter lenses were investigated, $d = 60$ and $80\mu\text{m}$. The Mylar spacers were $25\mu\text{m}$. The overall sample size is approximately 100cm^2 .

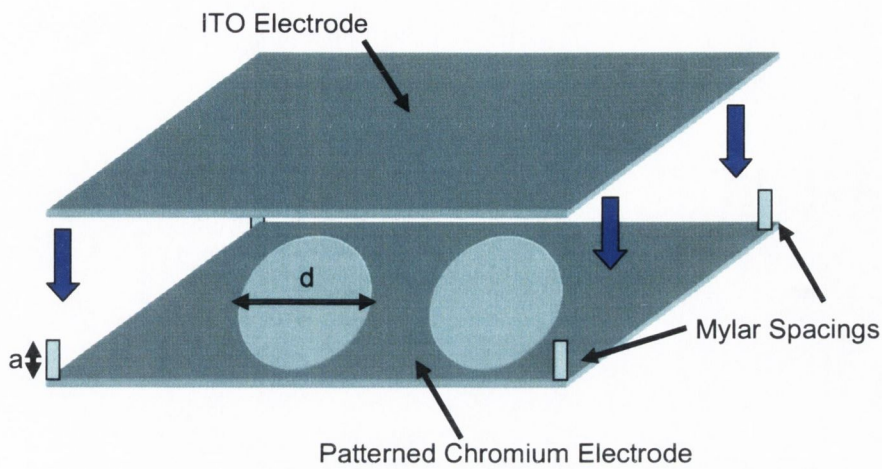


Figure 3.2 Schematic of LC cell

3.4 Experimental set-up and theory

Optical characterisation was carried out on a Mach-Zehnder interferometer designed for the optical characterisation of micro-optics³⁶, shown in Figure 3.3. At the core of the instrument is a Zeiss-Microscope. The light source is a He-Ne laser with a wavelength of 633 nm. The object and reference arm of the interferometer are illuminated with two polarization-preserving single-mode fibres. In the object arm, an ideal microscope objective produces a spherical wavefront and the microlens under test collimates the light into a plane wave deformed by the lens aberrations. This light joins the collimated beam from the reference arm to produce an interference pattern at the CCD camera.

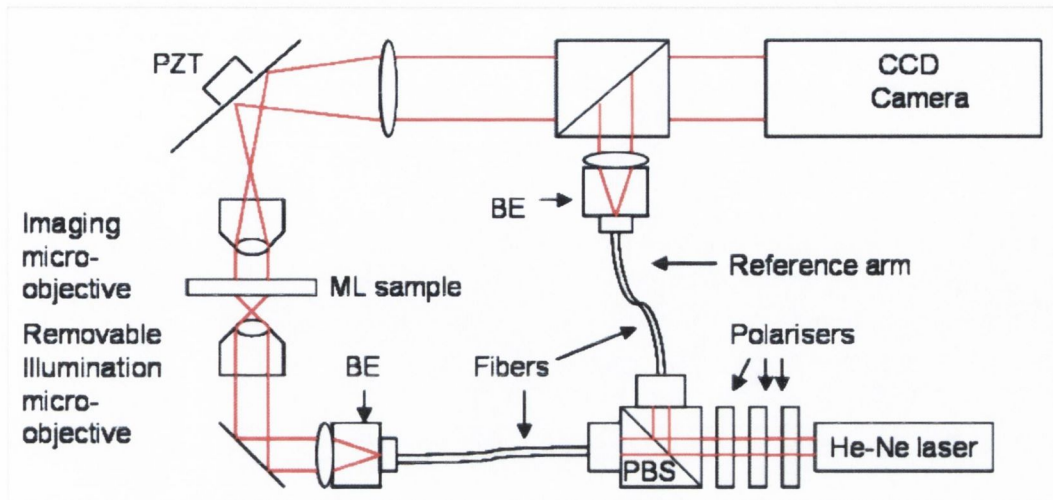


Figure 3.3 Schematic of experimental set-up

From this interferogram the software ³⁶ calculates the phase distribution by means of least squares and compares it to that of a plane wave that should emerge in the case of a perfect lens. This is done by use of the Zernike polynomial expansion, W , which is commonly used to map wavefront aberrations with a small number of coefficients. Zernike polynomials are one of an infinite number of complete sets of polynomials in two real variables, ρ and θ that are orthogonal in a continuous fashion over the interior of a unit circle. A wave front can be described using the first set of Zernike coefficients is described by the equation³⁷.

$$W(\rho, \theta) = Z_0 + Z_1 \rho \cos \theta + Z_2 \rho \sin \theta + Z_3 (2\rho^2 - 1) + Z_4 \rho^2 \cos 2\theta + Z_5 \rho^2 \sin^2 2\theta + Z_6 (3\rho^2 - 2) \rho \cos \theta + Z_7 (3\rho^2 - 2) \rho \sin \theta + Z_8 (6\rho^4 - 6\rho^2 + 1) \quad \text{Eqn.3.1}$$

Here Z_0, Z_1, \dots, Z_8 are the Zernike coefficients and $\rho \sin \theta, \rho \cos \theta$ are the polar coordinates in x and y plane. By rearranging the terms and using the relationship

$$a \cos \alpha + b \sin \alpha = \sqrt{a^2 + b^2} \cos[\alpha - \tan^{-1}(b/a)] \quad \text{Eqn. 3.2}$$

Equation 3.1 it can be rewritten as

$$\begin{aligned}
 W(\rho, \theta) = & Z_0 - Z_3 + Z_8 + \left(\rho \cos \left[\theta - \tan^{-1} \left(\frac{Z_2 - 2Z_7}{Z_1 - 2Z_6} \right) \right] \right) \left(\sqrt{(Z_1 - 2Z_6)^2 + (Z_2 - 2Z_7)^2} \right) \\
 & + \rho^2 \left(2Z_3 - 6Z_8 \pm \sqrt{Z_2^4 + Z_5^2} \right) \pm 2\rho^2 \sqrt{Z_4^2 + Z_5^2} \cos^2 \left[\theta - \frac{1}{2} \tan^{-1} \left(\frac{Z_5}{Z_4} \right) \right] \\
 & + 3\rho^3 \sqrt{Z_6^2 + Z_7^2} \cos \left[\theta - \tan^{-1} \left(\frac{Z_7}{Z_6} \right) \right] + 6\rho^4 Z_8
 \end{aligned} \tag{Eqn. 3.3}$$

This can be rewritten as more clearly as

$$\begin{aligned}
 W(\rho, \theta) &= \sum C_n^m Z_n^m \\
 Z_n^m &= \rho^n \cos^m \theta
 \end{aligned} \tag{Eqn. 3.4}$$

The aberration is expressed as a summation of the product of the respective Zernike coefficients, C , and Zernike polynomials, Z , where n and m are the radial and angular numbers respectively. The aberration type is expressed by the Zernike polynomial while the magnitude is given by the Zernike coefficient. The table below details the aberration and there magnitudes are described by Equation 3.3.

Polynomial Term	Description	Magnitude
Z_1^1	Tilt	$\sqrt{(Z_1 - 2Z_6)^2 + (Z_2 - 2Z_7)^2}$
Z_2^0	Defocus	$(2Z_3 - 6Z_8 \pm \sqrt{Z_2^4 + Z_5^2})$
Z_2^2	Astigmatism	$\pm 2\sqrt{Z_4^2 + Z_5^2}$
Z_3^1	Coma	$3\rho^3 \sqrt{Z_6^2 + Z_7^2}$
Z_4^0	Spherical	$6Z_8$

Table 3.1 Common aberrations present in the lenses and their coefficients and description

The rms value of the aberration is calculated by $rms = \sqrt{\sum (C_m)^2}$. The Strehl ratio (SR) can be calculated from the rms value as follows

$$SR \approx \exp\left[-(2\pi rms)^2\right] + \frac{(2\pi rms)^4}{2} \quad \text{Eqn. 3.5}$$

The Strehl ratio (SR) is the ratio of the intensity at the Gaussian image point (the origin of the reference sphere is the point of maximum intensity in the observation plane) in the presence of aberration, divided by the intensity that would be obtained if no aberration were present³⁷. The magnitudes of the common aberrations along with the SR value calculated from the interferograms are then used as a measure of the optical performance. The aberrations that present in lens systems, shown in Table 3.1, are astigmatism, spherical and coma aberrations as shown in Figure 3.4. Astigmatism is present in lenses where the light from an off axis point source is focused differently at perpendicular edges of the lens. The sagittal and tangential rays overlap at different places along the optical axis resulting in a blurred focal spot and an

elongated reduced intensity PSF, as shown in Figure 3.4 (c). Coma aberration is named after a comet as this the light imaged by a lens containing this aberration gives a comet-like focal spot. This occurs due to light which enters off-axis being focussed to a point above or below the geometrical focal spot. Spherical aberration occurs when the light entering the centre of the lens is focussed to a different position along the optical axis to those rays traversing the outer regions of the lens.

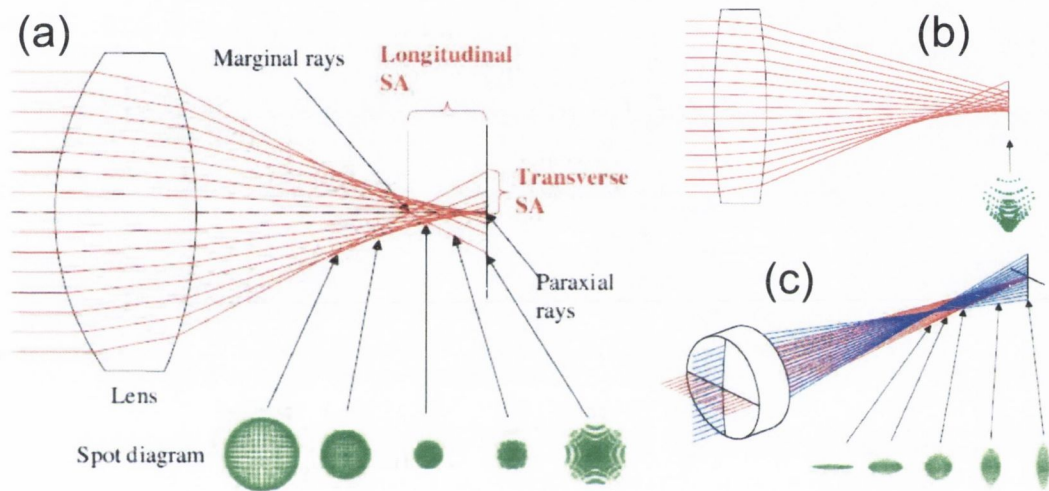


Figure 3.4 Schematic diagram representing (a) spherical aberration, (b) coma aberration and (c) astigmatism and their respective intensity distributions at planes close to the focal point.³⁸

By removing the microscope objective below the sample stage in Figure 3.3 the sample is illuminated by a plane wave. From the resulting interferogram the focal length of the microlens sample can be determined. For imaging of the emerging light fields of the microlenses the stage can be adjusted by the manual coarse adjustment of a microscope stage so as to image the focal spot region of the microlens sample to the CCD camera. The stage is

then controlled by piezo actuators to move the sample in steps of $1\ \mu\text{m}$ to image the entire 3D region in and around the focal spot.

3.5 Optical characterization

With the lenses placed on the interferometer and illuminated under plane wave illumination the focal length at varying voltages can be measured. Figure 3.5 shows these measurements for a microlens arrays with lenses of diameters 60 and 80 μm . The graph has been separated into three regions of interest describing the different effects of the voltage on the LC in the cell. At low voltages below there is no realignment of the LC and therefore no lens, this is shown in section I in Figure 3.5. This is due to the fact that the interactions between the LC layer and the glass slide have a large effect on the orientation of the LC in the cell. The influence of this effect is to oppose the response of the applied electric field which results in a threshold phenomena named the Fréedericksz transition ³⁹. In section I of Figure 3.5 the voltage is below this threshold value. At voltages above the transition the LC director profile at the edges of the electrode holes begins to align with the electric field, section II, this results in a refractive difference across the hole causing a lens to form. As the voltage increases the LC at the edge of the hole aligns to a greater extent resulting in a higher refractive index distribution difference between the centre of the cell and the edges, this explains the drop in focal length. At a certain value of applied voltage the realignment of the LC at the edge of the hole is complete except for a thin surface layer which corresponds to the electrical coherence lengths of the reorientation. Further increasing the electric field leads to penetration towards the centre of the hole. At this voltage the maximum NA for this lens is found. Section 3 is characterized by an increase in the focal length from the maximum NA. This is explained by the greater penetration of the electric field into the hole as the voltage is increased further; the

LC in the centre of the hole begins to realign with the electric field. The refractive index difference between the edges and the centre begins to decrease and thus focal length increases.

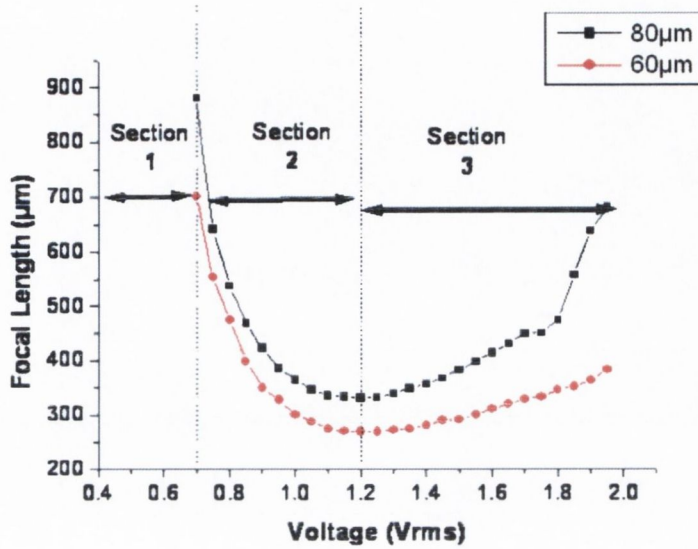


Figure 3.5: Focal length voltage dependence of microlenses.

Illuminating the lenses with a spherical wave in the Mach-Zendher interferometer gives an interferogram resulting from the interference of the emerging wave and the plane wave in the reference arm. From this interferogram the phase distribution is calculated by means of least squares and compared to that of a plane wave that should emerge in the case of a perfect lens. The Zernike polynomial expansion $W(p, \theta)$ is used to represent the wave aberration with each coefficient of the expansion providing values for the different forms of aberration. Measured SR values of the microlenses are shown in Figure 3.5. It can be seen that for the 80μm lens the quality is above the accepted criterion over a range of approximately 0.05V corresponding to a variation in focal length of less than 10 μm. The accepted criterion here refers to the Maréchal criterion which declares that for a lens is diffraction-limited if it has a Strehl ratio value of

greater than 0.8¹³. For the 60 μm lens, however, the quality is sufficient over 2 V. Geometry has shown to be important in the variations of the optical output of these lenses³⁵.

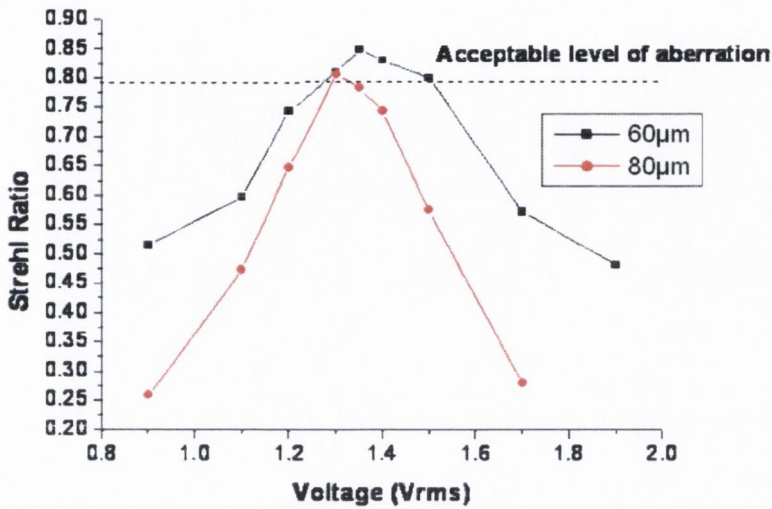


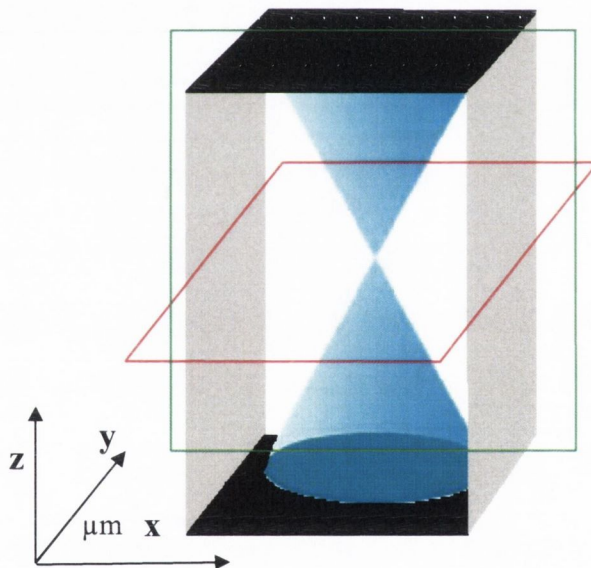
Figure 3.6: Strehl ratios of two microlenses samples at varying voltages.

From further experiments on similar LC cells with different diameter lenses we also found that an increase in diameter size of the lens (by 50 μm) results in a reduction in the optical quality (by over 10%) linked with an increase in numerical aperture (of approximately 30%). Liquid crystal microlenses of low numerical aperture (<0.103) show the highest optical quality (>0.9).

A piezo-controlled stage on the microscope together with a microscope objective with high numerical aperture allowed light to be imaged from different sections of the emerging light fields onto the CCD camera. A number of steps, 100 steps of 1 μm , created a collection of 2D images which were then grouped together and graphed using Matlab. These graphs allowed full inspection of the 3D light fields in and around the focal spots of the lenses. Examination

of these light fields gave an indication as to the levels of the main aberrations resulting from these lenses. The fields are imaged $100\mu\text{m}$ along the optical axis and $138\mu\text{m}$ in x and y directions. The point of highest intensity is found and centred on the CCD array and the stage is moved $50\mu\text{m}$ along the optical axis to image as much of the area around the focal spot as possible. The light fields cannot be presented in 3D in this thesis; only planes of interest can be shown. Therefore the notation of the planes in x , y and z will be given as (x, y, z) with units in μm , as shown in Figure 3.7.

Figure 3.7. Schematic diagram showing sections of 3D light fields, red plane and green plane are described as in the notation used as $(x,y,50)$ and $(x,50,z)$.



The light fields from a $60\mu\text{m}$ lens were imaged at two separate voltages, 0.95 and 1.35V. Strehl ratio values of approximately 0.55 and 0.85 were recorded at these voltages, respectively.

The astigmatism present is best shown if the z plane is imaged at distances from the focal spot or the circle of least confusion, where the highest intensity is found. The point of highest intensity in the 0.95V lens is found (91, 69, 69). Therefore the xy planes at $z = 99$ and $39\mu\text{m}$ were graphed and are shown Figure 3.8(a) and (b).

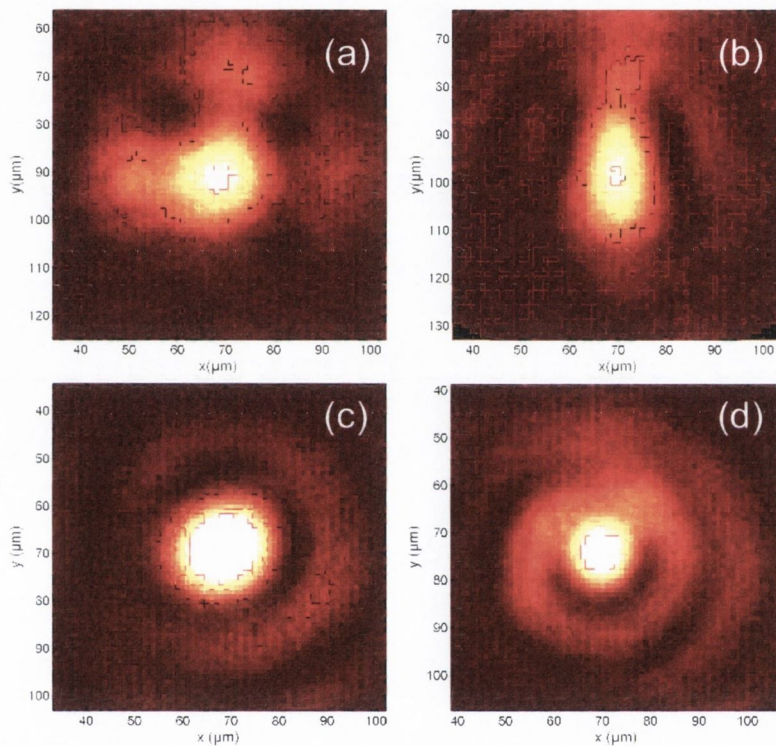


Figure 3.8. Captured images of planes of light emerging from lenses at planes, (a) $(x, y, 39)$ at applied voltage 0.95V, (b) $(x, y, 99)$ at applied voltage 0.95V, (c) $(x, y, 30)$ at applied voltage 1.35V, (d) $(x, y, 90)$ at applied voltage 1.35V.

If the intensity profile is plotted for the x and y directions through the point of highest intensity and the FWHM found, the extent of the spread of the light in either direction can be shown. FWHM of the intensity profiles in the x $(x, 70, 99)$ and y $(99, y, 99)$ directions for the

0.95V are 26 and 13 μm respectively. When imaged on the other side of the focal spot the intensity profiles (x, 68, 39) and (91, y, 39) give FWHM of 19 and 27 μm respectively. This clearly shows the presence of a large amount of astigmatism. The same process was carried out for the higher quality lens produced at 1.35V. Were the image planes (x, y, 30) and (x, y, 90) were imaged, shown in Figure 3.8 (c) and (d), and the intensity profiles of the x and y direction were graphed to find their FWHM. FWHM of 14 μm and 14.5 μm were found for intensity profiles (x, 68, 30) and (70, y, 30) respectively. Profiles found from the planes graphed on the far side of the focal spots give FWHM of 13 μm and 11 μm for lines (x, 70, 90) and (75, y, 90). There is a vast reduction in the astigmatism found in the high voltage lens. As this is also a higher NA lens the angles of the light entering and exiting the focal spot are greater resulting in a larger spread of light at a fixed distance from the point of highest intensity. As the astigmatism is measured at equal distances from the point of highest intensity the astigmatism in the higher NA lens would be more pronounced. Whereas in this case there appears to be none if very little astigmatism present in the lens created by the 1.35V. The presence of astigmatism is also shown in the wavefront deviation as calculated from the interferogram measured on the Mach-Zendher which is depicted graphically in Figure 3.9. The high level of aberration at the top and bottom centre of the graph is indicative of astigmatism aberration in the x direction⁴⁰. This is shown in the magnitude of the aberration as given by the Zernike polynomials, as calculated by the interferometer software, the magnitude for astigmatism in the x-direction is seen to drop from 0.2993 to 0.1093 for lens created at 0.9V and 1.35V. From the figures it appears that the main aberration present is indeed astigmatism.

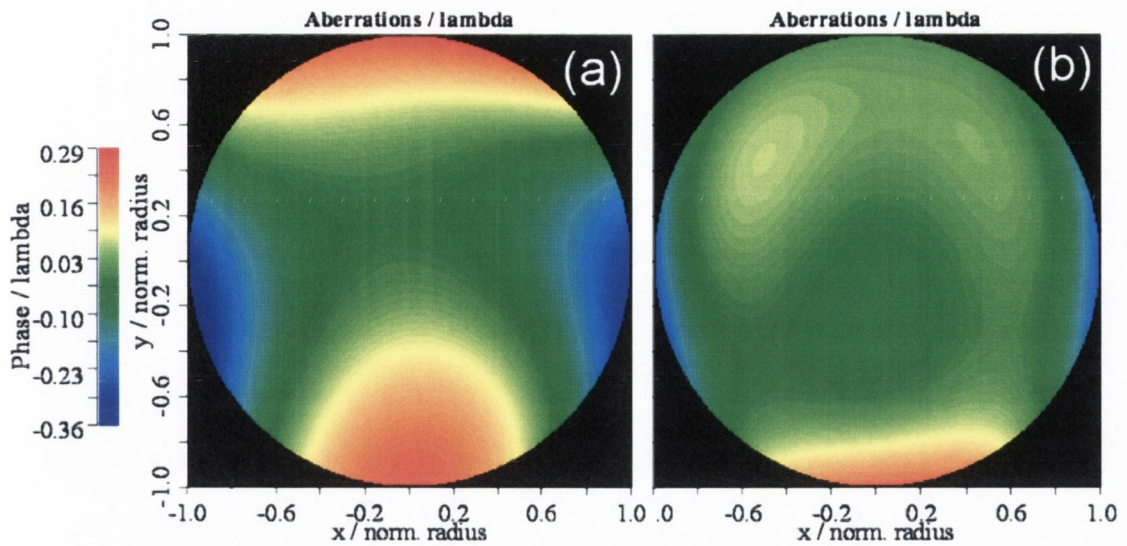


Figure 3.9. Aberration values of a lenses created by a (a) 0.9V and (b) 1.35V as measured by the interferometer.

The presence of coma aberration can also be seen in the light fields. Images of the planes $(x, 69, z)$ and $(91, y, z)$ taken from the light fields of the 0.95V lenses clearly show the occurrence of coma aberration, Figure 3.10 (a) and (b). The coma in the x direction is the more evident as can be seen in the image of the y plane $(x, 69, z)$, Figure 3.10 (a). Light from the edge of the lens is focussed a different place along the x axis. In contrast to the images of the point spread function (PSF) of the 0.95V lenses the light from the 1.35V lens is concentrated in a neat intense PSF, Figure 3.10 (c) and (d).

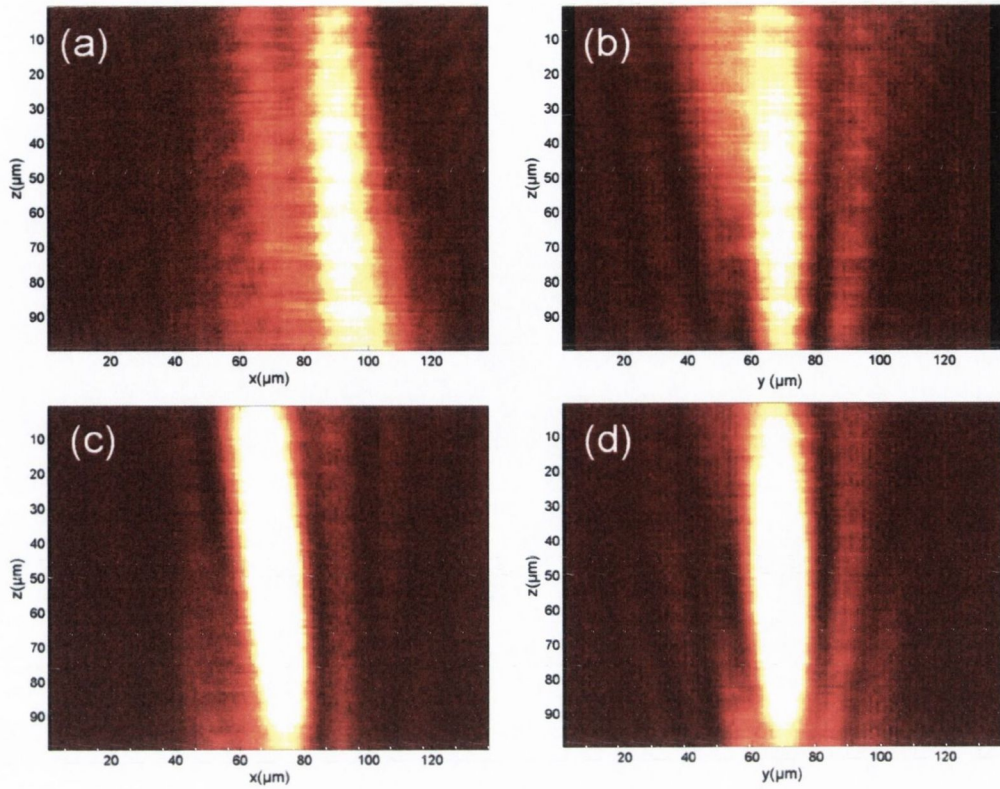


Figure 3.10. Images of the longitudinal PSF of lenses created by two voltages, (a) $(x, 69, z)$ at 0.95V, (b) $(91, y, z)$ at 0.95V, (c) $(x, 69, z)$ at 1.35V and (d) $(72, y, z)$ at 1.35V.

3.6 Increase in optical quality by control of the frequency of driving voltage

Many LC microlenses have been presented in the literature but frequently there is no discussion on the choice of the driving frequency of the applied voltage. Scharf *et al.*⁴¹ have shown that the focal length of dual frequency LC lenses can be controlled by changing the

driving frequency. Here we investigate the effect of varying the driving frequency on a standard LC lens. It was found that by changing the frequency brought a change in the optical quality of the lenses was also brought about. A LC microlens array with a LC layer thickness of 50 μm and a lens diameter of 115 μm was used. The SR was found to increase with increasing frequency up to values approximately 1.5 MHz, as shown in Figure 3.11.

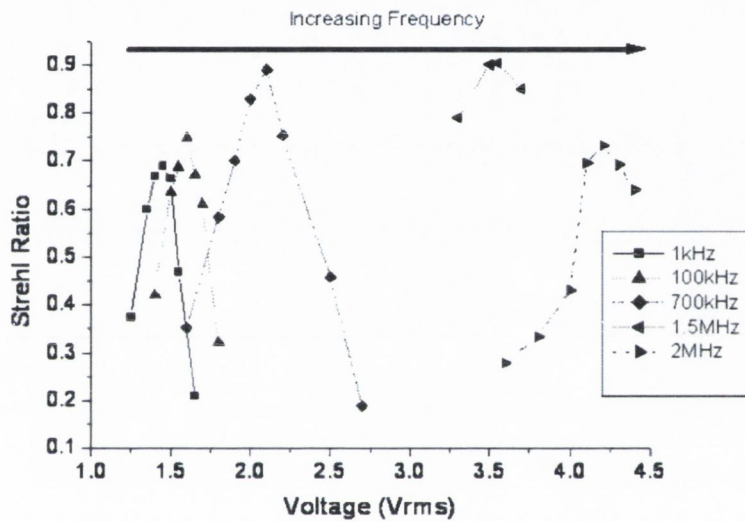


Figure 3.11 Graph showing the increase of Strehl ratio with increasing value of the driving frequency of the applied voltage.

Variation of the driving frequency from 1 kHz to 1.5 MHz gives an increase in the optical performance of the system by over 30%. With the lenses that are driven at a frequency of 1 kHz, the most favourable driving frequency for these type lenses, they do not reach the Maréchal criterion for acceptable level of aberration in a lens. Increasing the frequency to 700 kHz brings the lens to an acceptable quality over a voltage range of 0.2 V.

An explanation for this behaviour is found in the dielectric values of the LC. Dielectric values are dependent on the frequency of the driving voltage. The torque, Γ , on each of the LC molecules is dependent on the dielectric values $\Gamma = \epsilon \epsilon_0 E^2$. This is shown in the focal length voltage scans shown in Figure 3.12. The shape of the scans is similar but a higher voltage is required to get the necessary deformation of the LC inside the cell in order to achieve a certain focal length at higher frequencies. Therefore the dielectric values of the liquid crystal must be changing in the given frequency range. This was also suggested by measurements done on an HP network analyzer (41952). The network analyzer was used to test the capacitance of two samples, firstly an empty ITO cell and then the same cell filled with the LC BL006.

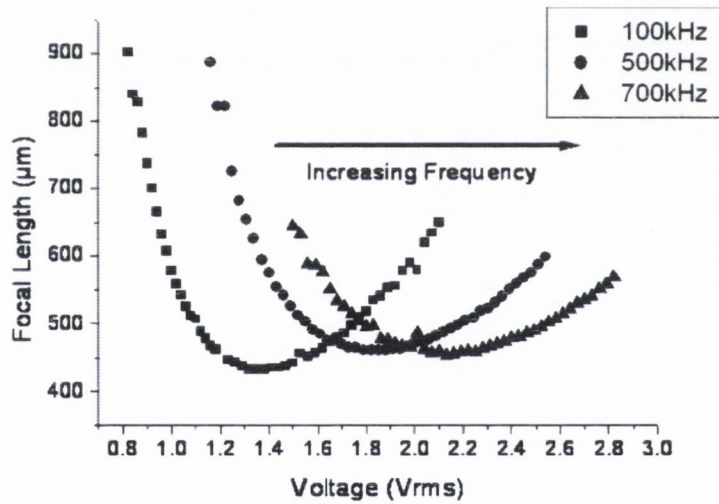


Figure 3.12 Focal length variations with voltage with increasing frequencies.

The capacitance was tested over a range of frequencies for both the switched and unswitched liquid crystal positions, for ϵ_{\parallel} and ϵ_{\perp} respectively. It found that both varied over the concerned frequency range. The torque experienced by the LC molecules is dependant of the dielectric

values and the dielectric values on the frequency. Thus the obtain the same focal lengths at higher frequencies, higher voltages must be applied for the LC to experience the same torque, which can be thought of as changing the refractive index. The lenses that are created at higher values of the applied frequency and voltage are found to have improved optical performance, as measured by the Strehl ratio.

The LC cells were modelled by means of the program LCD MASTER from Shintech using the electric constants and the dielectric values specific to BL006. In the model cell 2V was applied and the equilibrium positions of the LC were found by use of the Frank-Oseen equation. The result is the position and direction of the individual LC molecules within the simulation.

$$n_e(\theta) = \frac{n_o n_e}{\sqrt{(n_e^2 \sin^2 \theta + n_o^2 \cos^2 \theta)}} \quad \text{Eqn. 3.6}$$

$$Phase = \frac{2\pi}{\lambda} \int_{-r}^r n_e(\theta) dz \quad \text{Eqn. 3.7}$$

The effective refractive index, $n_e(\theta)$, can then be calculated from the director profile by use of Equation 3.6 where n_o and n_e are the ordinary and the extraordinary refractive indices respectively and the angle of the LC director molecule is given by θ . By integrating the refractive index along the width of the cell the phase profile for one cross section of the lens can be calculated. The phase profiles resulting from two such simulations are shown in Figure 3.13. The first simulation was the result of a cell modelled with the dielectric values parallel, ϵ_{\parallel} , and perpendicular, ϵ_{\perp} , as described in the literature for BL006 driven at 1 kHz, 22.8 and

5.5 respectively, giving a value of 17.3 for $\Delta\epsilon$ we have named this A The second simulations took values of half that given for 1 kHz, ($\epsilon_{\parallel}=11.4$ and $\epsilon_{\perp}=8.65$, $\Delta\epsilon=2.75$), and was named B.

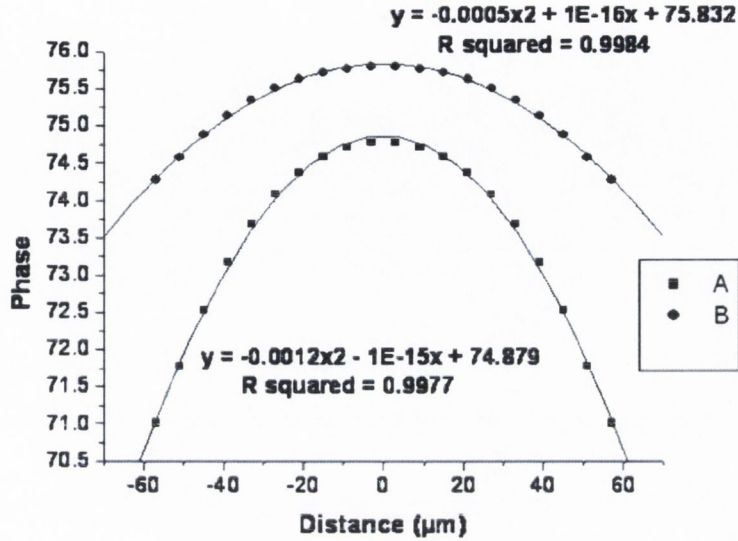


Figure 3.13 Phase profiles of modelled LC microlenses with different values of the dielectric constants due to a difference in the driving frequency of the applied voltage (2V)

The phase profiles show a greater radius of curvature for the 50% epsilon, which would mean a longer focal length, this is expected as a greater electric field is needed to achieve the same deformation on the LC at lower dielectric values. The important factor here is the fit to the parabolic curves. The lower value of the dielectric shows a superior fit to the parabolic curve, which means there is a smoother refractive index distribution within the LC cell. A smoother distribution in turn means the lens is less likely to have spherical aberration. Further experiments with the interferometer show that the spherical aberration tends to decrease with increasing frequency as shown in Figure 3.14 which further shows a favourable distribution of refractive index in the cell.

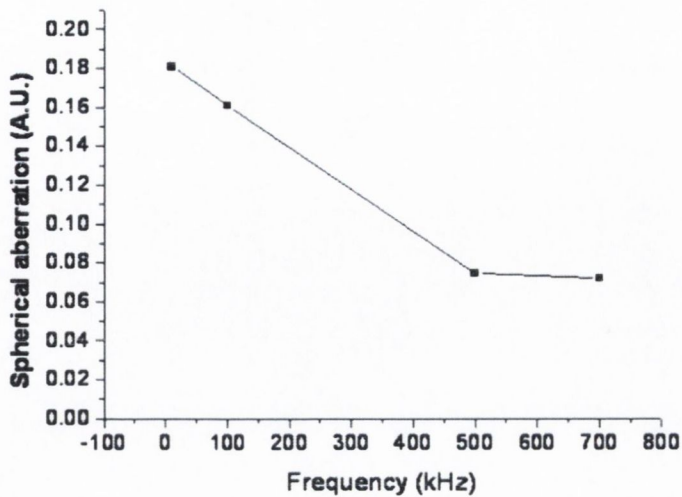


Figure 3.14 Relationship between spherical aberration and the driving frequency.

3.7 Conclusions

The emerging light fields of LC microlenses have been measured for the first time. There is strong agreement between the visual evidence of aberration and those calculated from the interferograms. Previously interference patterns of the extraordinary and ordinary rays passing through the microlens have been employed for the estimation of microlens quality, it has been shown here that a more thorough investigation by the calculation of wavefront aberration and the examination of the emerging light fields can show far greater detail in terms of optical quality. In addition it is also a simple procedure that is very time efficient for the qualitative analysis of the optical properties of the lens at different voltages. A quick examination at the

light in the focal plane, in Figure 3.15, is almost sufficient to see if a good lens has been formed.

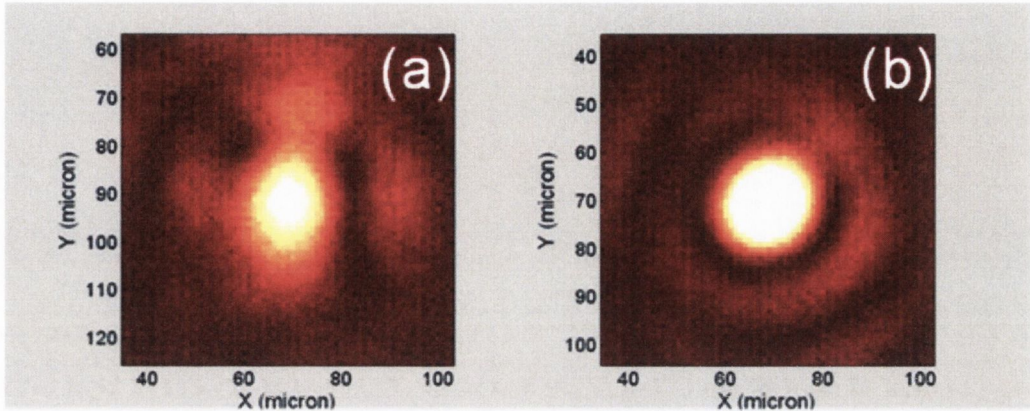


Figure 3.15 Focal spots of Lens created at (a) 0.95V and (b) 1.35V.

It has been shown here that the lenses have only a certain voltage range over which they have adequate optical quality and this is unfortunately a voltage range over which the focal length variation is minimal. Therefore these lenses may be used in applications where they can be used as a switch, for instance for fibre coupling⁴², or in low quality imaging where a variable focal length microlens is needed. However it has been shown that by even rough adjustment of the frequency with which the applied voltage is driven the optical quality of these lenses can be significantly improved by up to 30%. This could pave the way for higher quality liquid crystal lenses.

As is shown in this work, astigmatism is one of the main contributing factors to a decrease in the optical quality. This is most likely due to the fact that there is a large difference in the elastic constants for the LC BL006. The elastic constants are equivalent to those of a spring

and are the values which determine the force needed for the liquid crystal to perform any of the three deformations, splay, bend and twist. Figure 3.16 shows the orientation of the LC across the bottom glass slide containing a patterned chromium electrode. The LC molecules (not to scale) are aligned parallel to the rubbing directions with a small pretilt ($<10^\circ$). The ground electrode across the top of the cell (not shown) causes the electric field to form a symmetric pattern inside of the hole area.

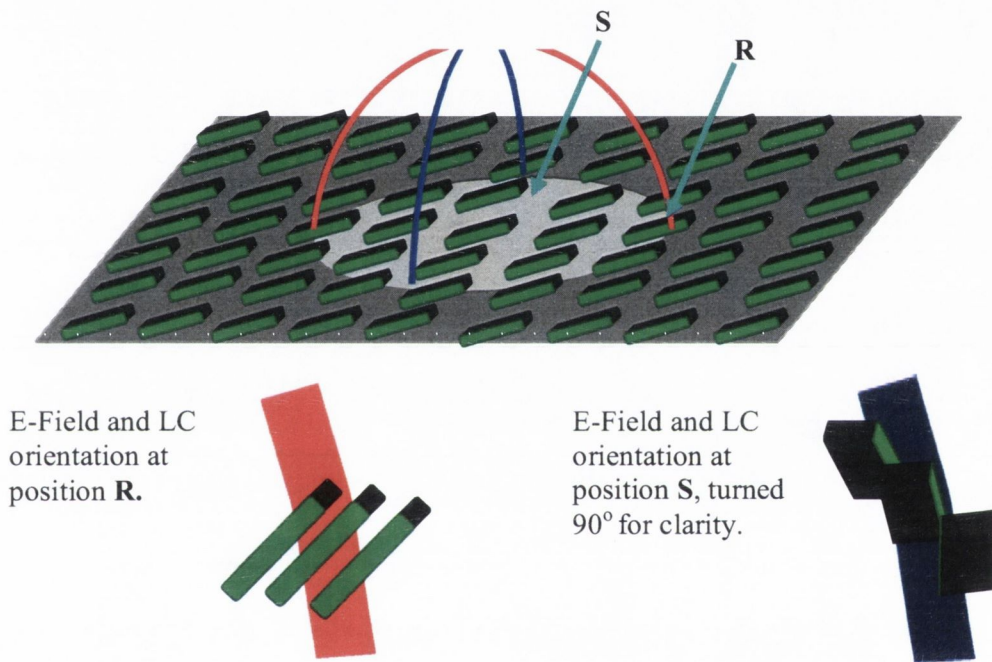


Figure 3.16. Schematic diagram showing the alignment of the liquid crystal across the surface of the glass slide with pretilt. The hole in the chromium layer is shown in light grey, and the LC molecules in green and black. The electric field is shown in red in the direction parallel to and blue in the direction perpendicular to the rubbing direction. Below are enlarged images of the LC at positions R and S, with S turned 90° for clarity. The LC at R is in a splay deformation while at position S there is a combination of splay, bend and twist.

As the LC is aligned in the rubbing direction the LC at the edges of the hole at different positions experience different electric fields. The maximum difference is found at the edge of the hole along the rubbing direction and perpendicular to that. Two such positions R and S are shown to explain the different forces on these liquid crystals. As the LC aligns with the electric field at the R position there is a splay deformation while at position S there are bend and twist deformations. The energy for these deformations is provided by the applied electric field. The final position is found when the elastic and electric fields are in equilibrium. The free energy per unit volume, F_v for nematic liquid crystal is given in terms of the spatial derivative or the director, \hat{n} . This is described by the Frank-Oseen equation³⁹,

$$F_v = \frac{1}{2}K_1[\nabla \cdot \hat{n}]^2 + \frac{1}{2}K_2[\hat{n} \cdot (\nabla \times \hat{n})]^2 + \frac{1}{2}K_3[\hat{n} \times (\nabla \times \hat{n})]^2 \quad \text{Eqn.3.8}$$

Here K_1 , K_2 , and K_3 are the elastic constants which describe the ‘stiffness’ of the LC to each of the splay, bend and twist deformations. The difference between the various K values will have a significant effect on the amount of astigmatism present. BL006 has a large difference between its elastic constants which accounts for the large amount of astigmatism in the lenses studied. A clear understanding of the electric field and LC molecular orientation with varying elastic constants could lead to the higher quality lenses in the future.

CHAPTER 4

APPLICATION OF VARIABLE FOCAL LENGTH SYSTEMS TO THE CONFOCAL MICROSCOPE SYSTEM

4.1 Introduction

A traditional confocal microscope images a single point with high resolution by restricting the collected light from a sample to that reflected or emitted from the focal spot region of the objective lens, as is outlined in the introductory chapters. For this reason the field of view is narrow. To obtain an image of the sample, one needs a three-dimensional scan. One development of confocal microscopy involves techniques to achieve real-time imaging without compromising resolution. The use of a Nipkow disk as a pinhole array is the first approach to providing real-time confocal imaging with reduced scanning in the lateral direction¹². However, the primary problem in using a Nipkow disk is its low light throughput,⁴³ which is due to the large mark-space ratios of ~ 5 required for reducing the cross talk between neighbouring pinholes in the disk without compromising the system's resolution. A combination of a microlens array and a Nipkow disk offers an improvement in the light throughput of as much as 40% by matching the foci of the microlenses to the pitch and diameter of the pinholes⁴⁴. Further development involves the design of a real-time clinical

confocal endoscope; a confocal imaging system with a miniature objective and a flexible fibre bundle has been studied^{45, 46}. The fibre bundle can act as both a pinhole array and an image-carrying element. Juškaitis *et al.*⁴⁷ described a real-time confocal microscope that views a fibre bundle in parallel to a Nipkow disk at its proximal end. McCabe⁴⁸ proposed a system that for the first time applies a variable-focal-length (VFL) microlens array to selectively address a coherent fibre bundle and thus achieve confocal imaging. Variable focal length microlenses are studied as a high throughput aperture array providing an array of point sources which can then be imaged to a sample, in this case a mirror. The use of a fibre bundle acting as a pinhole array and an image conduit in conjunction with the lenses is also investigated.

Microlens arrays have shown to be used as an array of objective lenses in the confocal system⁴⁹⁻⁵¹. This can increase the field of view by the number of lenses used were the lateral resolution and depth discrimination properties are defined by the NA of the individual lenses in the array as shown by Tiziani *et al.*⁵¹. With the inclusion of VFL as an array of objective lenses there exists the possibility for continuous axial detection. By varying the applied voltage across the LC VFL lenses the focal length can be made to axially scan the sample. Thus VFL negates the need for mechanical movement for either the objective lenses or the sample, while also decreasing the need to laterally scan the sample.

4.2 VFL microlens arrays as high throughput aperture arrays with fibre optical bundle

4.21 Fibre bundle characterisation

The fibre bundle that we used is a Sumitomo IGN20/50 imaging bundle (2m long) with 50,000 fibres, where an individual fibre has a diameter of $\sim 4\mu\text{m}$. The centre-to-centre spacing of two neighbouring fibres is $\sim 8\mu\text{m}$. The core diameter is $\sim 2\text{mm}$. The bundle was characterized by coupling light from both a coherent He-Ne laser (wavelength 632.8nm) source and an incoherent Tungsten white light lamp by using the set-up shown in Figure 4.1. For the white light, a $50\mu\text{m}$ pinhole was placed in the focus of a 10cm focal length lens as a spatial filter. The output power of the He-Ne is $\sim 6\text{mW}$ while the tungsten lamp has a much lower intensity transmitted through the pinhole, $\sim 1\mu\text{W}$ as measured by a power meter. The expanded He-Ne beam or collimated white light source was coupled to the fibre bundle through a x10 objective lens with a numerical aperture (NA) of 0.25. This objective lens was mounted on a translational stage for movement in the axial direction. The fibre was mounted on a two-dimensional stage for the alignment of the fibre bundle in the lateral directions. The two lenses placed after the fibre bundle are the imaging lenses, which project a magnified image of the fibre bundle end onto the CCD camera. Neutral density filters were used to keep the CCD cell from saturating

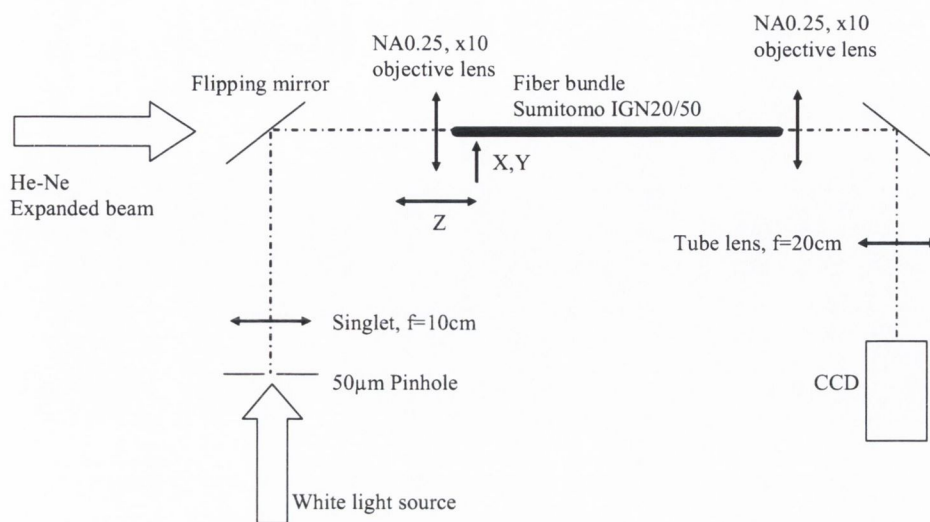


Figure 4.1 Schematic of experimental set-up for the characterisation of the fibre bundle

When the face of the fibre bundle was placed in a defocus position with respect to the objective lens, a large area of the fibre bundle is illuminated. The images of the fibre bundle end are shown in Figure 4.2. When using the coherent laser source, due to the interference of the fibres, the speckle effect is very evident in the image of the fibre end, shown in Figure 4.2(a). Thus the light transferred by the fibres was not uniformly distributed at the end. However, by using white light, the hexagonally packed fibre bundle can be clearly seen in the image, shown in Figure 4.2(b). On the other hand, when an individual fibre in the bundle was precisely aligned to the focus of the objective lens, the light is confined to a single fibre, shown in the insets of Figure 4.3. Figure 4.3 (a) and (b) show the intensity profile of the coupled single fibre using He-Ne or Tungsten lamp, respectively.

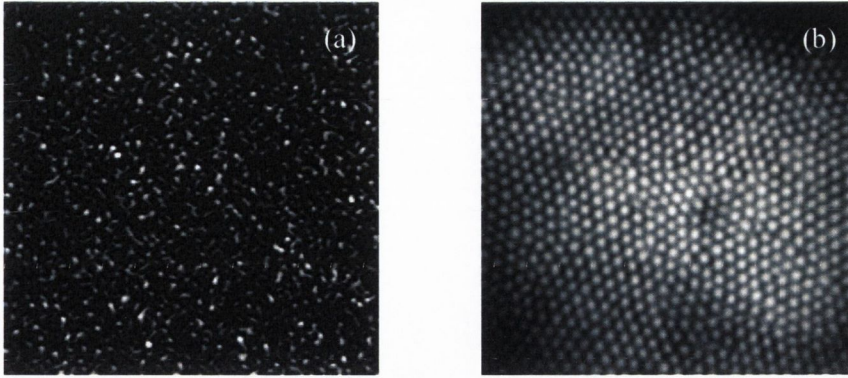


Figure 4.2. Images of the fibre bundle end. (a) with He-Ne coherent laser source; and (b) with Tungsten incoherent light source. Images are $232 \times 232 \mu\text{m}^2$.

The width of the profile by Gaussian fit is $\sim 4.0\mu\text{m}$ which relates to the mode diameter of the fibre. It is noticed that the propagation behaviour of coherent and incoherent light along an individual fibre also appears different. Figure 4.3(a) shows a non-zero background which may be due to the interference effect of the coherent light.

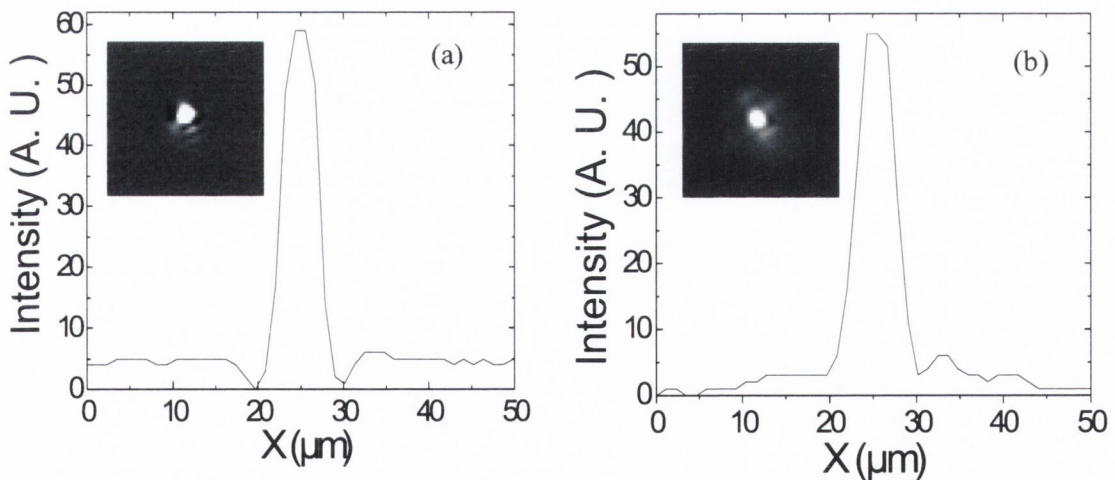


Figure 4.3. Intensity profile of the single fiber coupled with (a) He-Ne; and (b) Tungsten.

Insets are the corresponding images of the coupled fiber. Images are $58 \times 58 \mu\text{m}^2$.

4.22 Fibre bundle coupling with VFL microlens array

VFL LC lenses as described in Chapter 3 were used for this experiment. The difference here is that the lenses were made using the LC E7 Merck, a commonly used LC as its properties have been well studied. The lenses were $135\mu\text{m}$ in diameter with a centre-to-centre distance of $155\mu\text{m}$ and a liquid crystal layer thickness of $50\mu\text{m}$. The focal length voltage relationship for these lenses was examined using the set-up shown in Figure 4.4. By moving the objective lens in the optical axis the lenses could be imaged to the CCD camera. The lens array was moved to image the focal spot to the camera thus measuring the focal length. Only the He-Ne light source is used due to the low intensity of the tungsten lamp transmitted through the pinhole. Also as the microlens array only focuses light polarized in the direction parallel to one axis of the aligned anisotropic LC the intensity would be further reduced by passing the light through a polarizer.

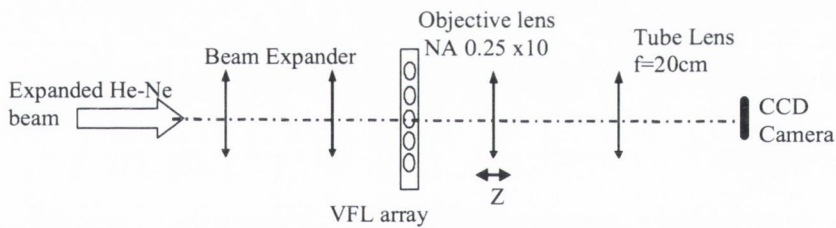


Figure 4.4 Schematic of experimental set-up for the investigation of the focal length voltage relationship of the lenses.

Figure 4.5 (a) shows the image of the lenses taken from the experimental set-up shown in Figure 4.4. When a voltage is applied across the cell by signal generator, the microlenses will focus the incident light to an array of foci which can then be imaged by the CCD camera. Figure 4.5(b) shows the image of the foci produced by applying a driving root-mean-square

(RMS) AC voltage of 2.83V and frequency of 1kHz. The intensity profile of two focal spots was plotted in Figure 4.5(c). The full-width-half-maximum of the focus is about $3.5\mu\text{m}$, which gives NA of the microlenses ~ 0.1 . This agrees with the focal length voltage relationship shown in Figure 4.5 (d). The focal length ranges from $2543\mu\text{m}$ (at 1.27V) to $645\mu\text{m}$ (at 2.83V), where accordingly a NA ranges from 0.003 to 0.1. Note that for the voltages below 1.27V, the electric field has not formed a lens shape, and for the voltage above 2.1V, only a slight change of the focal length can be observed. Hence, in the following, we focus our study mainly on the range of 1.4V- 2.1V, where the focal length of the microlenses varies sensitively with the change of voltage. Unfortunately as was shown in the previous chapter this is also the range over which the aberration of the lenses is quite high.

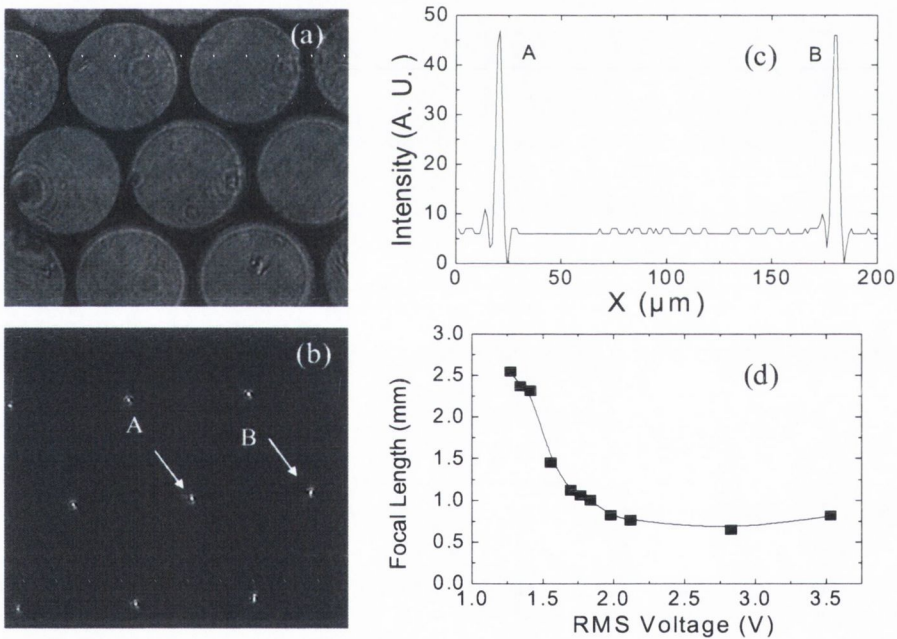


Figure 4.5 Image of (a) the variable focal length microlens array; (b) foci, where driving voltage (RMS) is 2.83V. Image sizes are $464 \times 464 \mu\text{m}^2$, (c) Profile of the foci A and B, (d) focal length voltage relationship.

By using the setup shown in Figure 4.6, we coupled the light into the fibre bundle through the microlenses. Two objective lenses, x10 (NA0.25) and x50 (NA0.65), were used in front of the microlenses and the fibre bundle respectively. The lens system produces a maximum demagnification of 5. By carefully aligning the distances between microlenses, objective lenses and fibre bundle, microlenses can be imaged to the face of the bundle and then transferred to the CCD camera with the different sets of demagnification.

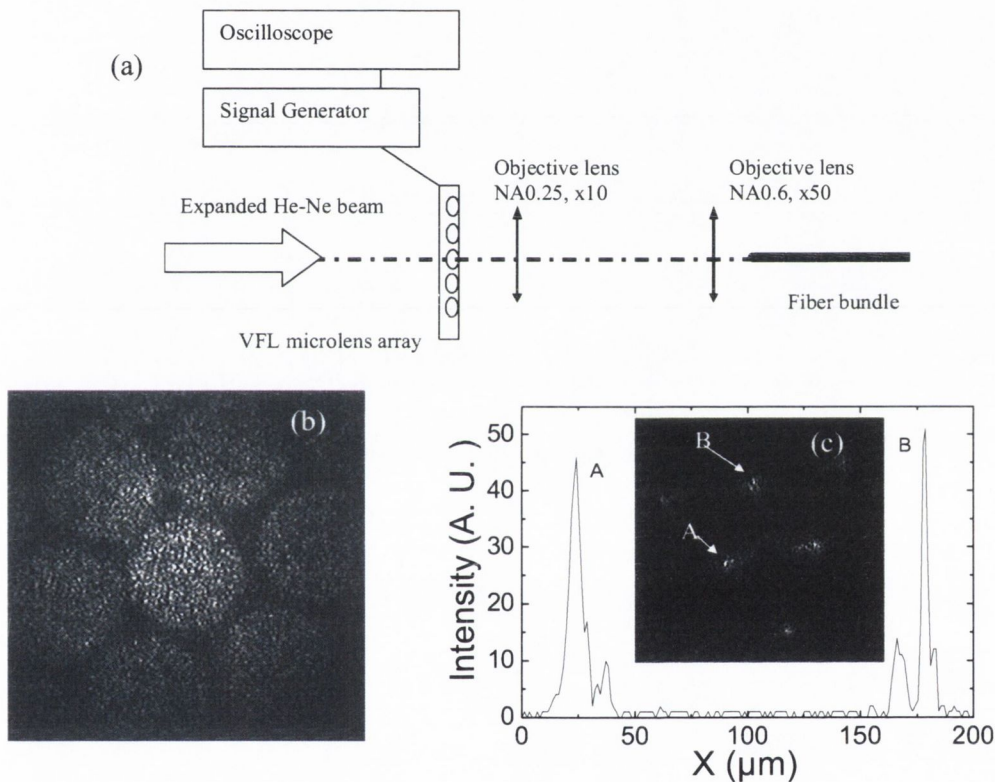


Figure 4.6. (a) Schematic diagram set-up used for the coupling of light from the microlens array to the fibre bundle (b) Image of microlens array transferred by the fibre bundle; (c) Intensity profile of two spots A and B. Inset: image of the microlens foci with voltage applied 1.77V. Images are $464 \times 464 \mu\text{m}^2$.

Figure 4.6(b) shows the image of the microlenses through the fibre bundle with the demagnification ~ 1 . When an electric field was applied the microlenses focused the light. Adjusting the distance between the microlenses and the x10 objective in front, the array of the foci can be imaged onto the face of the fibre bundle, as shown in the inset of Figure 4.6(c) where the voltage is set at 1.77V. Since the focal spot of a single microlens approximates to the mode diameter of an individual fibre, good coupling between a microlens focus and a fibre tip can be obtained by careful alignment. The intensity profile in Figure 4.6 (b) shows two selected spots A and B which are well coupled to fibres. The distance between neighbouring coupled fibres is $\sim 160\mu\text{m}$. Hence there are about 20 idle fibres between two coupled fibres. The small amount of splits shown in Figure 4.6(b) are due to the fact that the fibre bundle is actually not precisely hexagonally packed and thus the mismatch between the microlens focus and the fibre tip is inevitable.

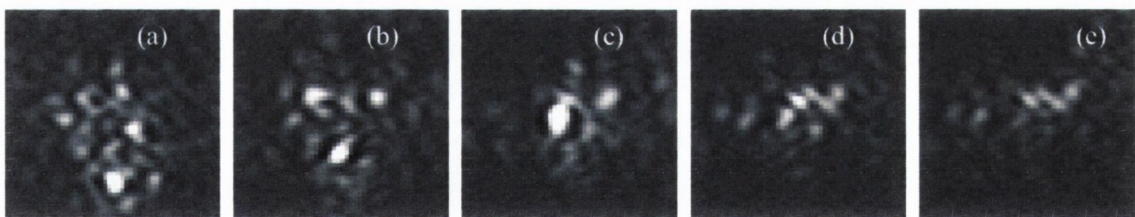


Figure 4.7. (a)-(e) Images of the fibre bundle surround the spot A, shown in the inset of Fig. 6(b). The applied voltages are 1.41V, 1.56V, 1.77V, 1.98V and 2.26V, respectively. Images are $58 \times 58 \mu\text{m}^2$.

By varying the applied voltage, the focal length of the microlenses was changed. As a result, the fibre bundle became defocused or decoupled. Figure 4.7(a)-(e) show the zoom-in image of spot A with the microlens applied voltage at 1.41V, 1.56V, 1.77V, 1.98V and 2.26V, respectively. When defocused, the light from a microlens was split across several fibres.

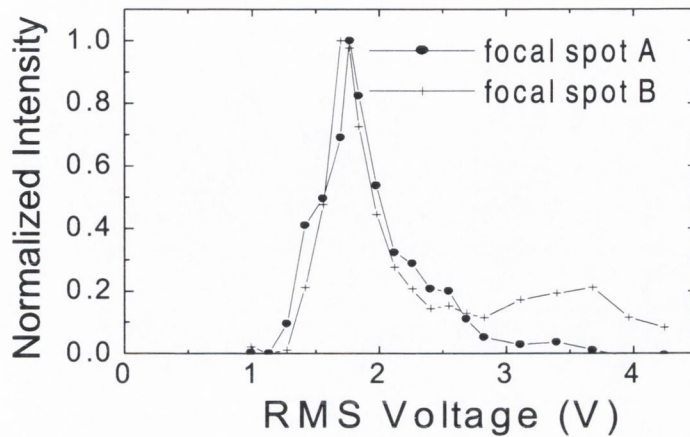


Figure 4.8. Normalized intensity of the focal spots vs. supplied average. The intensity was averaged over an area of $11 \times 11 \mu\text{m}^2$.

The intensity responses of spots A and B, (as shown in Figure 4.7), as a function of the applied voltage are shown in Figure 4.8. The intensity was averaged over an area of $11 \times 11 \mu\text{m}$, which locates on a fibre which is in-focus and well coupled at the voltage of 1.77V. The full-width-half-maximum (FWHM) of the voltage response is approximately 0.5V. In the case of the system demagnification of ~ 1 , this response width corresponds to the focal length variation of $\sim 750 \mu\text{m}$ in front of the fibre bundle according to the data shown in Figure 4.5(d). By moving the microlens close to the focal plane of the x10 objective lens and fibre bundle close to the x50 objective lens, a larger demagnification can be obtained. Figure 4.9(a) shows the image of microlenses with the system demagnification of ~ 4.2 . Due to the interference of the coherent light propagating along the bundle, the microlenses cannot be clearly distinguished.

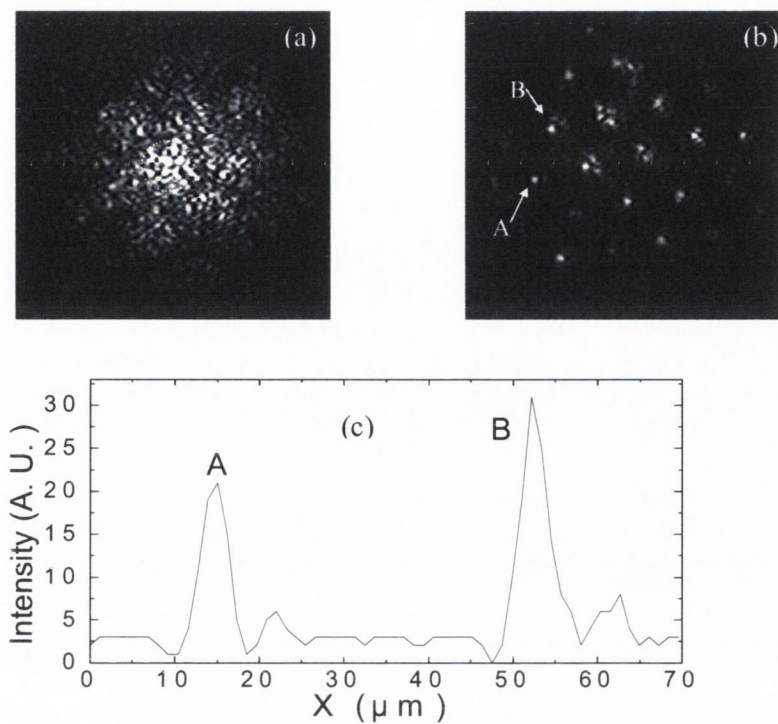


Figure 4.9. (a) Image of microlens array guided by fiber bundle. Dotted circle relates to a microlens. (b) Image of the focal spots with voltage supplied 1.77V. (c) Intensity profile of two spots A and B, as shown in (b). Images are $232 \times 232 \mu\text{m}^2$.

The dotted circle illustrates an ideal imaged microlens. However, when the voltage was applied, the foci of the microlenses were well coupled to the fibre bundle, shown in Figure 4.9(b). The intensity profile in Figure 4.9(c) gave a coupled fibre spacing of $\sim 37\mu\text{m}$, which means that there are ~ 4 idle fibres between the coupled neighbours. Although the interference appears in this case and gives a higher background between two coupled neighbouring fibres than that in the case of Figure 4.6(b), the coupled foci still can be distinguished with reasonable uniformity. The missing foci are mainly due to the mismatching of the microlenses

and the fibre bundle. This suggests that when the ratio between the coupled fibre spacing and the fibre diameter is ~ 5 or larger, the interference between fibres raised by the coherent light can be neglected.

Similarly, we measured the intensity response as a function of the applied voltage in the case of system demagnification of ~ 4.2 , shown in Figure 4.10. The FWHM of voltage is $\sim 0.5V$ which relates to the focal length variation of $\sim 750\mu\text{m}/4.2^2$, ($\sim 43\mu\text{m}$) in front of the fibre bundle according to geometric optics. We attribute the extraordinary response behaviour of spot B above 3.2V to the possibility of the deformation of the lens when applying high voltage.

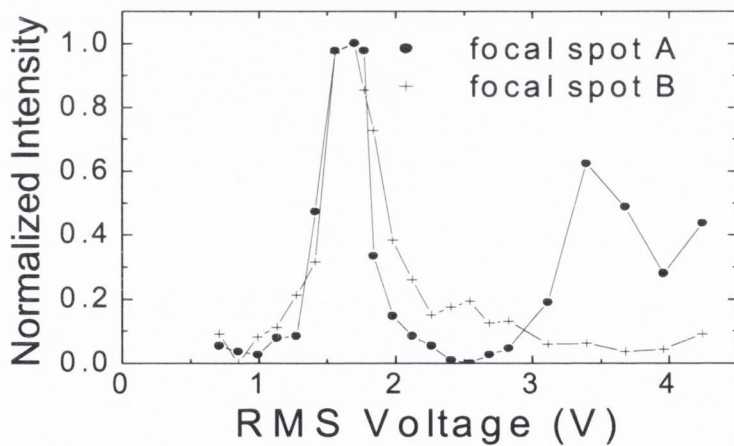


Figure 4.10. Normalized intensity of the spots shown in Fig. 9(b) vs. supplied average. The intensity is averaged over an area of $16 \times 16 \mu\text{m}^2$.

4.23 Confocal system with VFL lens array and fibre bundle

We then applied the VFL microlens and fibre bundle into a confocal set-up. The setup is shown in Figure 4.11. A mirror sample replaced the fibre bundle and was aligned to the focal plane of the x50 objective lens. The reflected and collimated light from the mirror was coupled to the fibre bundle through a beam splitter and a x10 objective lens.

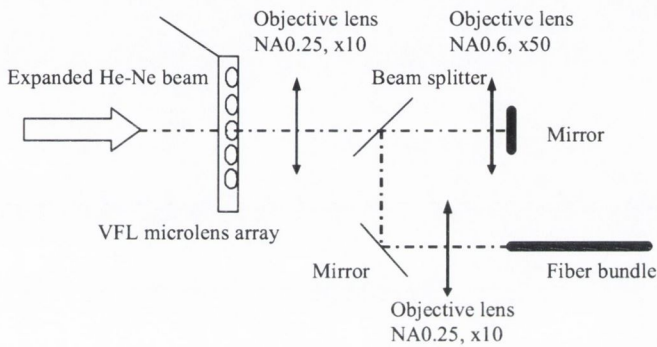


Figure 4.11. Schematic of the confocal system utilising the VFL lenses and the imaging fibre bundle.

The images of the microlens and the foci coupled to the fibre bundle at 1.77V are shown in Figure 4.12 (a) and (b) respectively. The intensity profile shows us that the lenses were spaced by $\sim 176\mu\text{m}$. This indicates that the system is quasi-symmetric and has a magnification of ~ 1.13 . Again, we showed that using a microlens array, the fibre bundle can be well addressed. By applying the voltage, the focal length of the microlens varies and correspondingly, the focus of the x50 objective lens will axially scan the mirror sample. The images of the fibre bundle end are shown in Figure 4.13(a)-(c) for the applied voltage at 1.62V, 1.77V and 1.98V, respectively. The intensity response was measured over the output of the fibre bundle end, shown in Figure 4.13(d). The intensity is calculated as an average intensity over the area of $11 \times 11 \mu\text{m}^2$ surrounding the spots A or B. The FWHM is $\sim 0.25\text{V}$ which is less than that of direct

microlens-fibre-bundle coupling. This is due to the sectioning property of the reflected confocal system.

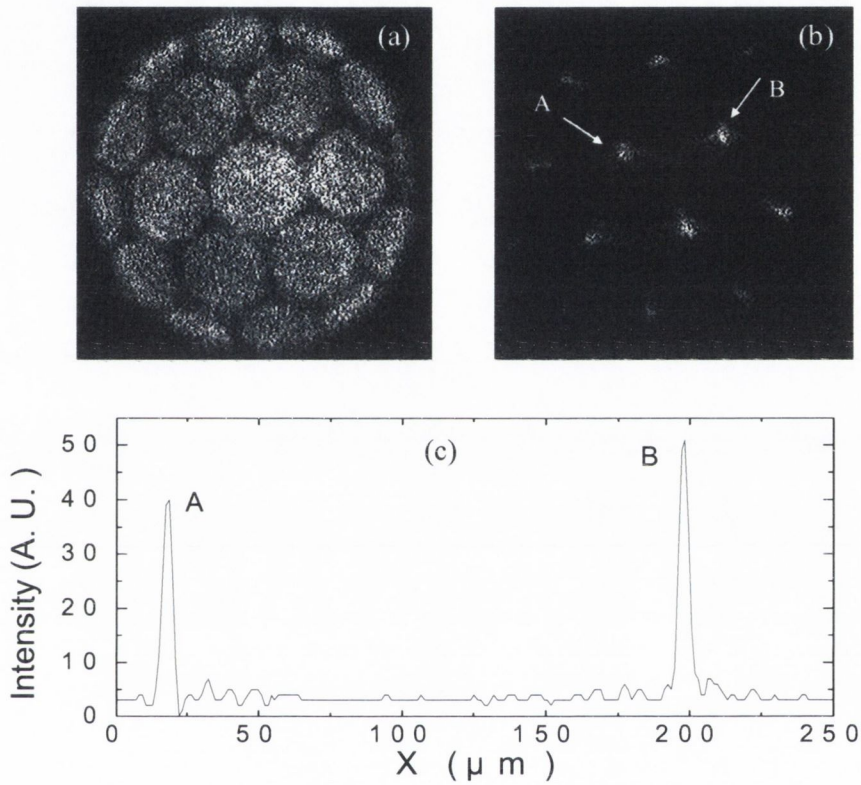


Figure 4.12. (a) Image of microlenses by using setup shown in Figure 11. (b) Image of the focal spots with voltage supplied 1.77V. (c) Intensity profile of two focal spots A and B. Images are 638 x 638 μm^2 .

According to data shown in Figure 4.5, the change of voltage from 1.60V to 1.85V will give a focal length change of the microlens about $400\mu\text{m}$. Since the microlenses were de-magnified by 5 to the mirror, based on geometric optics, the focal spots of the microlenses focused by the x50 objective lens varied at the distance of $\sim 400\mu\text{m}/5^2$, ($\sim 16\mu\text{m}$).

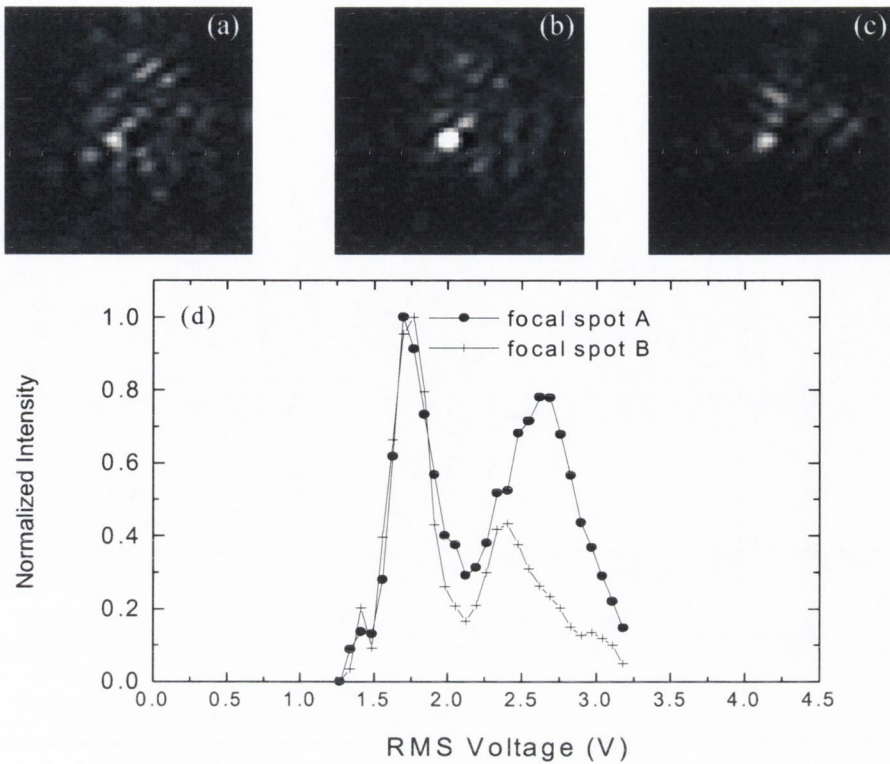


Figure 4.13 (a)-(c) Images of the fiber bundle surround the spot A, shown in the inset of figure 4.12(b). The applied voltages are 1.62V, 1.77V and 1.98V, respectively. Images are $58 \times 58 \mu\text{m}^2$. (d) Normalized intensity of the focal spots vs. applied average. The intensity is averaged over an area of $16 \times 16 \mu\text{m}^2$ surrounding the spots A or B.

Hence, the FWHM of the system axial response will be $\sim 16\mu\text{m}$. The NA of the microlens is variable from 0.047 to 0.068 with the change voltage from 1.60V-1.85V and the efficient NA of x50 objective in front of the mirror, NA_{obj} will be from 0.23 to 0.34. Hence, for the ideal confocal system with only a pinhole, while the pinhole is infinitely small, the FWHM of the axial response can be estimated as $\sim 0.9\lambda/\text{NA}_{\text{obj}}^2$, i.e. $< 12\mu\text{m}$. However, in our case, due to the cross-talk and interference between neighbouring fibres added with the finite size fibres acting

as a pinhole array, the axial response of the system is larger than the ideal case. In Figure 4.13(d), the asymmetric side lobes can be easily observed. Sheppard *et al.*⁵² have shown that for a small amount of spherical aberration in a confocal system there can be large degradation of the axial response with large side-lobes appearing on one side of the defocus. As we know from the optical characterisation of the VFL lenses there is a great presence of spherical aberration that becomes highly apparent at voltages above the voltage required to get the minimum focal length.

The difference between two axial response curves of spots A and B indicates that the microlenses focussing properties varies from lens to lens. This is further complicated by the fact that the lenses may not be perfectly laterally aligned to the fibres.

4.3 VFL microlens arrays as an array of objective lenses

Focal scanning, where the focal spot is made to axially scan the sample can be achieved by using VFL microlens array as an array of objective lenses. This also increases the field of view as mentioned in the introduction (see Section 4.1). The proposed set-ups closely follow those designed by Tizanni *et al.*⁵³. Two scans are possible in theory with these lenses, the first is traditional object scanning, the second being focal scanning. In object scanning the object is moved, there is a change in z , and a new plane falls into the focal plane, i.e. the plane to be imaged. In focal scanning, the focal length changes, moving the image plane to a new part of the sample to be imaged. This can be controlled electronically via the applied voltage to the

lens array. There is no need for mechanical movement of the sample or the objective lenses in the axial direction; there is also a reduced need for lateral scanning due to the increase in the field of view. The new planes to be imaged are always confocal with the pinhole.

Axially scanning a plane mirror through the focal plane of a confocal microscope is a standard technique for the measurement of the optical sectioning property of a confocal system. The mirror is moved to a defocused position; therefore the microscope is imaging a new plane in the sample (which in this case is obviously air). The detected light from the mirror is a measure of the amount of light from out-of-focus positions that contributes to the final image. Scanning across all the defocused positions builds up the common axial scan which is used to characterise the sectioning properties.

When the focal length of our VFL is changed, a new position of the sample is under scrutiny. If the mirror is in the old, now defocused position, it will reflect a certain amount of light into the lens. This is a measure of the amount of light that is scattered from the off-focus positions. By scanning the focal length of the lenses across all the defocused positions and noting the detected intensity through the pinhole a response is measured very similar to that of the traditional mirror, or object, scan. Both type scans were investigated using the set-up shown in Figure 4.14. The lenses used for this study had a diameter of 100 μ m.

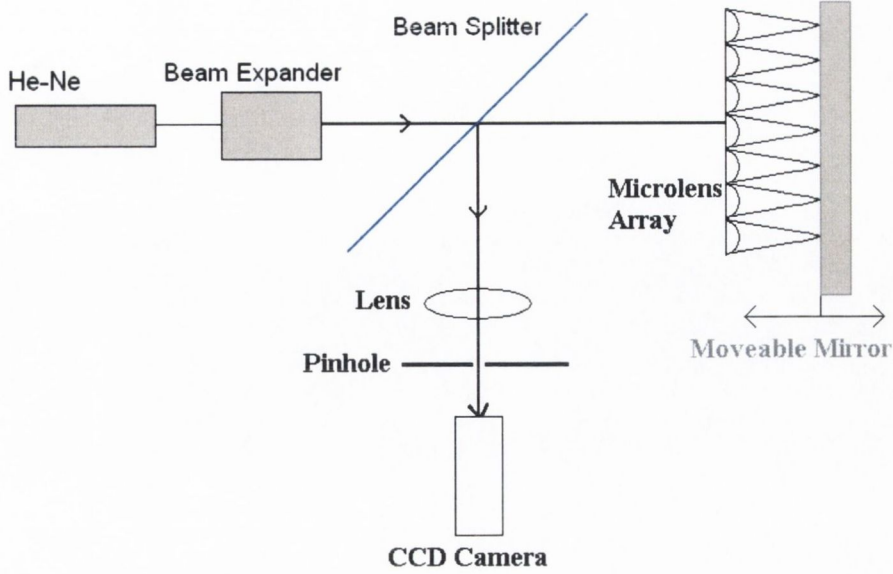


Figure 4.14. Experimental set-up for the investigation of the variable focal length microlens array as an array of objective lenses.

Using the familiar equations, derived by Wilson *et al.*⁷ for the axial intensity in a confocal microscope when imaging a plane mirror, the object scan was modelled.

$$I(u) = \left(\frac{\sin\left(\frac{u}{2}\right)}{u/2} \right)^2 \quad \text{Eqn. 4.1}$$

Here u is the normalised optical coordinate normally given by

$$u = \frac{8\pi}{\lambda} \Delta z \sin^2\left(\frac{\alpha}{2}\right) \quad \text{Eqn. 4.2}$$

$\sin(\alpha)$ is the numerical aperture of the lens when in air (refractive index of air taken as 1). λ , the wavelength of the light, is taken as 633nm and Δz is the defocus across the mirror. In the derivation for u there is an assumption that the defocus, Δz , is small compared to the focal length and that the distance from the lens to the object, $z \approx f + \Delta z$. This is true in the case of high numerical apertures with short changes of focal length but in our case a value for u that is more appropriate is

$$u = \frac{2\pi\alpha^2}{\lambda} \left(\frac{1}{f} - \frac{1}{z} \right) \quad \text{Eqn. 4.3}$$

This equation also allows the focal scan to be modelled as the value of focal length can be made to vary. The results are shown below, in Figure 4.15.

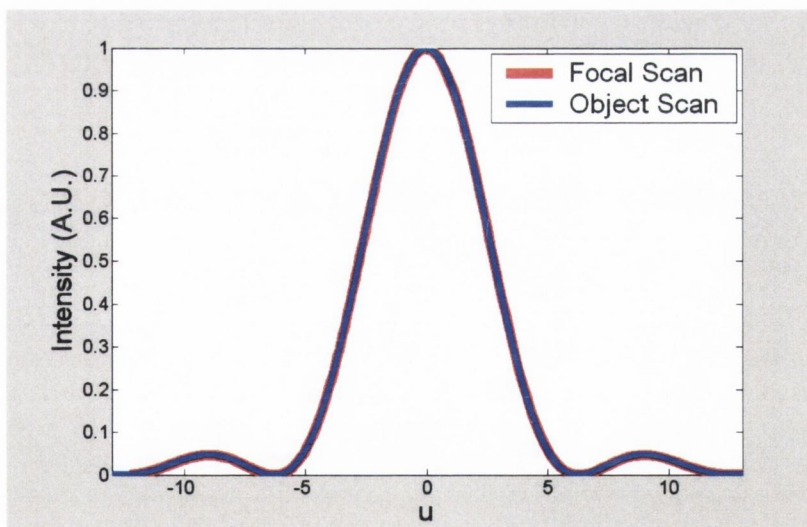


Figure 4.15 Axial responses for both the object scan and the focal length scan. The diameter is equal to $100\mu\text{m}$ and the distance from the lens to the mirror is taken as 1.44mm for the focal scan and the focal length has the same value for the object scan.

An object scan was carried out for these lenses with an applied voltage which resulted in a focal length of 1.44mm. Vast differences appeared between the shape of the experimental object scan and that calculated using Equation 4.1 as can be seen by comparing Figure 4.16 to Figure 4.15.

The asymmetrical shape can be explained by focal shift theory^{54, 55}. Focal shift theory accounts for the deviation of the symmetrical light distribution near the focal point of certain lenses. It occurs when the Fresnel number, N , of the lenses, given by Equation 4.4, has a finite value. In the case of microlenses this is often the case⁵⁵.

$$N = \frac{a^2}{\lambda f} \quad \text{Eqn. 4.4}$$

In the case of the lenses used in this study the Fresnel number is 4.2. The equations to model the axial scan must therefore be modified. Within the equation for the axial scan given by Equation 4.1 there is a multiplication factor that was excluded. The factor is named K . Where

$$K = \frac{\pi a^2}{\lambda z} \quad \text{Eqn. 4.5}$$

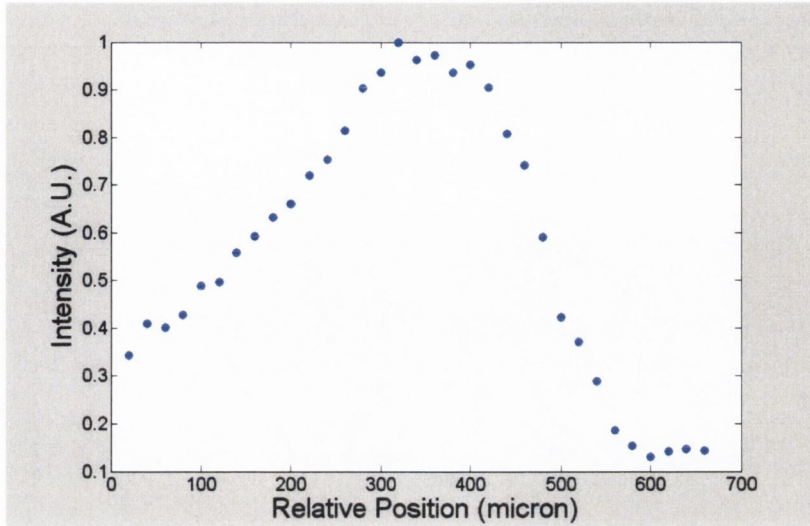


Figure 4.16 Measured axial response for an object scan with a focal length of the microlenses set to 1.44mm

This factor was not included in Equation 4.1, for the axial scan, as it is assumed it is quite large compared to $v^2/4$. The intensity is now calculated using the equation

$$I(u) = \left(\frac{2\pi a^2}{\lambda} \right)^4 \left(\frac{\sin(u/2)}{u/2} \right)^2 \quad \text{Eqn. 4.6}$$

With this equation the experimental results can be fitted to the theoretical model for the object scan as shown in Figure 4.17 below. Here we have added 1.01mm to all the relative positions, so that the relative position could be changed to the defocus and then calculated the normalised optical coordinate, u . We can see that there is a large background intensity which masks some of the lower intensity characteristics. This is due to back reflections at the

surfaces of the liquid crystal cell, particularly that of the chromium layer which is highly reflective.

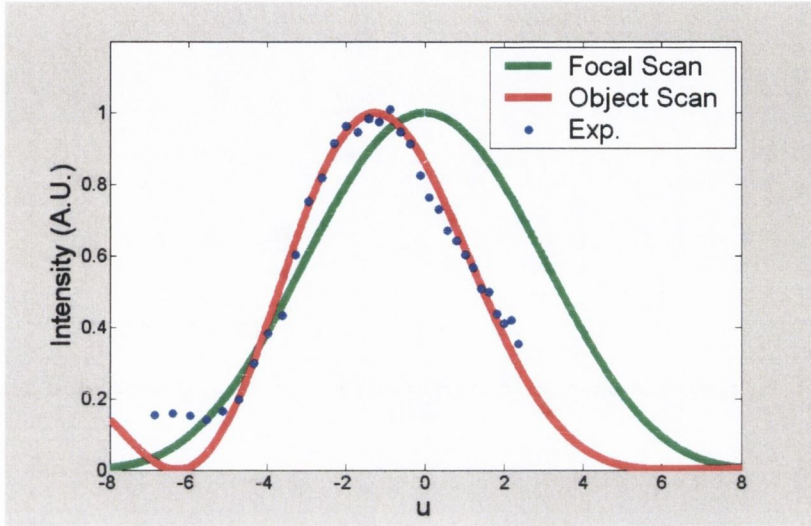


Figure 4.17. Axial response for both object (experimental and theoretical) and focal scans (theoretical)

Examining the axial response for the focal scans we found that there was no change with the use of the new Equation 4.6 for the focal axial scan. Although it is true that the axial response for the focal scans in Figure 4.17 and Figure 4.15 represents the amount of light collected from the defocused positions I do not believe this is an axial scan in the traditional sense, i.e. it is not a measure of the optical sectioning property of the microscope. As the focal length is changed it is then in the position that is imaged to the pinhole and as the focal length of the system has been changed the axial response at the new position, $I(u)$, will vary as it is dependant on the numerical aperture of the lens. Therefore at each position of the focal spot the microscope has a different response to the light from out-of-focus planes as can be seen in Figure 4.18 where the object scan is modelled for different values of the focal length. Here the

intensities have been measured against the distance from the lens to the object, z , as, u , is a coordinate normalised to the numerical aperture of the lens. The axial responses graphed have been cut-off at the position of first minimum so as not to obstruct the view of the other curves but are found to oscillate rapidly and have quite large side lobes which would degrade the final image.

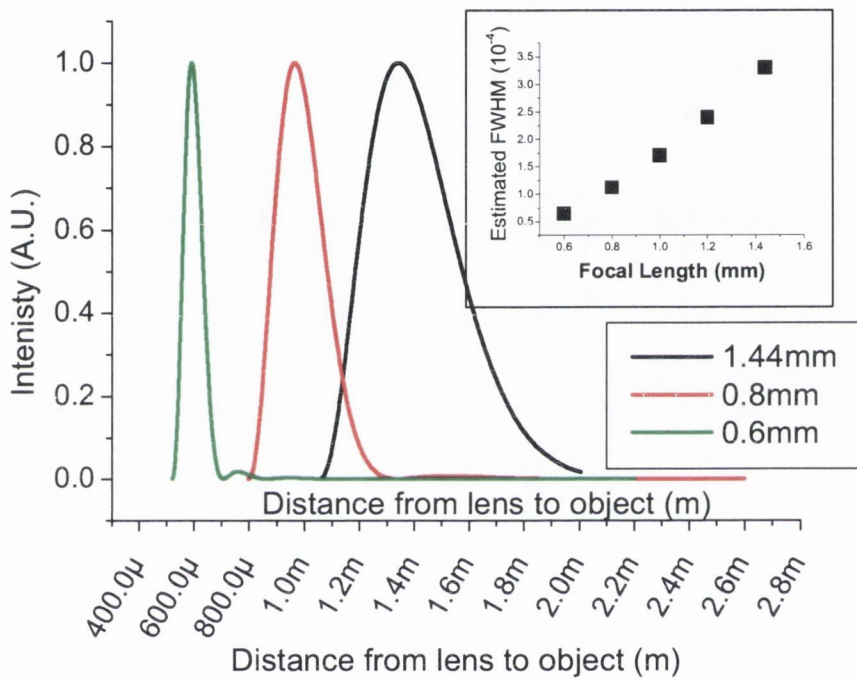


Figure 4.18. Modelled axial responses of object scans at different focal lengths achievable with the variable focal length microlenses.

Using a Gaussian fit the FWHM of the curves have been found for five different focal lengths and are shown in the inset of Figure 4.18. They are seen to increase linearly with increasing focal length as is expected from Equation 4.6. Focal scanning is still very applicable to confocal

systems as the focal length can still be varied to bring various depths of the sample into focus. However the axial response should be carried out in the traditional way to find the microscope performance at the individual focal lengths.

4.4 Conclusions

The use of VFL microlenses as an array of high throughput lenses has been shown. Most of the light incident on the array, $\sim 70\%$, is focussed by the lenses to an array of focal spots. These are shown to be implemented into a confocal system with a fibre bundle acting as a pinhole array. The lenses are shown to be well addressed to the fibre bundle. By varying the applied voltage across the LC lenses the focal spots are made to scan the mirror showing that light from defocused planes is indeed blocked by the fibres. The axial response for this scan is not a true measure of the optical sectioning as was discussed in Section 4.3. To utilise the focal scanning capabilities of the lenses another set of lenses with the same focal length variation would need to be applied to the end of the fibre. Another approach would be to use the fibres as the light sources as well as the pinhole array by mounting the VFL on the end of the fibre acting as an array of objective lenses.

The VFL lenses are shown to act as an array of objective lenses and their optical sectioning properties investigated. Focal scanning was introduced and investigated. It is shown that the depth response of the microlenses varies with the focal length of the system therefore a

practical instrument using these lenses would need a strict calibration of the intensities found from all the out-of-focus planes so that the results may be weighted accordingly. With higher quality and higher numerical aperture these lenses may very well be useful as an array of objective lenses where focal scanning is required.

Chapter 5

IMAGING AND SIZE DETERMINATION OF A SPHERICAL MICROCAVITY BY CONFOCAL FLOURECENCE MICROSCOPY

5.1 Introduction

Spherical dielectric microspheres can contain what are known as morphology-dependant resonances (MDRs). These occur when light propagates around the internal edge of the sphere due to total internal reflection at the surface. When the light propagates around the sphere in this fashion and closes in on itself in phase resonance occurs, as depicted in Figure 5.1. The light at these particular resonance wavelengths can then be confined inside the sphere with little losses due to total internal reflection and the low absorption of the dielectric materials usually used. This produces many interesting properties which are of interest to many disciplines. The confinement of light is both spatial and temporal. The spatial confinement is described by the mode volume (V) while the temporal confinement is described by the quality factor (Q), which is the photon storage time, normalized with respect to frequency⁵⁶.

MDRs are sometimes called ‘whispering gallery modes’ due to the resemblance to the reflection of sound waves around the inner walls of St. Paul’s Cathedral, which was dealt with by Lord Rayleigh⁵⁷.

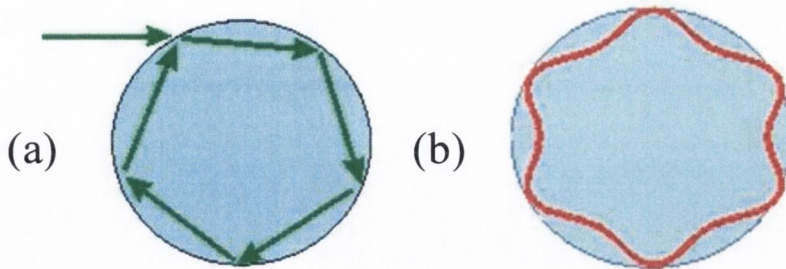


Figure 5.1 Schematic diagrams depicting a MDR in a sphere (a) in vector form and (b) in wave form

Whispering gallery modes are characterized by two polarizations, transversal electric (TE) modes and transversal magnetic (TM) modes, and three mode numbers n , l and m which are the radial, angular and azimuthal mode numbers, respectively. The value of l is close to the number of wavelengths that fit into the optical length of the equator. The value $l - m + 1$ is equal to the number of field maxima in the polar direction, i.e. perpendicular to the equatorial plane. The mode number n is equal to the number of field maxima in the direction along the radius of the sphere and $2l$ is the number of maxima in the azimuthal variation of the resonant field around the equator. The resonant wavelength is determined by the values of n and l which are in turn determined by the size and shape of the particle. The matching of the internal and external fields at the surface of the sphere relates the wavenumber of the resonant wavelengths to the mode numbers⁵⁶.

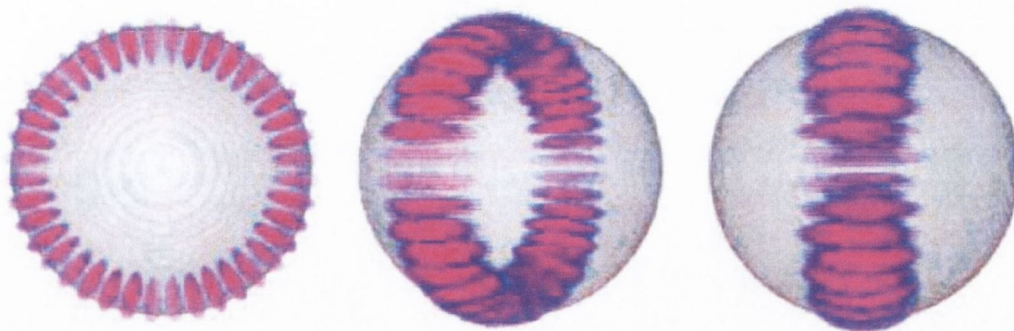


Figure 5.2 Schematic diagram representing a MDR with TE-mode and mode numbers $n=1$ and $m=1=20$ shown as the sphere is rotated.

As the name of these resonances suggests these are found to be highly dependant on the morphology of the sphere, namely the size and the refractive index.

5.2 Background and theory

Mie theory, also called Lorenz-Mie theory, is a complete description for the scattering of electromagnetic radiation by spherical particles⁵⁸. Gustav Mie and Ludwig Valentine Lorenz developed the theory from Maxwell's equation early in the last century. From this work the normalized extinction cross section for light scattering on spherical particles was found for different values of the wavelength. It was noted that this contained a 'ripple structure'. This was described by Van de Hulst as being due to some type of wave below the surface of the sphere⁵⁸. Petr Chýlek theoretically investigated this 'ripple effect' and found that it was due to resonances of the partial-waves as described by Mie theory⁵⁹. Using the size

parameter, $x_n = 2\pi a/\lambda_n$, he was able to calculate a formula for the periodic spacing Δx of the resonance peaks in the 'ripple structure. Here, a , is the radius of the sphere and λ_n is the wavelength of the resonance of mode order n . He found that they relied only on the relative refractive index of the material and its surroundings.

$$\Delta x = x_{n+1} - x_n = \frac{\tan^{-1} \sqrt{(m^2 - 1)}}{\sqrt{m^2 - 1}} \quad \text{Eqn. 5.1}$$

He found that these mode spacing were described separately by the electric and magnetic multipole coefficients of the scattered field giving rise to the TE and TM modes as described previously. These theoretical models predicted by Mie theory and investigated by Chýlek was later confirmed by experimental observation⁶⁰. Using radiation pressure a dielectric sphere was kept in levitation. A feedback loop was required to vary the radiation intensity from the laser to keep the sphere stationary. The wavelength of the incident radiation on the sphere was made to vary and the amplitude of the radiation power necessary to keep the sphere stationary was measured. When the radiation power was plotted against the size parameter a resonant change in the radiation pressure was found. As the optical force on the sphere arises from the scattering process it follows that this was an experimental observation of the resonant structure of the scattering process. As the size of the sphere was changed the resonant scattering structure varied. Using the experimental observation of the resonant structure along with the stringent theoretical Mie calculations a method of determining refractive index and size of the sphere was possible⁶¹. This produced many applications outside of determining the size of spheres by purely optical methods, for instance, as a temperature gauge. The size of many

dielectric spheres are temperature related and knowing the expansion coefficient the temperature can be calculated. The evaporation of droplets could also be investigated using this technique. We shall evaluate these techniques to see if the size of these spheres can be evaluated strictly from the spectral data.

To investigate the phenomena using inelastic scattering, dielectric sphere were impregnated with dye and the resonant structure determined⁶². Here the spectrally broad inelastic emission from fluorescent molecules within the sphere produced the resonant structure identical to those of spheres that were excited by varied wavelength incident light. This study will use similar set-up to this experiment with polymer spheres doped with dye.

Recently Chýlek *et al.*⁶³ noticed a discrepancy between his mode spacing as given by Equation 5.1 and the experimental results found for mode spacing of resonant peaks with large mode number, n . This led him to produce a modified equation which takes this into account.

$$\Delta x = x_{n+1} - x_n = \frac{\tan^{-1} \sqrt{(mx_n/n)^2 - 1}}{n \sqrt{(mx_n/n)^2 - 1}} \quad \text{Eqn.5.2}$$

The assumptions made in the derivation of both Equations 5.1 and 5.2, when the refractive index falls in the range of $1.2 < m < 2.0$, are

$$\begin{aligned} x &\gg 1 \\ n &\gg 1 \\ \frac{x}{n} &\sim 1 \\ mx &> n \end{aligned}$$

A further assumption that $|x - n| \gg 0.5$ was necessary for the derivation of equation 5.2. When this does not hold, Equation 5.1 is no longer valid and Equation 5.2 is to be used. The accuracy of the derived expressions of equation 5.1, if $|x-n| < 4$, and of equation 5.2, if $|x-n| \geq 4$, is within 1% comparing with the exact Mie numerical calculation⁶³. These equations and conditions will be investigated to determine the size of dye-doped polymer spheres by analysis of their spectral data.

There has been much research carried out into the use of MDR supporting microspheres as microcavities for lasers⁶⁴. A good cavity is essential to every laser as this is where the gain medium is placed and the light amplification occurs. Microspheres are interesting because of their small size and the large optical path length of the confined light inside the sphere due to the many of total internal reflections. One of the defining characteristics of a cavity's performance is the quality factor or Q factor. As was outlined in the introduction, the Q factor describes the temporal confinement and is given by the equation⁶⁵

$$Q = \omega\tau \quad \text{Eqn. 5.3}$$

Here τ is the lifetime of the light energy in the microsphere and ω is the frequency multiplied by 2π of the mode. The lifetime will be due to, amongst other factors, the amount of reflection at the surface of the cavity and the absorption or damping in the material. In polymer spheres the decay of the field is limited by Rayleigh scattering and absorption⁶⁵. These issues will lead to the broadening of the emission modes⁶⁶. It is not surprising therefore that the Q factor can also be determined by the ratio of the frequency of the mode to the full width at half maximum (FWHM) of the Lorentzian fit of the mode emission, as shown in Equation 5.4. It is therefore

possible to find the Q factor and the temporal confinement of photons inside the sphere from analysis of the emission spectra.

$$Q_n = \frac{\omega_n}{FWHM(\omega_n)} \quad \text{Eqn. 5.4}$$

5.3 Experimental set-up

Figure 5.3 shows the experimental set-up for fluorescence imaging and emission spectrum measurements. An Ar⁺ (457.9nm) laser is focused onto the microsphere samples through an objective lens with a high numerical aperture (NA) of 0.9. Only light of emission wavelength above 515nm from the sample can pass through the filter cube, which includes an excitation filter, a dichromatic mirror and a barrier filter. By flipping the mirror M1, the light can be input into either a scanning microscope with a photomultiplier tube or a spectrometer (Oriel Multispec 77400) with a cooled CCD camera (Andor Tech., 0.5nm spectral resolution). The experiments are performed on highly transparent polymer microspheres stained with Ethidium Bromide (EtBr) dye. Similar polymer microspheres which did not contain dye but were coated by a thin layer of Cadmium telluride (CdTe) quantum dots were also investigated by the confocal set-up.

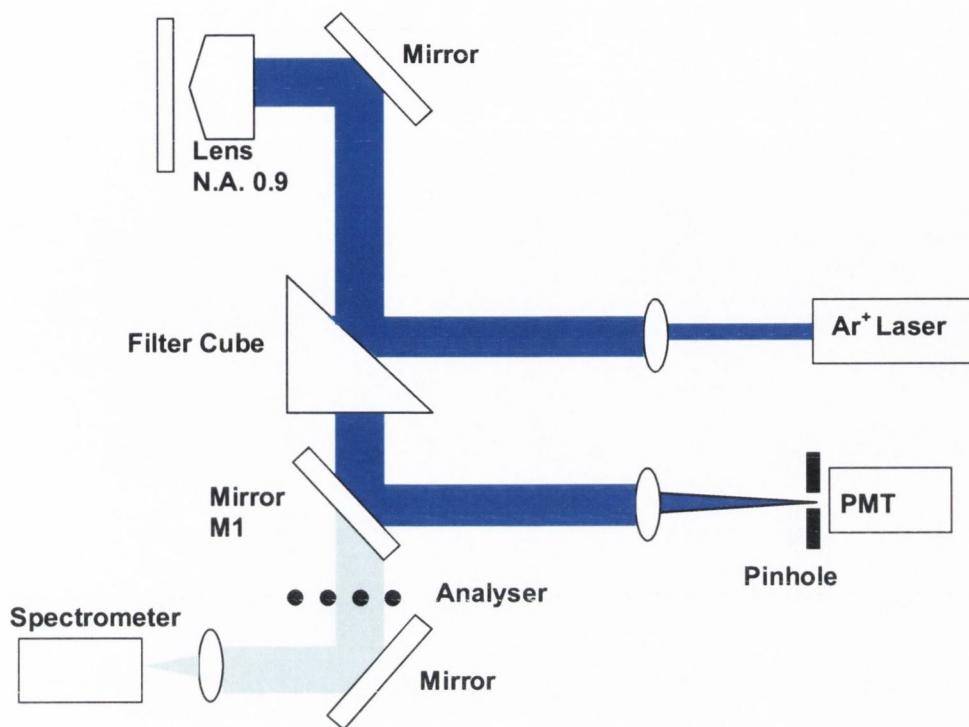


Figure 5.3 Schematic diagram of experimental set-up, M1 is a removable mirror

The fluorescent labelled microspheres are produced using simultaneous particle formation (polycondensation process) and dye incorporation. The sample studied has a diameter, D , of $5.09\mu\text{m}$ with a size deviation of $0.09\mu\text{m}$ (Microparticles GmbH, Germany). The size distribution is given by the manufacturer using an electrical sensing zone method with special high resolution measuring capillaries. The refractive index, m , of the microsphere polymer is 1.680. According to the specifications, the dye concentration is rather low compared to the particle mass ($<0.1\%$ wt.), thus there is no significant change in the refractive index of dye-doped microspheres. The fabrication of the polymer spheres coated by CdTe quantum dots was undertaken Rakovich *et al.*⁶⁷. A layer by layer approach (see Section 7.3.2) was used to coat the spheres. The CdTe nanocrystals are capped with thioglycolic acid during synthesis⁶⁸

which gave them a negative charge. This negative charge along with the surface charge on the spheres and some polyanion and cation solutions it was possible to fabricate high quality coated microspheres. The microspheres of both types were made with melamine formaldehyde (MF). These type of microspheres have a high optical transparency, high thermal and mechanical stability and a high refractive index ($m=1.68$) making them ideally suited to the examination of MDRs.

5.4 Confocal Imaging

Three-dimensional imaging of the CdTe coated microspheres was achieved with the set-up shown in Figure 5.3. The images obtained are shown in Figure 5.4. An isolated sphere and a pair of touching spheres were imaged. The stage was first moved so that the focal plane of the high NA objective lens was in the sample plane as the substrate on which the microspheres were placed. A raster scan in the x and y direction was performed, to produce the image shown in Figure 5.4(a), where the shadows of the sphere can be seen. When the focal plane was moved toward the equatorial plane of the sphere and an image taken, bright rings appeared in the periphery of the sphere, Figure 5.4(b). Since the distance from the equatorial plane to the substrate is about $2.6\mu\text{m}$ and the FWHM of the system axial response of $\sim 0.8\mu\text{m}$ is considerably less than this, light from the off-focused substrate will be blocked by the pinhole. In addition, other light scattering away from the focus will be also blocked by the pinhole. Hence bright rings can only be due to the light backscattered from the focused point of the sphere surface.

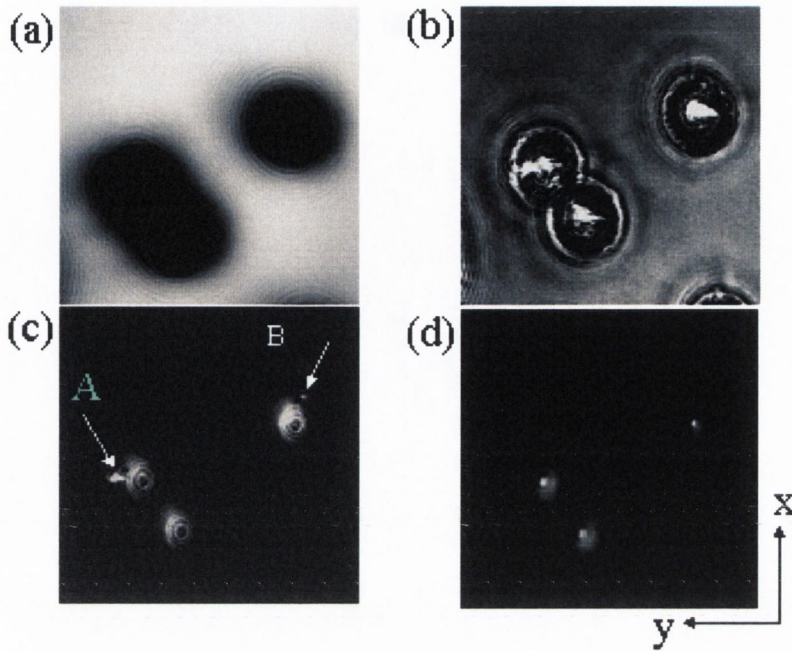


Figure 5.4. Normalised confocal scanning images of microspheres, $5.2\mu\text{m}$ in diameter, with different axial locations. From (a)-(d): $z = -a, 0, a/2,$ and $a,$ respectively. Two defects A and B are inside the sphere.

The bright centre in Figure 5.4(b) can be explained in terms of geometrical optics. The light incident on the centre of the sphere travelling along the optical path is reflected back along the optical axis, as shown in Figure 5.5. To observe the side rings in Figure 5.4(c) the gain was increased which saturated the image at the centre of the sphere. Figure 5.4(c) shows the images taken when the focal plane of the microscope is placed in the middle of the top half of the sphere. Scattered light arising from defects in the microsphere surface are evident and marked A and B in the image for clarity. The final image is a raster scan taken

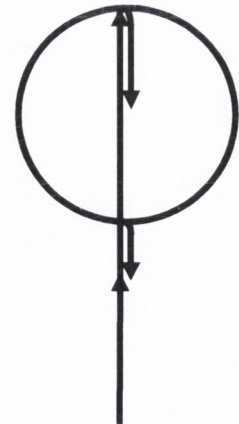


Figure 5.5

with the focal plane incident with the top of the spheres. A slight difference in the size of the spheres is evident from this image from the amount of scattering present.

5.5 Spectral analysis and size determination.

Figure 5.6(a) shows the emission image of a single microsphere with homogeneous photoluminescence distribution, taken with the pinhole removed from the optical set-up, i.e. with conventional microscopy. Figure 5.6(b) show the images of two other spheres with a bright spot at the edge and a tail opposite. The images have been investigated spectrally to make sure that the signal from the laser light is lower than -20dB.

This image is comparable with the microspherical lasing report produced by Fujiwara *et al.* in which they excited only one edge of the glass microsphere, emission can be observed at both edges of the sphere opposite each other. We notice that there are no obvious interference rings inside the sphere in the emission image compared with the bright field image shown in Figure 5.6(c) where the back scattered laser light is detected. This is due to the incoherent property of fluorescence light.

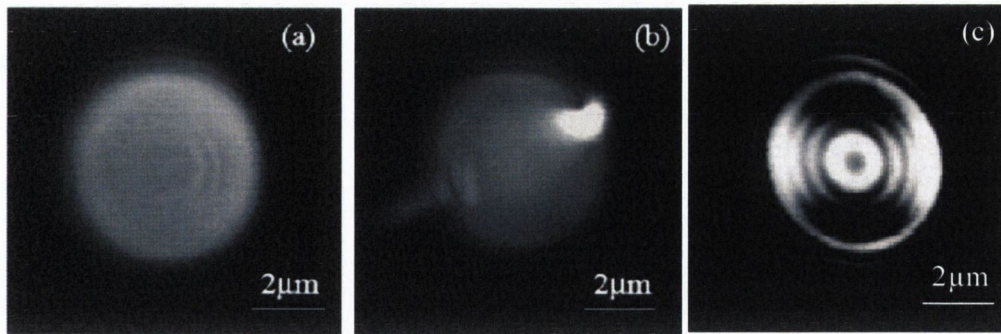


Figure 5.6. Emission images of two microspheres (a) and (b), when the pinhole is removed the conventional microscopy image is shown in (c).

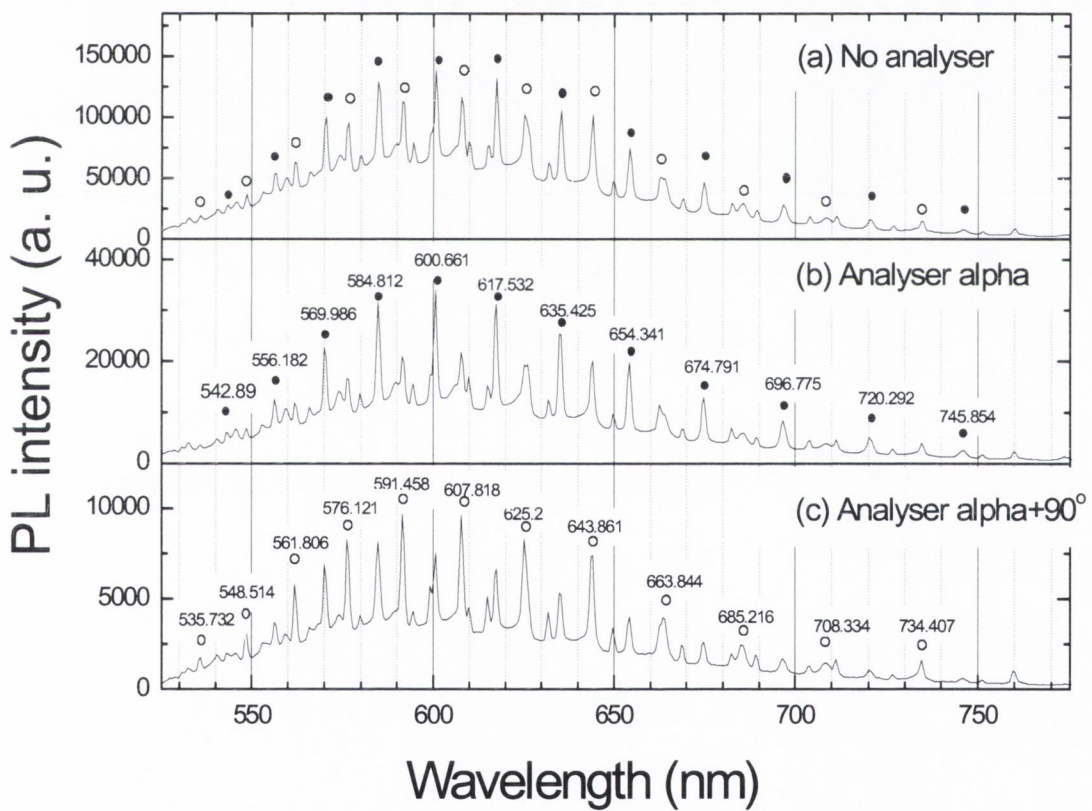


Figure 5.7. MDRs in a dye-doped microsphere. Solid circle: TE modes. Open circle: TM modes. (a) no analyser; (b) and (c) with the analyser at angle α and $\alpha + 90^\circ$ respectively. (b) A modes are quenched and (c) B modes are quenched.

The imaging system allows us to focus the beam onto the sphere with submicron spot size. By removing mirror M1 away from the light path, the emission spectrum from the edge of the microsphere was measured, shown in Figure 5.7(a). In this case, no analyser was used. The envelope of the fluorescence spectrum ranges from 525nm to 775nm giving a centre wavelength of ~ 600.5 nm. TE modes are found at lower wavelength values of the spectrum. Sharp peaks were observed within the envelope of the spectrum. The structural peaks have been explained in terms of the resonant optical modes. Mode quenching due to absorption of EtBr dye can be observed below 570nm, shown in Figure 5.7.

This is shown in by the emission and excitation wavelengths of EtBr in Figure 5.8, taken from reference material on the Invitrogen® website, where there is overlap between the excitation and emission spectra.

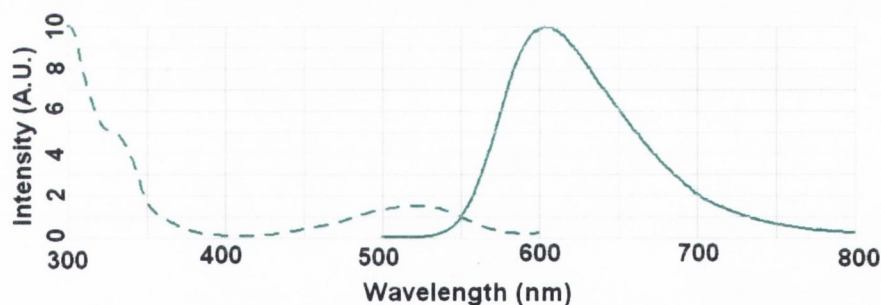


Figure 5.8: Absorbance (dashed line) and photoluminescence (solid line) spectra for EtBr.

Using Equations 5.1 and 5.2, $\Delta\chi$ is calculated. Equation 5.1 is reliant only on the refractive index while Equation 5.2 needs estimated values for both the radius and the mode number. With these values of $\Delta\chi$ the difference in wavelength between the resonance peaks can be found using Equation 5.3.

$$\Delta\lambda = \lambda_n - \lambda_{n+1} = \frac{\lambda_n \lambda_{n+1} \Delta x}{2\pi a} \quad \text{Eqn.5.3}$$

The fit of these values, using the estimated values for the radius of the spheres and the mode numbers, is found in respect to the experimental wavelength difference, $\Delta\lambda(\text{exp})$.

$$\Delta\lambda(\text{exp}) = \lambda_n(\text{exp}) - \lambda_{n+1}(\text{exp}) \quad \text{Eqn.5.4}$$

This is done using the method of least squares as shown in Equation 5.5. The criterion set forth by Chýlek *et al.*⁶³ are applied when choosing which data points are included in the fit. When $|x-n| < 4$, Equation 5.1 is applied and the difference between the calculated and experimental data is found, d_1 . When $|x-n| \geq 4$, Equation 5.2 must be applied and the difference, d_2 , is again found by the method of least squares as shown in Equation 5.5, where $c=1,2,\dots,n$

$$d_c = \sum [\Delta\lambda(\text{exp}) - \Delta\lambda(\text{eqn}_c)] \quad \text{Eqn.5.5}$$

The fit value is then given by the summation of these differences, $d_1 + d_2$. By minimising the fit we found the values of the mode numbers of the resonances and the radius of the sphere. As an initial starting position the size of the sphere was estimated from the image in Figure 5.6(a), $\sim 4.90\mu\text{m}$. For the mode number the assumption used in the derivation of the Equations 5.5 and

5.6, namely $x \sim n$, is employed. Therefore, the largest mode number taken was 29. The fit of the curved for peaks A and B are shown below in Figure 5.9.

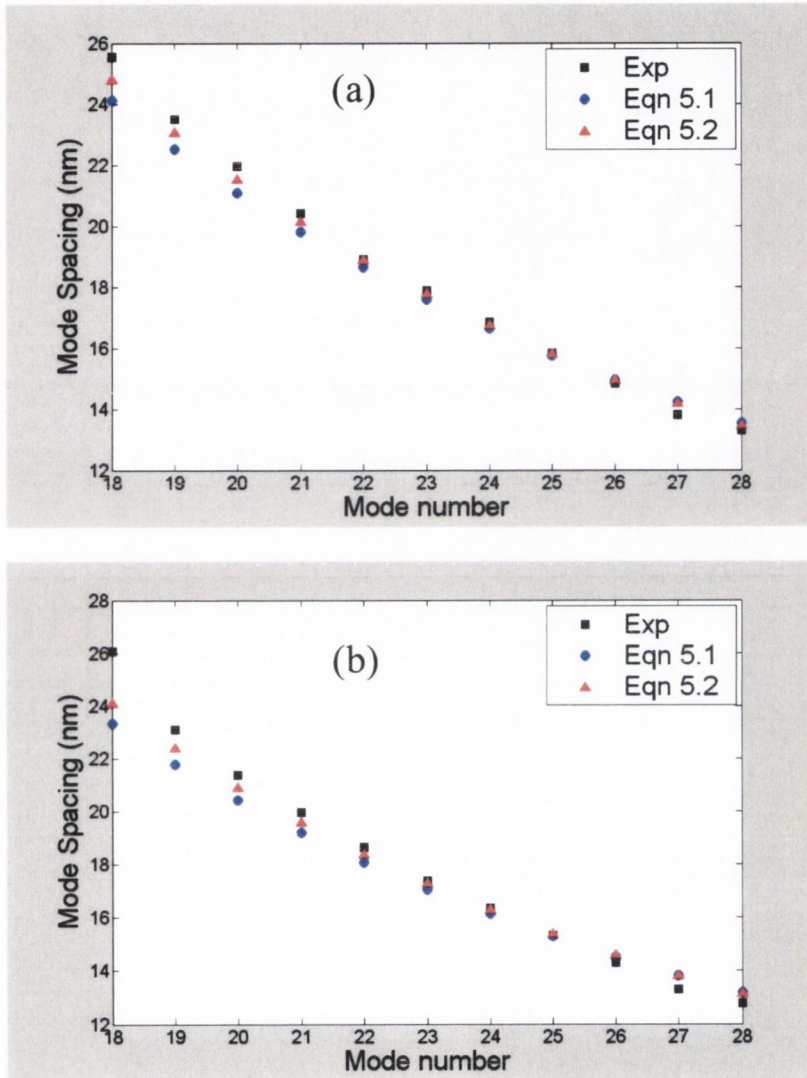


Figure 5.9. Fit of the experimental mode spacing for a sphere diameter of $4.90\mu\text{m}$ and the theoretical results calculated by Equations 5.1 and 5.2, graphs (a) and (b) are for TE and TM peaks respectively.

The fits calculated for these sets of data are 4.6247 and 11.6205 for peak sets A and B respectively. The mode number is varied to minimise the fit value. The results found are tabled below.

Mode Numbers	TE Peaks Fit Values	TM Peaks Fit Values	Average Fit Value
31	2.491	11.6205	7.05575
30	2.491	11.6205	7.05575
29	2.491	11.6205	7.05575
28	2.491	11.6205	7.05575
27	1.5443	3.5673	2.5558
26	1.065	2.2604	1.6627
25	3.5704	4.5813	4.07585
24	7.109	7.4241	7.26655
23	10.9318	10.8129	10.87235

Table 5.1 Values for the fit of the experimental data to the calculated data for different values of the highest mode number.

It is clear from Table 5.1 that the highest order has a mode number of 26. Using this value for the mode number we calculated the radius of the sphere. Using Matlab® it was possible to perform many such data fits as those shown in Figures 5.9 simultaneously, see Appendix B for program written. The fit values for each curve were then graphed against the radii chosen and the minimum found. Figures 5.10(a) and (b) show the calculated fits for values of 2400nm to 2700nm for the sphere radius for TE and TM peaks respectively.

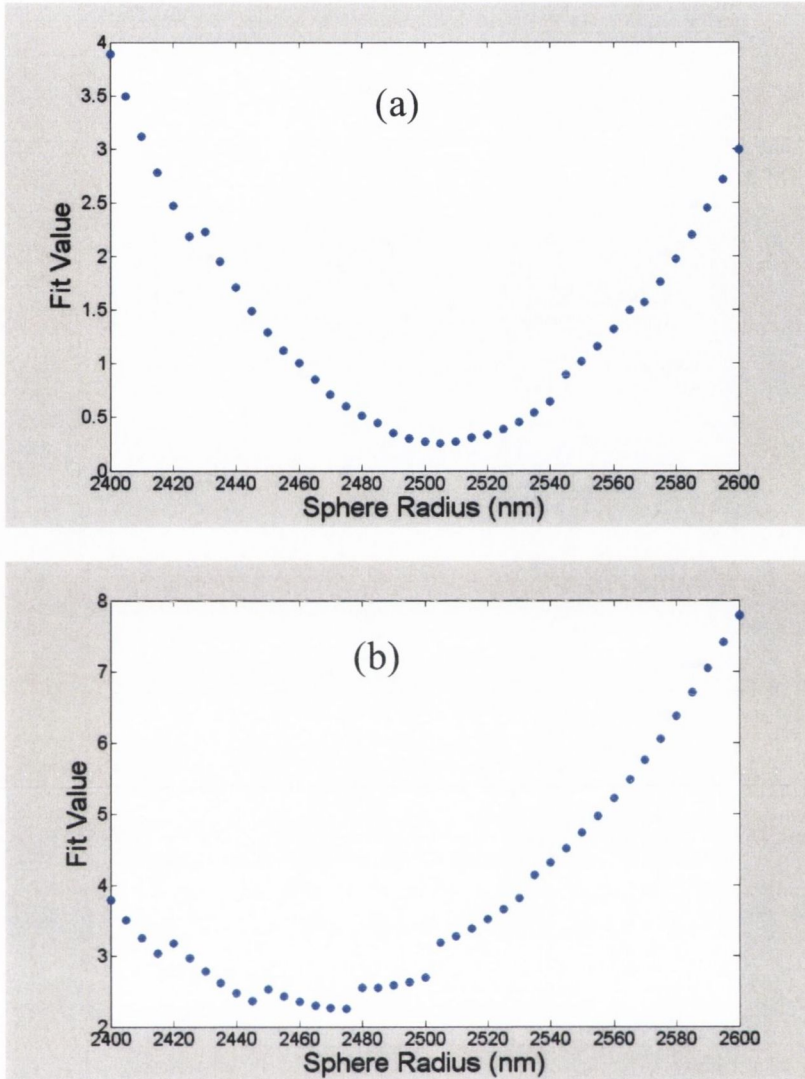


Figure 5.10. Calculated fit values for the experimental data and the theoretically calculated data for (a) TE peaks and (b) TM peaks. The minimum fit value corresponds to the true radius of the sphere as determined by the fitting method.

The minimum value for the sphere radius is found at 2505nm, for the TE peaks, giving us a sphere diameter of $5.01\mu\text{m}$ well within the range specified by the manufacturer. The minimum fit value found for the TM modes was at a value of 2475nm giving a sphere diameter of

4.95 μm . This seems a little low; also it is quite clear that the diameter calculated for both peak sets should be the same. The fit to Equation 5.1, where $|x-n| < 4$, i.e. mode numbers 23-25, and equation 5.2, when $|x-n| \geq 4$, i.e. mode numbers 15-22, shows a good result for the TE peak set but not for TM.

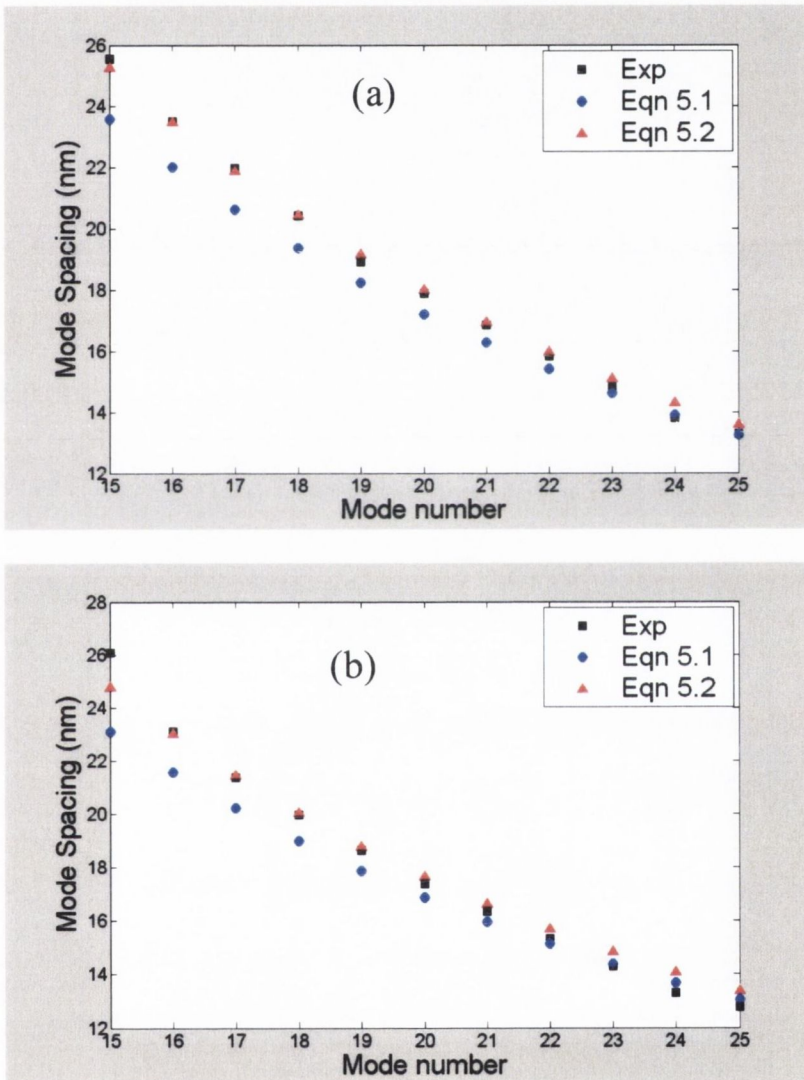


Figure 5.11 The improved fit of the experimental data to the calculated data using the sphere radius as found by the fitting method excluding peak modes that were not clearly distinguishable.

For $n=15$ in peak set B there is a large discrepancy between the calculated and experimental results. From Figure 5.7 it can be seen that the peaks at 708nm and 734nm are not very well defined and there may be some overlap. By removing these peaks from the calculation a value of 2500nm is found for the radius, 5.00 μm diameter. Figure 5.11 graphs the values calculated using the values found for the mode number and the sphere radius against the experimental data. The fit value decreases from 2.2438 to 0.4280 when the two smallest modes are excluded.

Figure 5.12 shows the spectrum from another randomly chosen dye-doped MF microsphere. Using the same approach as outlined above the size of the microsphere is determined to be 5.11 μm in diameter. The spectrum is red shifted as well as compressed when compared with that in Figure 5.7 due the size variation of the sphere. This is explained by using the equation $2\pi a \cong n\lambda$. For the same mode number n and peak type, the size of the two spheres should satisfy $a_1/a_2 = \lambda_1/\lambda_2$. Here the ratio of two studied sphere diameters is 0.97847. We chose modes TE₁₈, TE₂₂ and TE₂₆ and calculated $\lambda_1/\lambda_2 = 0.97838, 0.97891$ and 0.97915 for the two spheres, which shows good agreement with the size ratio. On the other hand, for the same mode number distance and wavelength range, the mode spacing $\Delta\lambda$ of the two spheres should satisfy $a_1/a_2 \cong \Delta\lambda_2/\Delta\lambda_1$. In Figure 5.7 (a), we chose TE₂₅ and TE₁₇, and in Figure 5.12, we chose TE₂₆ and TE₁₈, where the mode spacing ratio $\Delta\lambda_2/\Delta\lambda_1 = 0.9620$. Again, it shows good agreement with $a_1/a_2 \cong \Delta\lambda_2/\Delta\lambda_1$.

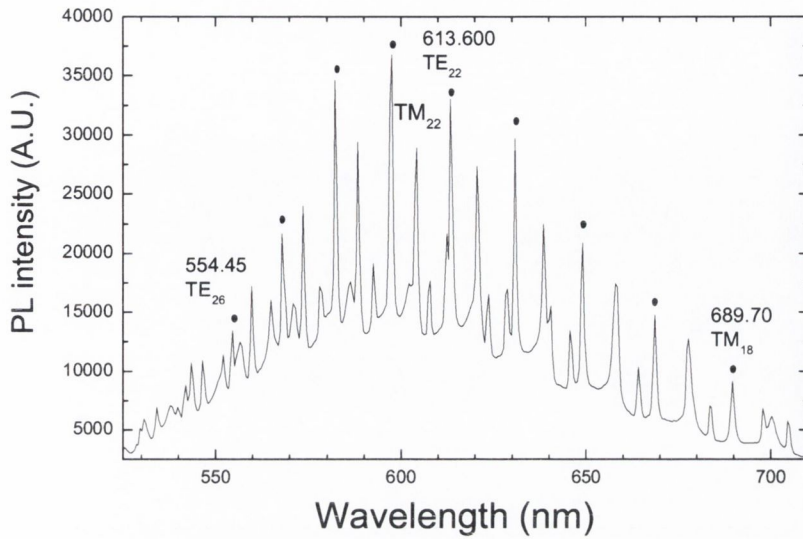


Figure 5.12. Mode spacing vs. and mode number of A (a) or B (b) modes. The determined diameter of the microsphere is 5.11.

As was described in the theory section of this chapter it is possible to find the Q factor of the sphere at each wavelength of emission. The Q factor describes the normalized energy dissipation in a cavity; it can therefore be described as $Q = E/\Delta E$. The Q factor was found by selecting the mode and removing the background luminescence intensity. The peak was then fitted by a Lorentzian curve and the peak position and FWHM read.

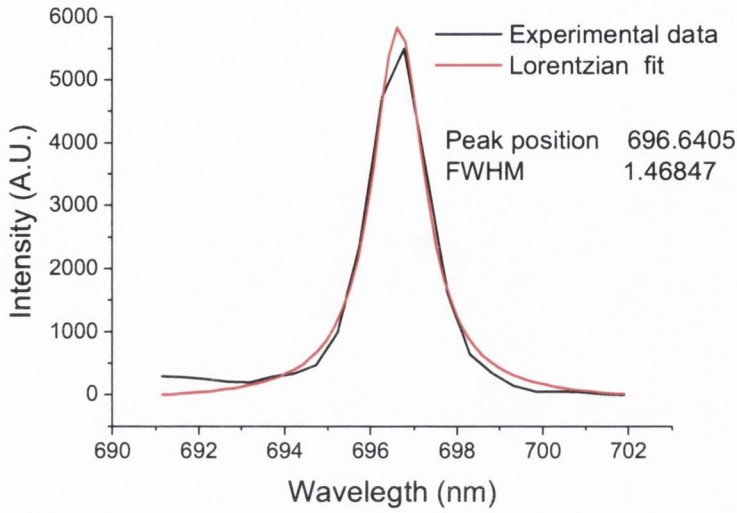


Figure 5.13. Peak intensity for a single resonance mode and its Lorentzian fit.

By multiplying Planck's constant, h , the electron volt, e , and the speed of light, c , we get

$$(h)(e)(c) = 1.24 \cdot 10^{-6} \text{ Eqn.} \quad 5.5$$

This can then relate the energy of a photon to its wavelength in μm .

$$E = \frac{1.24}{\lambda} \quad \text{Eqn. 5.6}$$

By differentiating E with respect to λ and rearranging we get

$$\Delta E = \frac{(E)(FWHM)}{\lambda} \quad \text{Eqn. 5.7}$$

By using these relations the Q factor was calculated from the spectrum of the resonance mode. An average value of ~ 500 was found for the A type peaks. The temporal confinement can be calculated from the Q factor using the equation, $\tau = Q/\omega$. The Q factor for a peak at 635nm

was found to be 757, the average lifetime of a photon at that wavelength was then calculated as 0.26ps.

5.6 Conclusions

Melamine formaldehyde microspheres coated with CdTe nanocrystals were investigated using confocal microscopy as a method of defect analysis and surface defects were found when they acted as scattering points on the surface of the sphere.

Melamine formaldehyde microspheres were investigated under conventional scanning microscopy and their emission properties analyzed. By fitting the experimentally measured mode spacing to theoretical equations the size of the sphere was determined. The sizes determined using this purely optical method seemed reliable as they fell within the size specifications as given by the company and their testing methods.

From the spectra the Q factors for the spheres were also determined and the temporal confinement at certain wavelengths was also calculated. This is important if these microcavities are to be considered to be useful in laser applications.

The fits from the two graph sets in Figures 5.9 and 5.11 for the TE and TM modes and the final values are tabled below for reference.

Mode numbers	Sphere radius (nm)	Fit value	
		Peak set A	Peak set B
28-18	2450	4.6247	11.6205
25-15	2505	0.2556	
25-15	2475		2.2438
25-17	2500		0.4280

Table 5.2 Fit values for sphere sizes found using the methods outlined

Chapter 6

Imaging with incoherent fiber bundles

6.1 Introduction

Fiber optics are predominantly used in optical communication but are also heavily used in imaging applications. Research into imaging with fiber optics predates that of telecommunications and spurred the development of optical fibers in the early years of the technology. The employment of total internal reflection to guide light along a stream of water was first shown by Daniel Collodon and Jaques Babinet in the 1840s. It found its first application in lighting up large fountains of water at the Universal Exposition in Paris in 1889⁶⁹. The concept was transferred to glass where it was first used in the fabrication of dental tools. Bent quartz rods were used to illuminate the back of the mouth. In the 1930s Heinrich Lamm, a medical student in Germany, was the first person to transmit an image through a fibre bundle⁶⁹. The quality of the transmitted image was poor due to the loss of light and also an addition of light from other sources outside of the original source. This problem was later solved by wrapping the fibres in plastic or cladding. This brought about a dramatic increase in the quality of the images and the distance over which light could be carried, (this heralded the dawn of fibre optics in telecommunications). By 1954 imaging bundles had been reported in *Nature*⁷⁰ and by 1957 the first trial of a fibre-optic endoscope was tested by Basil Hirschowitz who swallowed his device himself. Imaging bundles are now commonly used in medical in-vivo imaging, non-invasive surgery and in industry.

A group of 'thick fibres', between 37 to 169, are placed together and heated until they become soft, they are then stretched out to form a rigid multifiber about 2mm in diameter. A number of multifibers are bunched together and again heated and drawn to produce a rigid fibre bundle containing thousands of fibres; each fibre is now 3 to 20 μ m in diameter. The numbers of fibres given are chosen so as to pack them neatly and tightly together. The ends of the rods are covered and the rest of the bundle dipped in acid that dissolves the outer layer leaving a flexible bundle of thousands of fibres which are arranged so that their ends are aligned for imaging. The ends of the fibres are then polished and the fibre is ready for integration to an endoscope or any remote imaging application.

6.1.3 Imaging with incoherent bundles

As was shown above the fabrication of coherent fibre bundles is a very costly and strenuous process which must be heavily controlled. By removing this process and imaging with incoherent fibre bundles the cost of remote imaging applications could be drastically reduced and the system made more versatile.

The individual fibres in an imaging bundle can be thought of as pixels, each pixel being an intricate part of the full image. If an incoherent bundle is used as an imaging bundle the pixels will be out of position at the image end of the fibre thus destroying the image. By noting the position of the fibre bundles at the each end of the fibre a 'map' of the entrance and exit pupils can be built up. Using this map the light emitted from each individual fibre in the bundle can be moved to the position corresponding to its entrance fibre thus recreating the image. The

with a large numerical aperture (N.A.) are needed. A large refractive difference between the thin core and of the fibre and its cladding allows for a large N.A.

6.1.2 Fabrication

There are two main methods used for the fabrication of coherent fibre bundles. The first is done by winding a single long fibre around a drum moving each loop to the side of the last, tight against the drum. When the drum has been filled with a line of fibres a section is glued. After being dried this section is cut in half, producing a complete fibre bundle. This is a simple process in concept, but far more demanding in practice when using thin fibres which are brittle and likely to break.

The second and more widely used method is the drawing of heated fibres together. A 'thick fibre' one which has an extra layer of cladding, of a large diameter, is shown in Figure 6.1.

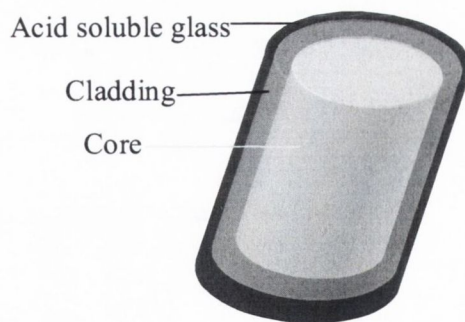


Figure 6.1. Schematic of 'thick' fibre.

6.1.1 Imaging bundles

When fibres are brought together into bundles they fall into two main categories, coherent and incoherent. Coherent bundles are those in which the positions of the individual fibres with respect to each other are fixed at either end. It is these bundles that are used in imaging applications. There is no control over the positions of the fibres inside incoherent bundles and these are used as light guides. Coherent bundles can be broken down further into two main categories, rigid and flexible. The disparity is that the fibres in the rigid bundles are fixed in position along its length whereas in the flexible bundles, the fibres are fixed only at the ends. Rigid bundles are generally shorter and fatter, used for transmitting or magnifying images piece by piece and other inspection and optical techniques. Flexible bundles are more widely used, employed by remote imaging and endoscopy. It is with these type bundles with which we shall be concerned.

For high quality imaging with fibre optics there needs to be many fibres in each bundle with as small a diameter as possible. Typically a bundle's resolution is approximately half a line per fibre core diameter. Numerically this means that for a bundle with fibres of core diameter $10\mu\text{m}$ the bundle could resolve approximately 50 lines per mm or 1 line per $20\mu\text{m}$. Thin fibres are widely used for optical communications as they are typically single mode fibres which greatly reduce pulse dispersion. However they are not suited to imaging bundles as they are difficult to couple light into. Remote imaging is habitually used in places of low light and the bundle must be placed close to the object under inspection therefore it is favourable to be able to couple as much light to the fibre as possible. Therefore thin fibres which are multi mode

incoherent fibre bundle can then be used in conjunction with the map and software to recreate the image. There are some things that would be necessary with such bundles, for instance the bundle would need to be placed in exactly the same position with each use. It would also be necessary to image the fibre bundle onto the camera in the same fashion as the map was created. This could easily be done by using precise connectors on the bundle ends.

This process would reduce the manufacture cost of the bundles. It may have other advantages, such as in endoscopy. Imaging bundles in endoscopes must undergo rigorous treatment between each use and have precise storage criteria, further increasing the cost, if they were to be replaced by much cheaper incoherent bundles the endoscopes bundles could be made single use which would make the process not only cheaper but far more flexible.

6.2 Fibre bundle mapping.

To 'map' the fibre bundle the position of each individual fibre in the bundle at each end must be known. This was done by using the set-up shown in Figure 6.2. The light source used was a fibreised Xenon arc lamp. The light from the fibre source was made to overfill an objective lens which then focussed the light to the face of the fibre bundle. The light from the distal end of the fibre is imaged to a CCD camera. The objective lens which focuses the light to the face of the fibre bundle was attached to a Thorlab's® Nanomax flexure stage. This was set to raster scan the spot of light across the fibre bundle face.

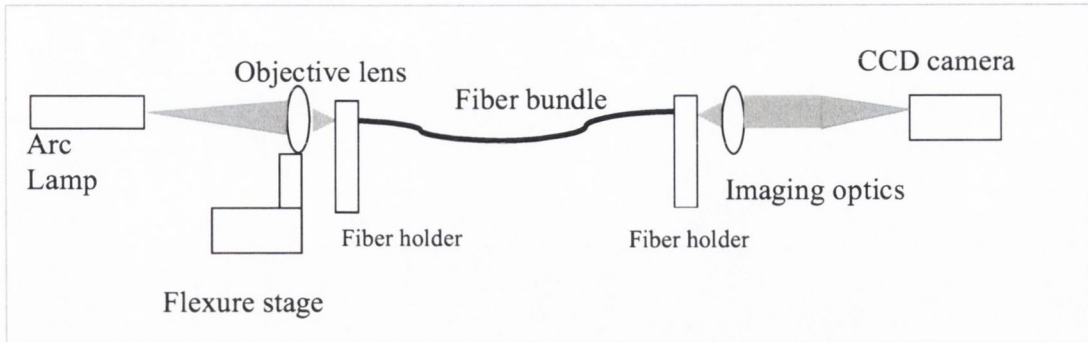


Figure 6.2 Experimental set-up for the mapping of an incoherent fibre bundle

After capturing an image, the camera is set to send a trigger pulse to the objective translational stage to initiate a move in the raster scan. There was a time delay then set on the camera to take another image after the move was completed. The step size of the raster scan is set at a distance smaller than that of the fibres in the bundle to ensure that the light is well coupled to each individual fibre. The incoherent bundle used in this study was a fibre bundle light guide. This had an outer diameter of 6.3mm with individual fibres of 50 μ m diameter and a packing fraction of 82%. The light guide ends were tightly bound in metal jackets and the fibres ground and polished by the manufacturer. This introduced a problem for the experiment as we had to image the light into single fibres. The fibre bundle had to be cut with a razor blade and held together with tape. This caused some additional issues. The incoherent bundle should be perfectly flat along the surface into which the light is to be coupled. Microscopic images of the entrance and exit ends are shown in Figure 6.3.

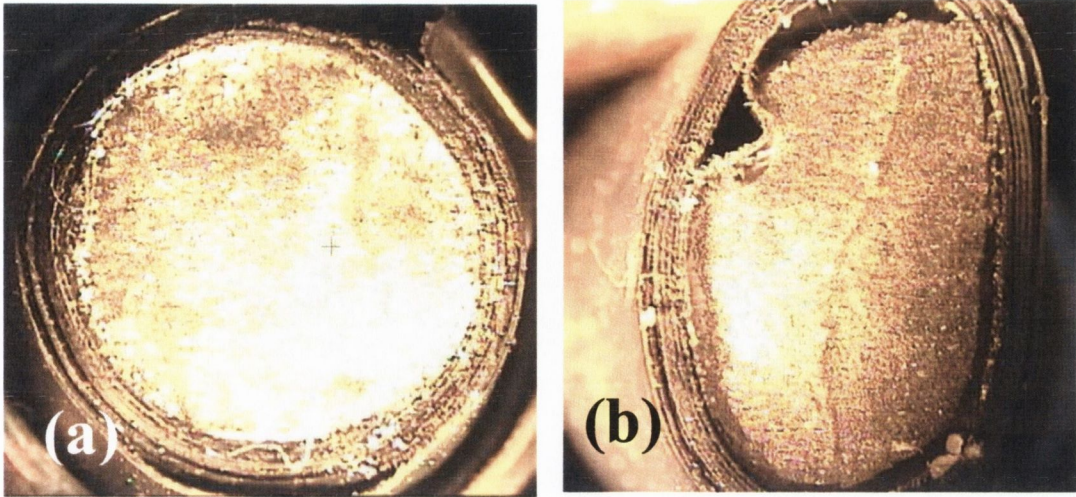


Figure 6.3 Microscopic images taken of the entrance (a) and exit (b) ends of the fibre bundle.

It can be seen clearly that the fibres in the bundles are not flat across the surfaces. It was therefore impossible to focus the light into each fibre in the bundle and many fibres were omitted from the mapping file. The fibre diameter is larger than that of the maximum travel range on the stage and a circular aperture of 4mm in diameter was placed tight with the fibre bundle face and only the fibres inside this had light transmitted to them.

An image was taken at each position in the raster scan. Using Image Pro-Plus®, it is possible to find the position of the bright spot, measure its intensity and its area. By measuring its intensity and its area it is possible to disregard images with spots of light that are the result of light being coupled across two or more fibres. For the spots that are well defined the centre position is given in pixel positions (x_2, y_2) and is read out into a mapping file. These pixel positions can be related to image number which is in turn related to the scan position of the fibre, (x_1, y_1) , noted in the mapping file. Using programs, we wrote specifically for this

purpose, with Visual basic® it was possible to automate this process for a large number of images resulting in a map file with all of the input and output positions for the individual fibres. See Appendix C for the visual basic program. For the positions that are disregarded due to insufficient coupling the program gives a value of (0,0) for positions (x_2, y_2) in the mapping file.

6.3 Image reconstruction

An image was recorded of the fibre bundle end. This image is read into a program written in Matlab®, see Appendix C. In Matlab the pixel values of the image create a matrix of intensity values. The program then creates a matrix of values the same size as the image matrix but filled with zeros. The map attained as described in the previous section is also fed into the program. This map consisted of the positions of the centre of the bright spot as measured in the pixels numbers of the image, these are named (x_2, y_2) and the positions of the objective when the image was captured, named (x_1, y_1) . The program takes an area of pixels around the position (x_2, y_2) and transfers them to the new matrix centred on a position (x_1, y_1) . The mapping file was the result of 10,000 images. The light spots that did not fall into the area or intensity criteria set for a well focussed spot of light were given positions of (0,0) and were disregarded in to program. The image taken by the camera of the fibre end and the resulting image from the program are shown in Figures 6.5. The image is reconstructed and appears as circular pattern, which was illuminated at the entrance face on the bundle.

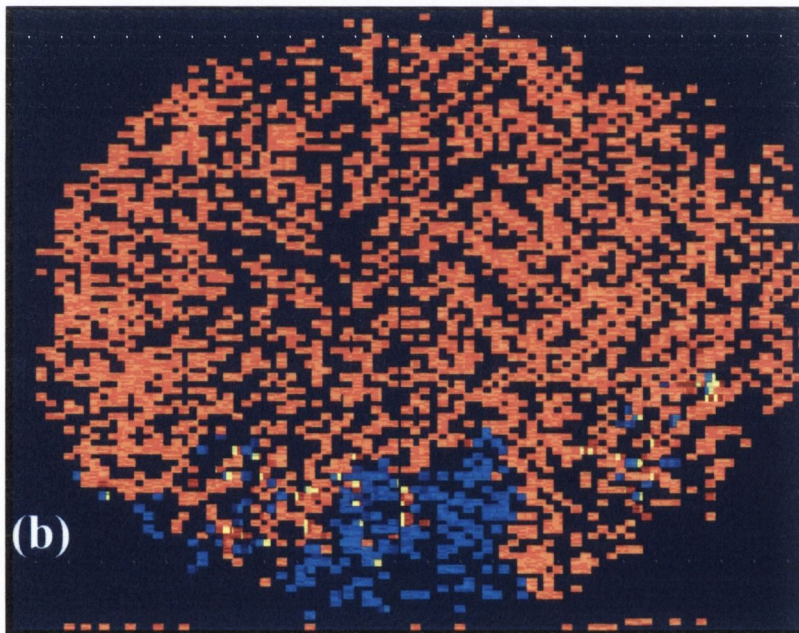
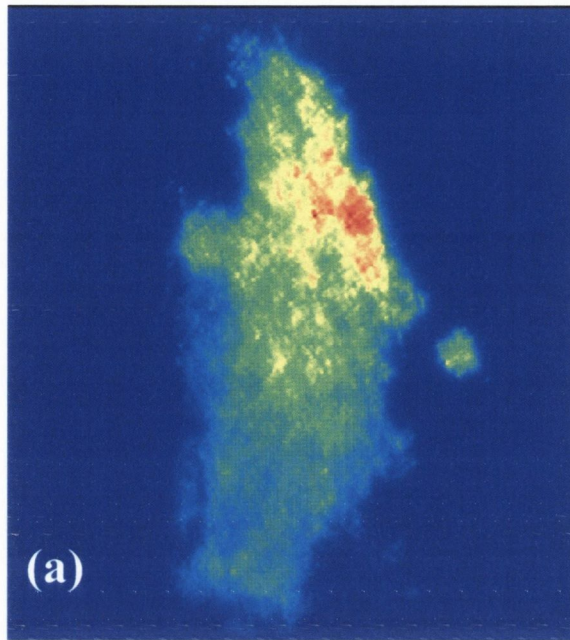


Figure 6.5 Image of the fibre bundle graphed in Matlab (a) and its reconstructed image (b). The colours are a designation of the intensity with blue being least and red the most intense.

6.4 Conclusions

The circular pattern of the fibre bundle end, Figure 6.5(b), is recreated from that of the somewhat flattened end, Figure 6.5(a), of which the image was taken. Initial efforts to pass an image through the fibre bundle were unsuccessful. This was mainly due to the fact that the fibre ends were not aligned flat at the face of the bundle. The fact that they were not aligned caused fibres to be missed completely. The light could not be coupled to these without splitting light into the neighbouring fibres unless the objective was moved in the optical axis, placing its focus in the plane of each individual fibre. This is not practical with the number of fibre involved. In order to account for the majority of the fibres which were not in the focal plane of the objective lens, the area and intensity criteria was therefore relaxed. This had drawbacks as there were positions noted that was not the position of best coupling.

As an example, image in Figure 6.5(b) was reconstructed for over 10,000 images. From the fibre diameter and the packing fraction ~5500 fibres were present in the 4mm diameter fibre end illuminated. In the mapping file there were ~13000 fibres mapping positions that were supposedly positions of best coupling; double that of the amount of fibres present. It follows from this that the light transferred to the reconstructed image matrix from the measured one would overlap at many of the positions. This would lead to degradation of the reconstructed image. A bundle with all the fibres aligned flat at the face would mean that strict criteria could be used to measure the point of highest coupling and only that position.

From the bottom of the reconstructed image in Figure 6.5(b) there are light spots which correspond to (0,0) positions of the stage. These are due to the movement of the line scan and

can be disregarded. Due to time constraints the time delay set between the image captures did not allow sufficient time for the line scan to have completed. This resulted in the scan crossing the centre of the fibre bundle when the camera took an image. It assumes this point is the beginning of the line scan and notes the position accordingly. There were also constraints on the virtual memory of the computer on which the images were stored which did not allow the automation of the entire process but limited it to sections, of which there were ~10.

I am confident that with the proper fibre bundle this method would prove successful in transmitting images. A computer with more available memory would allow the process to be completely automated, smaller step sizes could be taken and the entire scan done over night.

Chapter 7

F.L.I.M CONFOCAL MICROSCOPY ON MODIFIED FLOURESCENCE OF QUANTUM DOTS

7.1 Introduction and background

An excited electron in a molecule or atom has many possible routes to reorganise into the lower energy levels. By doing this it realises the energy it obtained when excited. It may do this by releasing the energy as a photon of longer wavelength than the excitation photon; this is named fluorescence, the molecule can then be named as a fluorophore. The fluorescence lifetime is an intrinsic property of the molecule and occurs on the scale of nanoseconds. Next to the spectral information from the fluorescence the lifetime is a powerful way to discriminate molecules of interest from the background⁷¹. The intensity decay of the fluorescence is given by¹²

$$I(t) = \sum_i A_i \exp\left(-t/\tau_i\right) \quad \text{Eqn. 7.1}$$

Here, $I(t)$, is the intensity detected from the fluorescence a time, t , after the excitation occurred. The values τ_i denote the decay times. The measurement of these lifetimes and their spatial displacement is the basis of fluorescence lifetime imaging microscopy (F.L.I.M). Fluorescence microscopy can be implemented in conventional and confocal microscopy, although it is advantageous to use confocal microscopy. In conventional microscopy the

fluorescence from a certain volume of the sample is collected at the detector. That is to say the light emitted from all fluorescent points in the sample. There may also be some emission and re-absorption from these points of the sample to others which can then add to the image at the detector. If a small amount of fluorophore to be imaged, with lifetime τ_1 , is surrounded by a volume of fluorophores with lifetime, τ_2 , and we image that volume only a small signal from the, τ_1 , will be present in a large background of, τ_2 , signal. By using a confocal microscope the volume from which the light is detected is much reduced leading to a higher relative fluorescence signal from the molecule with lifetime τ_1 ¹².

Lifetime imaging can be divided into two common techniques, phase fluorometry and the more popular time-correlated single photon counting (TCSPC) technique. Phase fluorometry excites the sample with an intensity modulated excitation beam and measures the phase delay arising from the fluorescence of the sample. Phase fluorometry is in the frequency domain, whereas TCSPC is in the time domain¹². TCSPC is based on the detection of single photons excited by a periodical light signal, generally a pulsed laser, the measurement of the detection times of the individual photons and the reconstruction of the waveform from the individual time measurements. The detector signal consists of a train of randomly distributed pulses due to the detection of the individual photons. Periods with more than one photon are very rare. When a photon is detected, the time of the corresponding detector pulse is measured. The events are collected in a memory by adding a '1' in a memory location with an address proportional to the detection time. After many photons, in the memory the histogram of the detection times as shown in Figure 7.1.

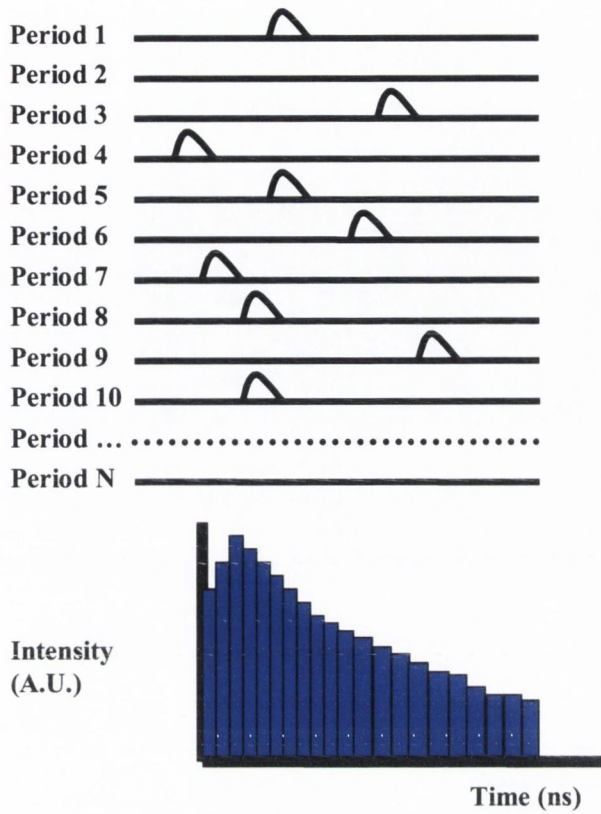


Figure 7.1 Showing the detection of photons which are given a time delay value and added to give the lifetime histogram as shown which is then fitted by an exponential decay curve.

The histogram is then fitted by an exponential decay curve given by equation 7.1. The pre-exponential factors in Equation 7.1 are taken into account by the fact that the curve is normalized to one at the point of highest intensity. The average lifetime is then calculated by the equation⁷²

$$\tau_{ave} = \frac{\sum_{i=N1}^{i=N2} A_i \tau_i^2}{\sum_{i=N1}^{i=N2} A_i \tau_i} \quad \text{Eqn. 7.2}$$

Here N_1 and N_2 are the values at the beginning of the decay, i.e. the point of highest intensity, and the end of the curve respectively. The curve given by the Equation 7.1 is fitted to the experimental data by the sum of least squares. The fit value, χ^2 , is given by the square of the difference of the experimental data to that of the calculated decay curve. O'Connor *et al.*⁷² give a criterion of $0.8 < \chi^2 < 1.2$ for an acceptable fit. The residuals are given as the difference between the experimental data and that of the decay curve fit for each point. When these are measured against time an even distribution of the residuals around the zero line also indicate a good fit. These are used to evaluate decay curves in the following study.

The technique described above is to be used to image the modified lifetime of the luminescence of CdTe quantum dots in the vicinity of surface plasmon supporting metallic nanostructures.

7.2 Experimental set-up

The F.L.I.M. microscope used was the Pico Quant Microtime 200 time-resolved confocal microscope system, equipped with Olympus IX71 microscope. The samples were excited by 480 nm picosecond pulses generated by a Pico Quant, LDH-480 laser head controlled by a PDL-800B driver. The setup was operated at an overall time resolution of ~ 150 ps. The apparatus is described in detail elsewhere⁷¹, the difference between that set-up and ours is that a single channel was used for detection. Scanning of the sample was made possible by stage

scanning with nm resolution using a P-733 X-Y Piezo-positioner together with an E-710 digital PZT controller (Physik Instrumente). The spatial resolution of the images was determined by the PZT controller sending a signal to the computer at the beginning of each frame and line scan which could then relate the position of the photon to the incoming information for the detector.

7.3 Sample Preparation

7.3.1 Gold nanoparticle preparation

Au spherical NPs were produced by a modified citrate reduction of HAuCl_4 stabilized by a water-soluble mercapto ligand (sodium 3-mercaptopropionate)⁷³. No rigorous cleanliness of glassware was needed during the fabrication and the reductant is decomposed to CO_2 . Stable aqueous dispersions of gold nanoparticles with only small amounts of precipitation over several months were obtained. The stabilising agent, sodium 3-mercaptopropionate (MPA-Na), was prepared by neutralization with NaOH 3-mercaptopropionic acid. The particle size was controlled by the stabilizer/gold ratios. The refluxing agents changed colour from yellow to brownish red, which is the colour for quantum confined gold. Particles were then washed by the addition of di-ethyl-ether and placed in a 14000rpm centrifuge and then washed with water. Confirmation of colloidal Au was obtained by UV-Vis absorbance spectra of the solution which had a sharp absorbance peak at 519nm, as shown in Figure 7.2 (a), which is indicative of spherical Au nanoparticles with an approximate diameter of 15nm⁷⁴.

Transmission electron microscopy (TEM) of the nanoparticles did show nanoparticles with an average diameter of 14.7nm but with a rather large standard deviation of 5nm. One such TEM image is shown in Figure 7.2 (b).

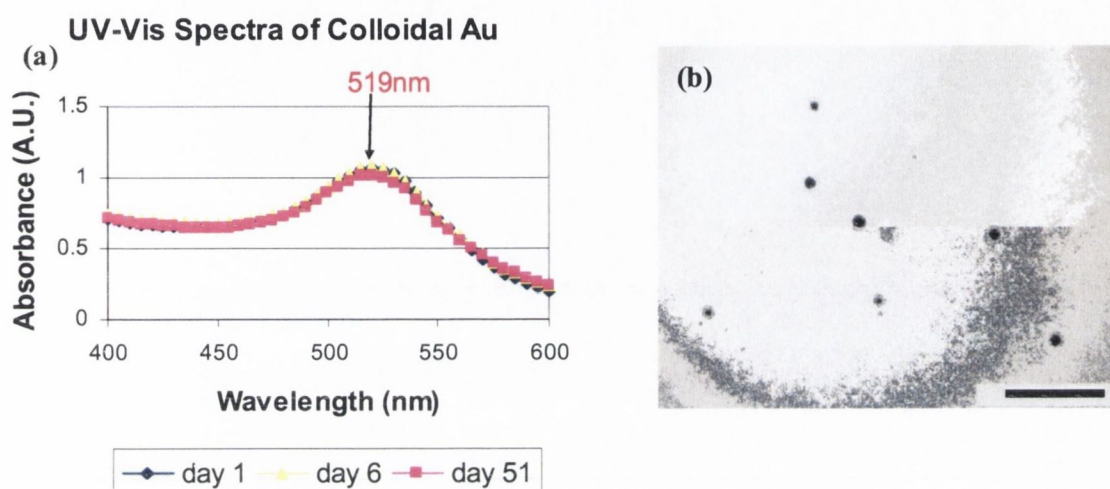


Figure 7.2 UV-Vis absorbance spectra of colloidal Au showing a sharp plasmon absorbance peak (a) the same Au particles when dropped and dried on a grid and imaged under the TEM (b) the scale bar observes a 200nm distance.

7.3.2 Sample preparation for F.L.I.M. imaging

A schematic diagram of the samples under investigation in the confocal microscope is shown in Figure 7.5. The relative sizes of the individual layers are greatly exaggerated for clarity. A PE layer is formed on the quartz slide by the LBL technique. In this case a glass slide is laced in an excess solution of PEI (polyethyleneimine) which forms a monolayer of the polymer on the glass slide.

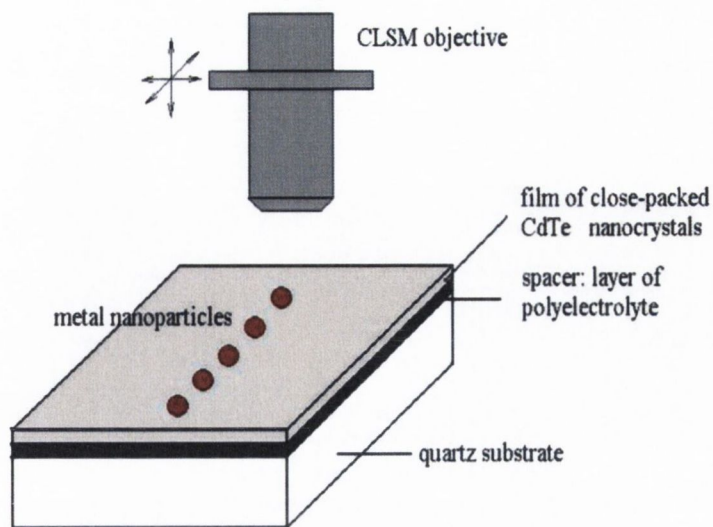


Figure 7.5 Schematic diagram of a prepared sample and its orientation under the confocal laser scanning microscope (CLSM) objective.

The polyanion used in this case was PSS and the polycation used to form the following layers is PDDA poly(diallyldimethylammonium chloride). This can be used to absorb a layer of CdTe QD onto the sample surface. The quantum dots used are Cd-Te nanocrystals capped with thioglycolic acid (TGA) which leaves a negative surface charge on the dots⁷⁷, the measured photoluminescence is displayed in Figure 7.6.

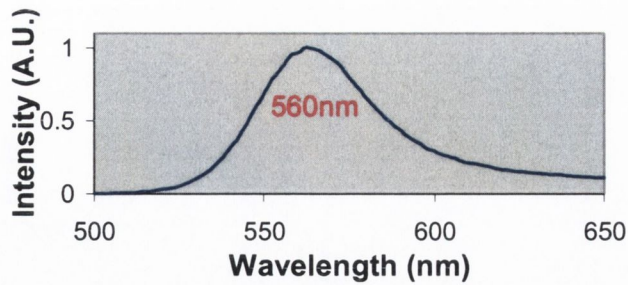


Figure 7.6 Photoluminescence spectra of CdTe QD in water.

By displacing the quantum dots from the quartz surface using the polymer layers there is no quenching due to surface effects. The other effect of the polymer layers is to increase or produce a surface charge on the sample which allows the placement of a monolayer of QD. A diluted drop of colloidal gold prepared as described in Section 7.3.1 is dropped on to the surface of this sample. As the surface dries much of the Au in the solution tends to the edge of the droplet, thus there is a large collection of the Au along the edge of the evaporated Au droplet.

7.4 Confocal F.L.I.M

Strong quenching of QD photoluminescence accompanied by reduction in PL decay time can be seen. Corresponding time-dependent PL intensity decays obtained from the F.L.I.M.

images are presented in Figure 7.7 demonstrating strong reduction in PL lifetime caused by Au nanoparticles.

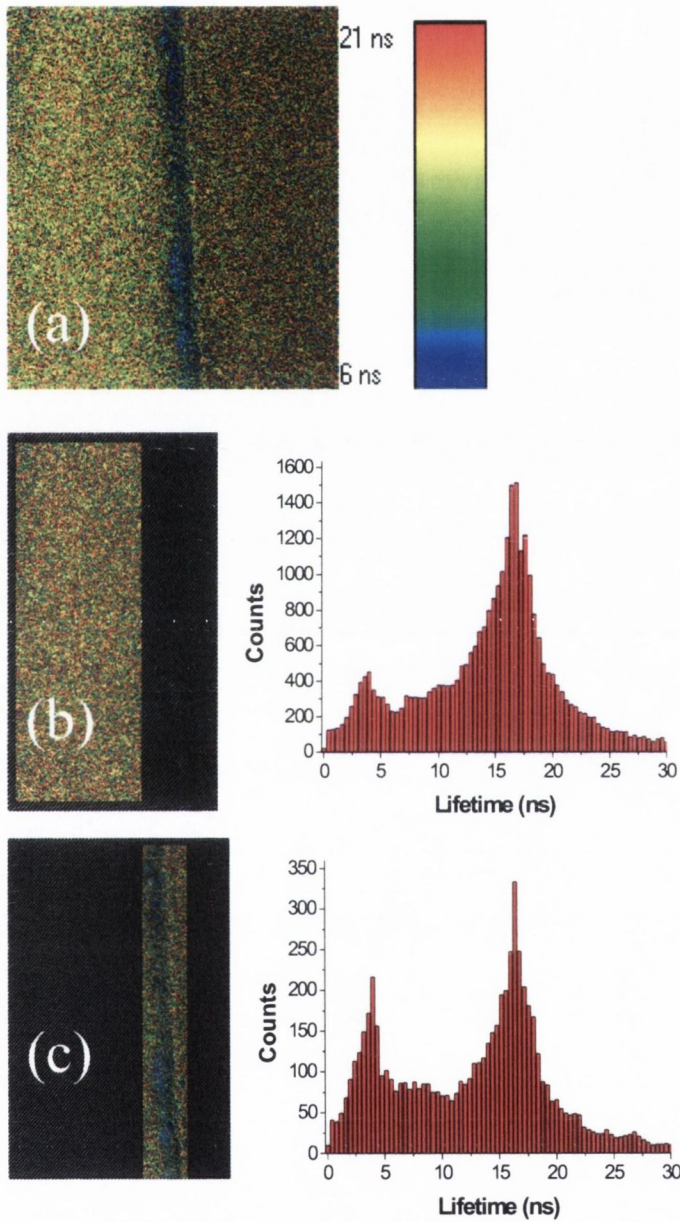


Figure 7.7 FLIM image of Au nanoparticles aligned on the surface of a monolayer of CdTe QD (a) and its unquenched (b) and quenched (c) parts. The corresponding histograms show the electron counts for the corresponding images

Using a conventional microscope we also imaged the collection of Au particles along the edge of a droplet of colloidal solution. The image, Figure 7.8, was recorded by a CCD camera attached to a Nicolet Continuum optical microscope and the contrast has been increased by the computer to show the NPs more clearly.

In all cases the PL decays curves are dominated by two emission components with corresponding lifetimes in the nanosecond time scale (Table 7.1), consistent with a PL model that includes multiple emission pathways⁷⁸. This multi-exponential behaviour is almost universal in the PL dynamics of colloidal II-VI QD. The multi-exponentials fit are shown in Figure 7.9 as calculated from the equations outline in Section 7.1. The even distributions of the residuals around zero show that the calculated fit is indeed accurate. Table 7.1 shows the values for the lifetimes, τ_i , and the pre-exponential factors, A_i . A decrease in the calculated average lifetime shows that there is a significant drop in the spontaneous emission rate of CdTe QD by interaction with Au nanoparticles. This is also clearly shown in the enhanced contribution from the shorter lifetimes, A_1 for that section of the QD layer is contact with the metallic NPs. The histograms in Figure 7.7 show a drastic decrease in the amount of long lifetime radiation. This has been suggested as being due to a reduction in the interplay of the surface states of the QDs⁷⁸.

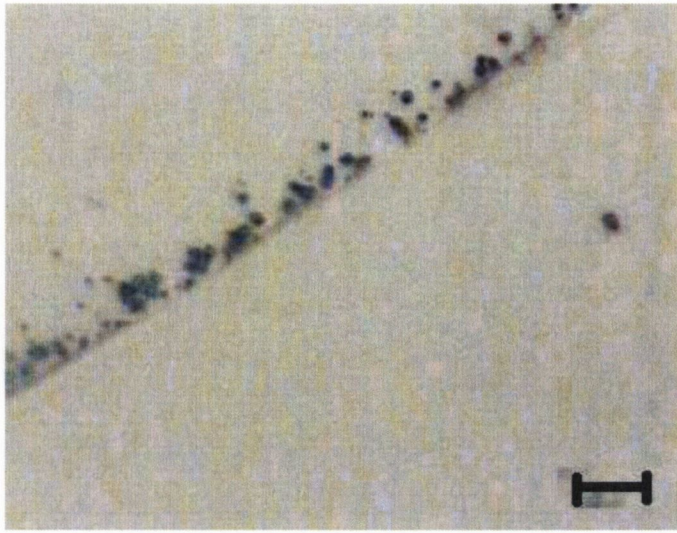


Figure 7.8 Brightfield microscope image of NPs coming together along the edge of the droplet. The size bar denotes a distance of $\sim 20\mu\text{m}$

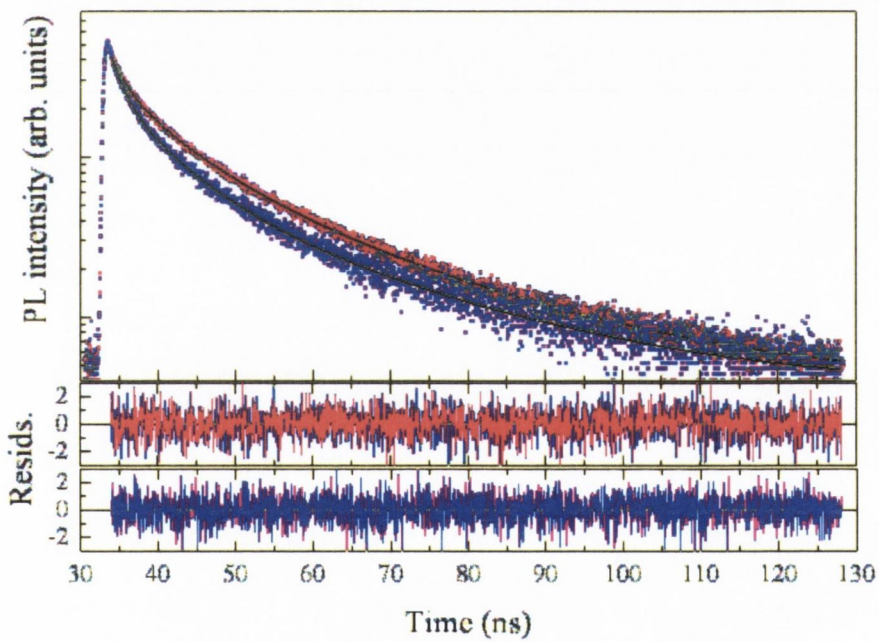


Figure 7.9 (a) Time-dependent PL intensity decays obtained from FLIM images presented in Figure 7.7 (a) (red dots) and (c) (blue dots). Results of three-exponential analysis of decay curves are shown by thick black lines with corresponding residuals.

Image	τ_1 (ns)	A ₁	τ_2 (ns)	A ₂	τ_3 (ns)	A ₃	τ_{ave} (ns)
Fig.7.6(b)	1.782	0.36	7.844	0.43	23.446	0.21	15.89
Fig.7.6(c)	1.600	0.46	6.451	0.41	21.997	0.13	13.12

Table 1: Three-exponential fit parameters to the observed PL decays presented in Figure 7.7 (b) and (c).

7.6 Discussion and Future work

The interaction between metals and fluorophores has been widely researched, some references are given for the many that could be chosen^{79, 80, 81} and has been found to have a great impact of the fluorescence emitted from both QD and dyes. The technique studied here has shown that this interaction can result in high contrast confocal F.L.I.M. imaging.

The drop in fluorescence is due to the increase in non-radiative pathways for the electron in the QD to return to the lower energy states⁸⁰. The dominant mechanisms are the non-radiative energy transfer from the QD to the Au nanoparticles. Much interest has been shown in the interaction of light with nano-structured Au particles. This is because of the unusual interaction of photons with the metals. Incident photons from the light can be made to excite collective oscillations of the conduction band electrons of the metal. These are commonly known as surface plasmons (SP) but more strictly speaking they should be called plasmon-

polaritons, as a plasmon is the quantized charge density wave and a polariton is the coupling of a light wave to this plasmon. In 1998 a group in Spain while studying the dielectric response of metals to make photonic materials found that the transmission of light through subwavelength hole arrays made in a metal film can be orders of magnitude larger than expected from classical diffraction theory⁸², it seemed that light impinging on the metal between the holes was transmitted. This was attributed to the creation of surface plasmons on one surface, migration of the plasmons through the holes, and subsequent radiation of the plasmons from the distal side of that metal. This has led to an vast amount of study in the field, some of the results are high lighted different reviews⁸³⁻⁸⁵. From this research an entire field of study has originated which has been termed Plasmonics, which is denoted as a merging of the fields of electronics and photonics. The coupling of light to these SP and their channelling along nanostructures shows great promise. They can take account of the large bandwidth of photonics and the small scaling of electrical circuits. The techniques for imaging these structures are typically expensive and time consuming with techniques like SEM and AFM at the forefront. The technique studied in this work shows potential for the imaging of these structures in a quick and relatively cheap fashion although there are obvious drawbacks in the resolution obtainable. The integration of this technique with STED microscopy⁸⁶ may open a path to a far-field high-resolution optical imaging technique. The SP can be tuned to a very high degree with the shape and size playing an important factor⁸⁷. None have been more useful in the tuning of the SP absorbance band than nanoshells structures like those presented in Section 7.3.2⁸⁸. The absorbance band of these nano- and micro-shells can be tuned across the visible and infrared regions of the electromagnetic spectrum. These structures could be very efficient in targeted drug delivery systems⁸⁸. The fluorescent properties of the systems are

key to any developments in this field and the studied process could be very useful in understanding the interactions at play.

The F.L.I.M. images in Section 7.4 show the decrease in fluorescence of the QD in contact with Au nanoparticles. The interaction between metal nanoparticles and fluorescent particles is known to be highly distance dependant^{80, 89} and is the subject of much study. With the coating of polymer spheres with Au particles and the sample preparation as shown this distance dependence can be further probed by utilising the curvature of the spheres to investigate this distance dependence.

Chapter 8

Conclusions

The versatility of the confocal technique has been studied in this thesis from different aspects. The main goal of the research has been inclusion of variable focal length microlenses into the confocal system and the examination of their possible advantages. These lenses were first characterised before the examination of possible confocal systems. The mapping of an incoherent fiber bundle was then undertaken for its use as an image conduit. Chapter 5 and 7 deals with the study of fluorescent confocal microscopy. The size determination of dye-doped melamine formaldehyde microspheres by spectral analysis was performed and the use of confocal FLIM microscopy in the exciting field of plasmonics was initiated. The outline of the use of confocal microscopy and its comparison to other high resolution imaging techniques was presented as a means of introducing this work along with a short presentation on the well accepted theory of confocal imaging in Chapter 2.

Liquid crystal variable focal length microlenses were designed, fabricated and tested for inclusion into the confocal system. The most thorough investigation, to the best of the author's knowledge, of the optical properties of liquid crystal lenses to date was undertaken. A novel technique for the imaging of emerging light fields of LC microlenses was presented. The results of which were compared to the examination of the quality of the lenses as measured by an interferometric microscope and described by the Strehl ratio. There is strong agreement between the visual evidence of aberrations and those calculated from the interferograms. It was also shown to be a simple procedure that is time efficient for qualitative analysis of the

optical properties of the lens at different voltages. A quick look at the focal spots (see Figure 3.15) is almost sufficient to see if a good lens has been formed. It was shown here that the lenses have only a certain voltage range (and focal length range) over which they have adequate optical quality. However it was shown that by even rough adjustment of the frequency with which the applied voltage is driven, the optical quality of these lenses can be significantly improved by up to 30%. This could pave the way for higher quality liquid crystal lenses. It was shown that the main aberration present was astigmatism and a study on the causes and correction of this aberration could further increase the optical quality of the lenses for wider application.

The inclusion of these lenses into a confocal set-up was then investigated. As most of the light incident on the array was focussed to an array of focal spots, a confocal system utilising the lenses as a high throughput aperture array was assembled. A fiber bundle was employed as an aperture array. The lenses were shown to be well addressed to the fibre bundle. By varying the applied voltage across the LC lenses the focal spots were made to scan the mirror showing that light from defocused planes was indeed blocked by the fibres. The axial response for this scan is not a true measure of the optical sectioning as was discussed in Section 4.3. To utilise the focal scanning capabilities of the lenses another set of lenses with the same focal length variation would need to be applied to the end of the fibre. Another, possibly more useful approach, would be to use the fibres as the light source array as well as the pinhole array by mounting the VFL on the end of the fibre acting as an array of objective lenses. In the following section the VFL lenses were shown to act as an array of objective lenses and their optical sectioning properties investigated. Focal scanning was introduced and investigated. It

was shown that the depth response of the microlenses varied with the focal length of the system, therefore a practical instrument using these lenses would need a strict calibration of the intensities found from all the out-of-focus planes so that the results may be weighted accordingly. Due to the small working distance of the lenses, this form of microscopy may be most useful in topography studies.

Confocal fluorescence microscopy images of dye-doped melamine formaldehyde microspheres coated with CdTe nanocrystals were taken. Using this technique it was possible to see defects on the sphere's surfaces as they acted as highly scattering points. Due to the depth discrimination property of the set-up the emission from the scattering points was discernable from that of other points on the spheres. Melamine formaldehyde microspheres were investigated under conventional scanning microscopy and their emission properties analyzed. By fitting the experimentally measured mode spacing and fitting them to theoretical equations, the size of the sphere was determined. The sizes determined using this purely optical method seemed reliable, as they fell within the size specifications given by the company using their testing methods. From the spectra, the Q factors for the spheres were also determined.

In Chapter 6 the mapping of an incoherent fibre bundle was achieved. The main issues relating to this task were discussed. It has been shown as a proof of principle, the mapping of the individual fibres in a bundle can be done and the positions of the light from each the elements of the bundle rearranged to give the image incident on the opposite end of the bundle. The vast difference in cost between incoherent fibre bundles and imaging bundles could be drastically

decreased using this method. As the majority of incoherent fibre bundles commercially available were used as light guides the end connections were specifically designed accordingly. I am confident that with an incoherent fibre bundle, with the fibres polished and set across an even surface, this technique could allow high quality imaging with cheaper, more flexible fibre bundles.

Finally the initial steps were taken into a promising study of high contrast FLIM imaging of surface plasmon supporting structures. By novel sample preparation the large amount of fluorescence quenching from quantum dots due to the presence of Au nanoparticles leads to the spatial resolution of a collection of metal nanoparticles on a bed of quantum dots. Thus began a study on the possibility of measuring novel polymer metal hybrid nanostructures for both practical applications and towards a better understanding of the physical processes involved, some of these were discussed as future work in Section 7.6.

A study on VFL LC microlenses was performed, the issues noted, some improved and with further understanding of the distribution of the forces inside the cells there is the possibility to fabricate high quality lenses with a large focal length range. Their inclusion into the confocal system was investigated, which may show promise in certain applications. Microspheres were investigated under confocal and conventional microscopy. A fitting method was used to find the size of microspheres and qualify the theoretical models. The mapping of an incoherent fibre bundle was performed which could decrease the cost of confocal endoscopes. Finally a study into the use of confocal F.L.I.M. imaging of metal-polymer-QD hybrid structures was

undertaken and shows great promise for the future. I believe that these studies together outline a broad study into the versatility of the confocal technique and its instrumentation.

Appendix A

Liquid crystal immersed microlenses supplied by Dr. Selviah's optical system device research group in UCL³⁴ were investigated originally and their focal length voltage relationship measured. The microlenses are manufactured by the melt and reflow of photoresist method. These microlenses are then immersed in liquid crystal (LC) to produce a VFL cell.

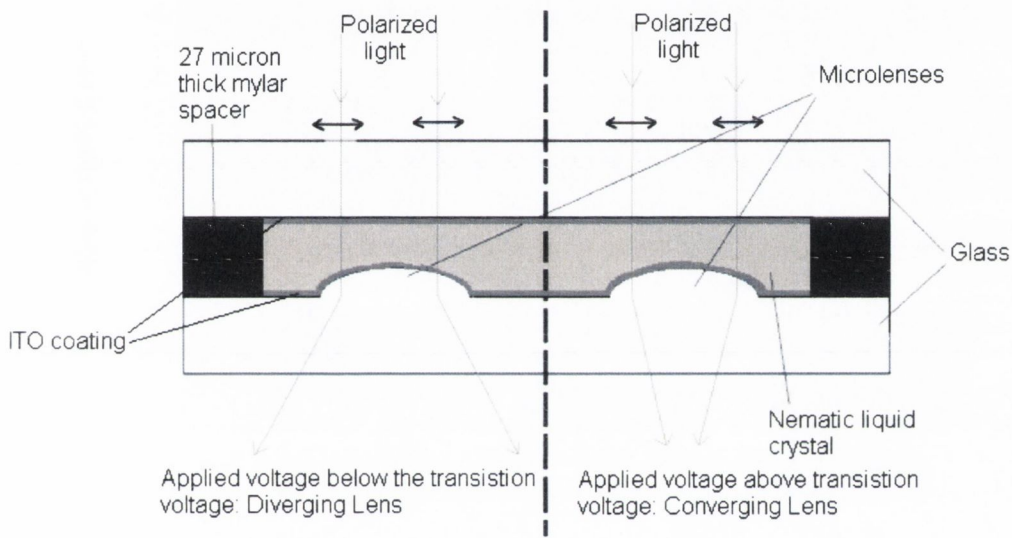


Figure A1. Schematic diagram showing a cross section of a variable focal length microlens cell.

Immersion in liquid crystal allows for the VFL property of the cells by altering the refractive index of the immersion media, i.e. the LC. By aligning the direction of linear polarised light parallel to the extraordinary axis of the birefringent LC. The variation in the LC can be taken simply as a change in the refractive index of the media. Thus the focal length of the cell is controlled by the refractive indices of the microlenses and the LC.

$$f = [(n_{\text{liquid crystal}} - n_{\text{photoresist}}) c]^{-1}$$

Experiments on the variation of focal length with voltage show that these cells may act as diverging or converging lenses, switching between the two when the effective refractive index of the LC is equal to that of the microlenses.

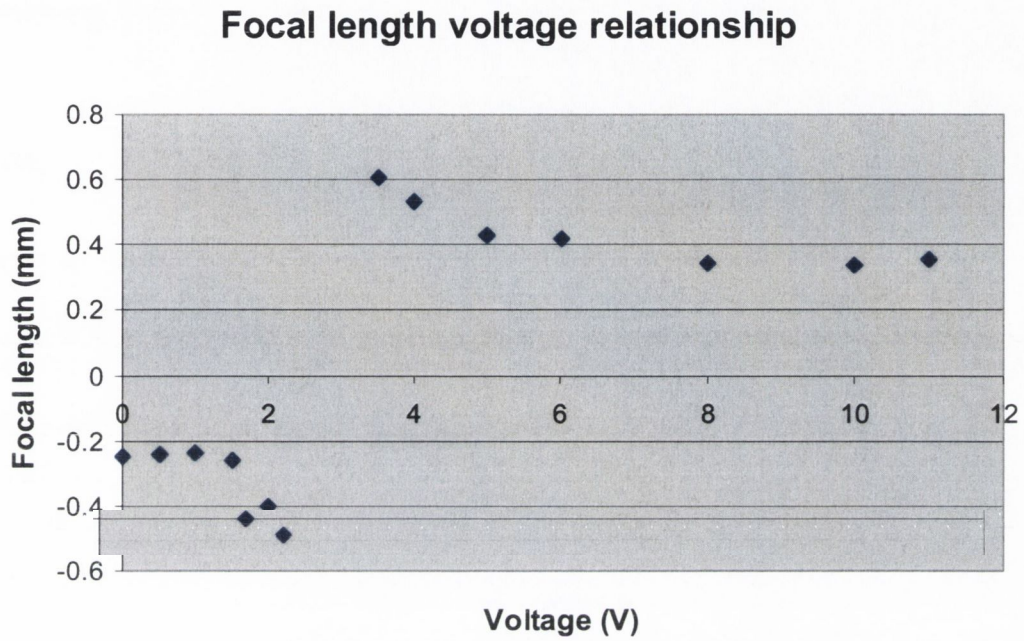


Figure A2. Focal length variation with applied voltage for microlenses of $55\mu\text{m}$ immersed in liquid crystal

Appendix B

The following is a Matlab program written for the determination of the radius of the microspheres by fitting the spectral data to the theoretical values for the mode spacing.

```
m=1.68;           %this is equation 5.1 and equation 5.1, done for TE modes

l=[543 556  570  585  601  618  635  654  675  697  720  746];
    %peak position, experimental results
lambda=l(1:12);
a=2400:2:2600;    %radius sizes
sd=length(a);
for s=1:sd;
r(s)=a(s);        %r(s)= vector of radius sizes
end
for i=1:12 ;
for s=1:sd;
    x(i,s)=(2*pi*r(s))/lambda(i); %size parameters for different values of wavelength
    (rows) and different values of radius(columns)
n(i,s)=27-i;      %mode orders, same in each column
end
end
norm=length(n(1:11))

for i=1:11 ;
for s=1:sd;
    deltax2(i,s)=(x(i,s)*(atan((((m*x(i,s))/n(i,s)).^2)-
    1)).^0.5))/(n(i,s)*((((m*x(i,s))/n(i,s)).^2)-1).^0.5));
```

```

                                %delta x from equation 5.2
d_lam_exp(i,s)=lambda(i+1)-lambda(i); %experimental mode spacing

                                deltalamba21(i,s)=((lambda(i)*lambda(i+1)*deltax2(i,s))./(2*pi*r(s)));
                                deltax1=(atan(sqrt(m^2-1)))/(sqrt(m^2-1));
                                deltalambda1(i,s)=((lambda(i)*lambda(i+1)*deltax1)./(2*pi*r(s)));
end
end

for i=1:12 ;
    for s=1:sd;
t(i,s)=sqrt((x(i,s)-n(i,s)).^2);
p(i,s)=(t(i,s)>=4);
end
end

diff_squared12=zeros(11,sd);
diff_squared2=zeros(11,sd);
for i=2:12 ;
    for s=1:sd;
        if p(i,s)==0;
            diff_squared12(i,s)=(d_lam_exp(i-1,s)-deltalambda1(i-1,s)).^2; %difference d1
        elseif p(i,s)==1;
            diff_squared2(i,s)=(d_lam_exp(i-1,s)-deltalamba21(i-1,s)).^2; %difference d2
        end
    end
end

value1=sum(diff_squared12,1);
value2=sum(diff_squared2,1);
fit=value1+value2;

```

```
figure;plot(r(1:sd),fit(1:sd),'o');  
hold on;  
xlabel('Sphere Radius (nm)')  
ylabel ('Fit Value')
```

```
[q,b]=min(fit);  
calculated_radius=r(b)  
value=fit(b)
```

```
figure;plot(n(2:12),d_lam_exp,'sk',n(2:12),deltalambda1,'ob',n(2:12),deltalambda21,'^r');  
ylabel('Mode Spacing (nm)')  
xlabel('Mode number')  
legend('Exp','Eqn 5.1','Eqn 5.2')
```

Appendix C

This appendix contains the programs written for the experiments outlines in Chapter 6. The programs which allowed the automation of the mapping process and the Matlab® program written for the image reconstruction.

Section A1

Visual basic® program written for the flexure stage controller which make a move in the raster scan when a trigger pulse from the camera was received. We originally received the program from Thorlabs® for the raster scan and this was modified to use a trigger pulse.

Option Explicit

Private Sub Form_Load()

' Set up of Motor.

On Error GoTo BasicErrorHandler

Dim lRetVal As Long

' Set serial number - either here in code OR use properties of control on form

' (use number of actual HW unit or simulated unit (see APTConfig for details))

MG17Motor1.HWSerialNum = 20808095

' Start motor control.

lRetVal = MG17Motor1.StartCtrl

If lRetVal <> MG17_OK Then Err.Raise lRetVal

Exit Sub

BasicErrorHandler:

MsgBox " An error has occurred", vbCritical, App.Title

Unload Me

End Sub

Private Sub cmdScan_Click()

' Call scan routine.

MotorScan2D

End Sub

Private Sub MotorScan2D()

' 2 Dimensional motor raster scan.

On Error GoTo BasicErrorHandler

Dim lRetVal As Long

Dim sngStartPoint(CHAN1_ID To CHAN2_ID) As Single

Dim lngNumSteps(CHAN1_ID To CHAN2_ID) As Long

Dim sngInterval(CHAN1_ID To CHAN2_ID) As Single

Dim i%, j%

Dim sngChan1Positions() As Single

Dim sngChan2Positions() As Single

Dim ret%

' Home motors.

lRetVal = MG17Motor1.MoveHome(CHANBOTH_ID, False)

```

If lRetVal <> MG17_OK Then Err.Raise lRetVal

' Set start point of scan as 0,0.
sngStartPoint(CHAN1_ID) = 0
sngStartPoint(CHAN2_ID) = 0

' Set number of steps along each axis as 10.
lngNumSteps(CHAN1_ID) = 3
lngNumSteps(CHAN2_ID) = 3

' Redimension channel 1 and channel 2 position arrays according to number of steps.
ReDim Preserve sngChan1Positions(0 To lngNumSteps(CHAN1_ID))
ReDim sngChan2Positions(0 To lngNumSteps(CHAN2_ID))

' Set step interval for each axis.
sngInterval(CHAN1_ID) = 0.04
sngInterval(CHAN2_ID) = 0.04
' Nested loops to step through all positions (in raster pattern).
For i = 0 To lngNumSteps(CHAN1_ID)
    For j = 0 To lngNumSteps(CHAN2_ID)

        ' Calculate position for each channel separately.
        ' Position = start point + (loop index * interval)
        sngChan1Positions(i) = sngStartPoint(CHAN1_ID) + i * sngInterval(CHAN1_ID)
        sngChan2Positions(j) = sngStartPoint(CHAN2_ID) + j * sngInterval(CHAN2_ID)

        ' Method sets the absolute position to which the channel
        ' specified will move, the next time the MoveAbsolute
        ' method is called.
        lRetVal = MG17Motor1.SetAbsMovePos(CHAN1_ID, sngChan1Positions(i))
        If lRetVal <> MG17_OK Then Err.Raise lRetVal
    
```

```

lRetVal = MG17Motor1.SetAbsMovePos(CHAN2_ID, sngChan2Positions(j))
If lRetVal <> MG17_OK Then Err.Raise lRetVal
Ch1Moved = False
ret% = MG17Motor1.SetTriggerParams(0, TRIGMODE_IN, TRIGMOVE_ABS)
While Ch1Moved = False
    DoEvents
Wend
' Method initiates a motor move on the channel specified,
' as set above.
lRetVal = MG17Motor1.MoveAbsolute(CHAN2_ID, True)
If lRetVal <> MG17_OK Then Err.Raise lRetVal

```

```
Next j
```

```
Next i
```

```
Exit Sub
```

```
BasicErrorHandler:
```

```
MsgBox " An error has occurred", vbCritical, App.Title
```

```
End Sub
```

```
Private Sub cmdExit_Click()
```

```
' Unload form.
```

```
Unload Me
```

```
End Sub
```

```
Private Sub MG17Motor1_MoveComplete(ByVal IHWChannel As Long)
```

```
DoEvents
```

```
Select Case IHWChannel
```

```

Case 0 ' move absolute
    Ch1Moved = True
Case 1
    Ch2Moved = True
End Select
End Sub

Private Sub Form_Unload(Cancel As Integer)
' Stop Motor control.

    MG17Motor1.StopCtrl

End Sub

```

Section A2

A program had then to be written in Image Pro-Plus to count the number of bright spots, measure their area, intensity and their centre positions in x and y. The images which were not defined as well coupled by the criterion set were then disregarded. A data file is opened and the area and centre positions are placed in the file with a value of (0,0) for the images which were disregarded by the measuring criteria.

```

Sub Joe()
    Dim Count As Integer
    Dim numFrames As Integer
    Dim I As Integer
    Dim FileName As String
    FileName="D:\D\fiber imaging\06-10-22\dataY.cnt"
    IpSeqPlay (SEQ_FFRA)
    ret=IpSeqGet(SEQ_NUMFRAMES, numFrames)

```



```

ret = IpBlbShow(1)
'Opens the count size window
ret = IpSegSetRange(0, 47, 255)
ret = IpSegPreview(CURRENT_C_T)
'shows the counted area up as red spot
ret = IpSegSetRange(0, 47, 255)
ret = IpSegPreview(CURRENT_C_T)
'shows the counted area up as red spot
ret = IpBlbSetRange(47, 255) 'sets

```

intensities range of objects to be counted

```

ret = IpSegShow(0)
'This function is used to close the Segmentation command window
ret = IpBlbEnableMeas(BLBM_CENTRX, 1)
'Enables measurement of the of the centre of object in x dir
ret = IpBlbEnableMeas(BLBM_CENTRY, 1)
'Enables measurement of the of the centre of object in x dir
ret = IpBlbSetFilterRange(BLBM_AREA, 18, 10000800.0)'Filter range for area
ret = IpBlbCount()

```

'Performs count, This function returns a long value representing the number of counted objects within range, or 0 if no objects were found.

```

ret = IpBlbUpdate(0)
'makes the active windows in image pro update to show it following the macro
ret = IpBlbUpdate(0)

```

If Count>0 Then

```

    ret = IpBlbSaveData(FileName, S_DATA)

```

Else

```

    Open FileName For Output As #1

```

```

    Print #1, "0" & Chr$(9) & "0" & Chr$(9) & "0" & Chr$(9)

```

```

    Close #1

```

End If

```

For I=1 To numFrames Step 1

```

```

ret = IpSeqPlay(SEQ_NEXT)
Count = IpBlbCount()
ret = IpBlbUpdate(0)
If Count>0 Then
    ret = IpBlbSaveData(FileName, S_DATA+S_APPEND)
Else
    Open FileName For Append As #1
    Print #1,"0" & Chr$(9) & "0" & Chr$(9) & "0" & Chr$(9)
    Close #1
End If
Next I
End Sub

```

Section A3

The Matlab program for image reconstruction is shown below.

```

% Load image file
M1=load('fiber_end.txt');

% Find minimum value of image matrix (background intensity)
[a,b]=min(M1);
m=min(a);

d=4 %width of pixels taken as square of light from the image

% Delete background intensity
M=M1-m;

% Create new matrix image

```

```

N=zeros(1:450,1:450);

% Read in the map file
map=load('fibermap_final.txt');

% Move from old image matrix to new image matrix
s=size(map)
p=s(1) %this gives the amount of images in the scan

for i=1:p
    x1=map(i,1)+d; %next four lines give x and y positions for each image matrix
    y1=map(i,2)+d;
    x2=map(i,3)+1;
    y2=map(i,4)+1;
    if x1>4
        r1=x1-(d/2);
        r2=x1+(d/2);
        s1=y1-(d/2);
        s2=y1+(d/2);
        N(x2:x2+d,y2:y2+d)=M(r1:r2,s1:s2);
    end
end

figure;pcolor(M1),SHADING FLAT
figure;pcolor(N),SHADING FLAT% Graph new image

%this section is to find the number of positions which were defined as well
%coupled
n=0

```

```
K=size(N)
p=K(1)
o=K(2)

for i=1:p
    for j=1:o
        if N(i,j)~=0
            n=n+1;
        end
    end
end

u=n/4
```

References

1. E. Hecht, "Optics," **3rd Edition**.
2. J. A. Okeefe, "Resolving Power of Visible Light," *Journal of the Optical Society of America* **46**, 359-359 (1956).
3. R. Kopelman, and W. H. Tan, "Near-Field Optics - Imaging Single Molecules," *Science* **262**, 1382-1384 (1993).
4. H. D. Young, and R. A. Freedman, *University physics* (Addison-Wesley, Reading, Mass. ; Wokingham, 1996).
5. C. V.E., "Modern Microscopy," (1966).
6. S. W. Hell, "Increasing the REsolution of Far-Field Fluorescence Light Microscopy by Point-Spread-Function Engineering," *Topics In Fluorescence Spectroscopy* **5**, (1997).
7. T. Wilson, and C. Sheppard, "Theory and Practice of Scanning Optical Microscopy," Academic Press, (1984).
8. M. Minsky, "Memoir on Inventing the Confocal Scanning Microscope," *Scanning* **10**, 128-138 (1988).
9. D. Huang, E. A. Swanson, C. P. Lin, J. S. Schuman, W. G. Stinson, W. Chang, M. R. Hee, T. Flotte, K. Gregory, C. A. Puliafito, and a. et, "Optical coherence tomography," *Science* **254**, 1178-1181 (1991).
10. A. G. Podoleanu, G. M. Dobre, R. G. Cucu, R. Rosen, P. Garcia, J. Nieto, D. Will, R. Gentile, T. Muldoon, J. Walsh, L. A. Yannuzzi, Y. Fisher, D. Orlock, R. Weitz, J. A. Rogers, S. Dunne, and A. Boxer, "Combined multiplanar optical coherence tomography and confocal scanning ophthalmoscopy," *Journal of Biomedical Optics* **9**, 86-93 (2004).
11. W. Denk, J. H. Strickler, and W. W. Webb, "Two-photon laser scanning fluorescence microscopy," *Science* **248**, 73-76 (1990).
12. J. B. Pawley, *Handbook of biological confocal microscopy* (Plenum Press, New York ; London, 1995).
13. M. Born, and E. Wolf, "Principles of Optics," **6th edition**, (1980).
14. M. Gu, "Principles of Three-Dimensional Imaging in Confocal Microscopes," World Scientific Pub Co Inc, (1996).
15. C. J. R. Sheppard, and T. Wilson, "Depth of Field in Scanning Microscope," *Optics Letters* **3**, 115-117 (1978).
16. M. Honma, T. Nose, and S. Sato, "Optical properties of anamorphic liquid crystal microlenses and their application for laser diode collimation," *Japanese Journal of Applied Physics Part 1- Regular Papers Short Notes & Review Papers* **38**, 89-94 (1999).
17. D. Berreman, "Variable focus liquid crystal lens system, US Patent No. 4,190,330," (1980).
18. B. M. Wright, "Improvements in or relating to variable focus lenses," English patent, (1968).
19. G. C. Knollman, J. L. S. Bellin, and J. L. Weaver, "Variable-Focus Liquid-Filled Hydroacoustic Lens," *Journal of the Acoustical Society of America* **49**, 253-& (1971).
20. K. H. Jeong, G. L. Liu, N. Chronis, and L. P. Lee, "Tunable microdoublet lens array," *Optics Express* **12**, 2494-2500 (2004).
21. H. Oku, K. Hashimoto, and M. Ishikawa, "Variable-focus lens with 1-kHz bandwidth," *Optics Express* **12**, 2138-2149 (2004).
22. Y. Nishimoto, "Variable-focal-length lens using an electrooptic effect," U.S. Patent 4,466,703 1984, (1984).
23. M. B. Chang, "Total Internal-Reflection Lens," *Applied Optics* **24**, 1256-1259 (1985).

24. T. Tatebayashi, T. Yamamoto, and H. Sato, "Electrooptic Variable Focal-Length Lens Using PLZT Ceramic," *Applied Optics* **30**, 5049-5055 (1991).
25. T. Tatebayashi, T. Yamamoto, and H. Sato, "Dual Focal Point Electrooptic Lens with a Fresnel-Zone Plate on a Plzt Ceramic," *Applied Optics* **31**, 2770-2775 (1992).
26. T. Shibaguchi, and H. Funato, "Lead-Lanthanum Zirconate-Titanate (Plzt) Electrooptic Variable Focal-Length Lens with Stripe Electrodes," *Japanese Journal of Applied Physics Part 1-Regular Papers Short Notes & Review Papers* **31**, 3196-3200 (1992).
27. Q. W. Song, X. M. Wang, and R. Bussjager, "Lanthanum-modified lead zirconate titanate ceramic wafer-based electro-optic dynamic diverging lens," *Optics Letters* **21**, 242-244 (1996).
28. C. B. Gorman, H. A. Biebuyck, and G. M. Whitesides, "Control of the Shape of Liquid Lenses on a Modified Gold Surface Using an Applied Electrical Potential across a Self-Assembled Monolayer," *Langmuir* **11**, 2242-2246 (1995).
29. B. Berge, and J. Peseux, "Variable focal lens controlled by an external voltage: An application of electrowetting," *European Physical Journal E* **3**, 159-163 (2000).
30. T. Krupenkin, S. Yang, and P. Mach, "Tunable liquid microlens," *Applied Physics Letters* **82**, 316-318 (2003).
31. S. Sato, "Liquid-Crystal Lens-Cells with Variable Focal Length," *Japanese Journal of Applied Physics* **18**, 1679-1684 (1979).
32. S. T. Kowel, D. S. Cleverly, and P. G. Kornreich, "Focusing by Electrical Modulation of Refraction in a Liquid-Crystal Cell," *Applied Optics* **23**, 278-289 (1984).
33. M. Honma, T. Nose, and S. Sato, "Enhancement of numerical aperture of liquid crystal microlenses using a stacked electrode structure," *Japanese Journal of Applied Physics Part 1-Regular Papers Short Notes & Review Papers* **39**, 4799-4802 (2000).
34. L. G. Commander, S. E. Day, and D. R. Selviah, "Variable focal length microlenses," *Optics Communications* **177**, 157-170 (2000).
35. S. Masuda, S. Fujioka, M. Honma, T. Nose, and S. Sato, "Dependence of optical properties on the device and material parameters in liquid crystal microlenses," *Japanese Journal of Applied Physics Part 1-Regular Papers Short Notes & Review Papers* **35**, 4668-4672 (1996).
36. J. Lamprecht, ["http://www.optik.uni-erlangen.de/odem/research/work/index.php?lang=e&what=mz."](http://www.optik.uni-erlangen.de/odem/research/work/index.php?lang=e&what=mz.)
37. K. C. James C. Wyant, "Basic Wavefront Aberration Theory for Optical Metrology," *APPLIED OPTICS AND OPTICAL ENGINEERING* **11**, 28-39 (1992).
38. G. Yoon, "Aberration Theory," http://cfao.ucolick.org/pubs/presentations/eyedesign/05_aberrations_GY.pdf.
39. P. J. Collings, "Introduction to liquid crystals : chemistry and physics," Taylor & Francis, (1997).
40. J. Y. Wang, and D. E. Silva, "Wave-Front Interpretation with Zernike Polynomials," *Applied Optics* **19**, 1510-1518 (1980).
41. T. Scharf, K. Cottier, and R. Dandliker, "High quality adaptive liquid crystal microlenses," *Molecular Crystals and Liquid Crystals* **366**, 2265-2272 (2001).
42. P. J. Smith, C. M. Taylor, E. M. McCabe, D. R. Selviah, S. E. Day, and L. G. Commander, "Switchable fiber coupling using variable-focal-length microlenses," *Review of Scientific Instruments* **72**, 3132-3134 (2001).
43. D. T. Fewer, S. J. Hewlett, E. M. McCabe, and J. Hegarty, "Direct-view microscopy: Experimental investigation of the dependence of the optical sectioning characteristics on pinhole-array configuration," *Journal of Microscopy-Oxford* **187**, 54-61 (1997).
44. T. Tanaami, S. Otsuki, N. Tomosada, Y. Kosugi, M. Shimizu, and H. Ishida, "High-speed 1-frame/ms scanning confocal microscope with a microlens and Nipkow disks," *Applied Optics* **41**, 4704-4708 (2002).

45. K. B. Sung, R. Richards-Kortum, M. Follen, A. Malpica, C. Liang, and M. R. Descour, "Fiber optic confocal reflectance microscopy: a new real-time technique to view nuclear morphology in cervical squamous epithelium in vivo," *Optics Express* **11**, 3171-3181 (2003).
46. C. Liang, K. B. Sung, R. R. Richards-Kortum, and M. R. Descour, "Design of a high-numerical-aperture miniature microscope objective for an endoscopic fiber confocal reflectance microscope," *Applied Optics* **41**, 4603-4610 (2002).
47. R. Juskaitytis, T. Wilson, and T. F. Watson, "Real-time white light reflection confocal microscopy using a fibre-optic bundle," *Scanning* **19**, 15-19 (1997).
48. E. McCabe, "Optical Imaging Systems Irish Patent S99 0004," Irish patent, (2001).
49. H. J. a. U. Tiziani, H.M., "Three dimensional analysis by a microlens-array confocal arrangement," *Applied Optics* **33**, 567 (1994).
50. M. Eisner, N. Lindlein, and J. Schwider, "Confocal microscopy with a refractive microlens-pinhole array," *Optics Letters* **23**, 748-749 (1998).
51. H. J. Tiziani, R. Achi, R. N. Kramer, and L. Wieggers, "Theoretical analysis of confocal microscopy with microlenses," *Applied Optics* **35**, 120-125 (1996).
52. C. J. R. Sheppard, M. Gu, K. Brain, and H. Zhou, "Influence of Spherical-Aberration on Axial Imaging of Confocal Reflection Microscopy," *Applied Optics* **33**, 616-624 (1994).
53. H. J. Tiziani, and H. M. Uhde, "3-Dimensional Analysis by a Microlens-Array Confocal Arrangement," *Applied Optics* **33**, 567-572 (1994).
54. D. Feng, Y. B. Yan, G. F. Jin, and S. S. Fan, "Axial focusing characteristics of diffractive micro-lenses based on a rigorous electromagnetic theory," *Journal of Optics a-Pure and Applied Optics* **6**, 1067-1071 (2004).
55. P. Ruffieux, T. Scharf, H. P. Herzig, R. Volkel, and K. J. Weible, "On the chromatic aberration of microlenses," *Optics Express* **14**, 4687-4694 (2006).
56. T. J. A. Kippenberg, "Nonlinear Optics in Ultra-high-Q Whispering-Gallery Optical Microcavities," Thesis submitted to California Institute of Technology, (2004).
57. L. Rayleigh, "The Problem of the Whispering Gallery " *Phil. Mag.* **20**, 1001 (1910).
58. H. C. v. d. Hulst, *Light scattering : by small particles* (Dover ; Constable, New York London, 1981).
59. P. Chylek, "Partial-Wave Resonances and Ripple Structure in Mie Normalized Extinction Cross-Section," *Journal of the Optical Society of America* **66**, 285-287 (1976).
60. A. Ashkin, and J. M. Dziedzic, "Observation of Resonances in Radiation Pressure on Dielectric Spheres," *Physical Review Letters* **38**, 1351-1354 (1977).
61. P. Chylek, V. Ramaswamy, A. Ashkin, and J. M. Dziedzic, "Simultaneous Determination of Refractive-Index and Size of Spherical Dielectric Particles from Light-Scattering Data," *Applied Optics* **22**, 2302-2307 (1983).
62. R. E. Benner, P. W. Barber, J. F. Owen, and R. K. Chang, "Observation of Structure Resonances in the Fluorescence-Spectra from Microspheres," *Physical Review Letters* **44**, 475-478 (1980).
63. P. Chylek, "Resonance Structure of Mie Scattering - Distance between Resonances," *Journal of the Optical Society of America a-Optics Image Science and Vision* **7**, 1609-1613 (1990).
64. V. Sandoghdar, F. Treussart, J. Hare, V. LefevreSeguin, J. M. Raimond, and S. Haroche, "Very low threshold whispering-gallery-mode microsphere laser," *Physical Review A* **54**, R1777-R1780 (1996).
65. A. B. Matsko, and V. S. Ilchenko, "Optical resonators with whispering-gallery modes - Part I: Basics," *Ieee Journal of Selected Topics in Quantum Electronics* **12**, 3-14 (2006).
66. P. Chylek, J. T. Kiehl, and M. K. W. Ko, "Optical Levitation and Partial-Wave Resonances," *Physical Review A* **18**, 2229-2233 (1978).
67. Y. P. Rakovich, L. Yang, E. M. McCabe, J. F. Donegan, T. Perova, A. Moore, N. Gaponik, and A. Rogach, "Whispering gallery mode emission from a composite system of CdTe

- nanocrystals and a spherical microcavity," *Semiconductor Science and Technology* **18**, 914-918 (2003).
68. N. Gaponik, D. V. Talapin, A. L. Rogach, K. Hoppe, E. V. Shevchenko, A. Kornowski, A. Eychmuller, and H. Weller, "Thiol-Capping of CdTe Nanocrystals: An Alternative to Organometallic Synthetic Routes," *J. Phys. Chem. B* **106**, 7177-7185 (2002).
 69. J. Hecht, *City of light : the story of fiber optics* (Oxford University Press, New York ; Oxford, 1999).
 70. A. C. S. Vanheul, "A New Method of Transporting Optical Images without Aberrations," *Nature* **173**, 39-39 (1954).
 71. M. Wahl, F. Koberling, M. Patting, H. Rahn, and R. Erdmann, "Time-resolved confocal fluorescence imaging and spectroscopy system with single molecule sensitivity and sub-micrometer resolution," *Current Pharmaceutical Biotechnology* **5**, 299-308 (2004).
 72. D. V. O'Connor, and D. Phillips, *Time-correlated single photon counting* (Academic, London, 1984).
 73. T. K. T. Yonezawa, "Practical preparation of anionic mercapto ligand-stabilized gold nanoparticles and their immobilization," *Colloids and Surfaces* **149**, 193-199 (1999).
 74. M. C. Daniel, and D. Astruc, "Gold nanoparticles: Assembly, supramolecular chemistry, quantum-size-related properties, and applications toward biology, catalysis, and nanotechnology," *Chemical Reviews* **104**, 293-346 (2004).
 75. F. Caruso, R. A. Caruso, ouml, and H. hwald, "Nanoengineering of Inorganic and Hybrid Hollow Spheres by Colloidal Templating," *Science* **282**, 1111-1114 (1998).
 76. F. C. David I. Gittins, "Spontaneous Phase Transfer of Nanoparticulate Metals from Organic to Aqueous Media," *Angewandte Chemie International Edition* **40**, 3001-3004 (2001).
 77. V. K. Komarala, Y. P. Rakovich, A. L. Bradley, S. J. Byrne, S. A. Corr, Gun, rsquo, and Y. K. ko, "Emission properties of colloidal quantum dots on polyelectrolyte multilayers," *Nanotechnology* **17**, 4117-4122 (2006).
 78. X. Y. Wang, L. H. Qu, J. Y. Zhang, X. G. Peng, and M. Xiao, "Surface-related emission in highly luminescent CdSe quantum dots," *Nano Letters* **3**, 1103-1106 (2003).
 79. D. K.H., "Progress in Optics XII," (1974).
 80. V. K. Komarala, "Metal surface enhanced emission from CdTe quantum dots," *Proceedings of SPIE* **5955**, (2005).
 81. J. H. Song, T. Atay, S. F. Shi, H. Urabe, and A. V. Nurmikko, "Large enhancement of fluorescence efficiency from CdSe/ZnS quantum dots induced by resonant coupling to spatially controlled surface plasmons," *Nano Letters* **5**, 1557-1561 (2005).
 82. T. W. Ebbesen, H. J. Lezec, H. F. Ghaemi, T. Thio, and P. A. Wolff, "Extraordinary optical transmission through sub-wavelength hole arrays," *Nature* **391**, 667-669 (1998).
 83. S. A. Maier, "Plasmonics - A Route to Nanoscale Optical Devices," *Advanced Materials* **13**, 1501-1505 (2001).
 84. E. Ozbay, "Plasmonics: Merging Photonics and Electronics at Nanoscale Dimensions," *Science* **311**, 189-193 (2006).
 85. W. L. Barnes, A. Dereux, and T. W. Ebbesen, "Surface plasmon subwavelength optics," *Nature* **424**, 824-830 (2003).
 86. S. W. Hell, and J. Wichmann, "Breaking the Diffraction Resolution Limit by Stimulated-Emission - Stimulated-Emission-Depletion Fluorescence Microscopy," *Optics Letters* **19**, 780-782 (1994).
 87. K. L. Kelly, E. Coronado, L. L. Zhao, and G. C. Schatz, "The optical properties of metal nanoparticles: The influence of size, shape, and dielectric environment," *Journal of Physical Chemistry B* **107**, 668-677 (2003).
 88. N. Halas, "Playing with Plasmons: Tuning the Optical Resonant Properties of Metallic Nanoshells," *MRS BULLETIN* **30**, 362 (2005).

89. E. Dulkeith, A. C. Morteani, T. Niedereichholz, T. A. Klar, J. Feldmann, S. A. Levi, F. C. J. M. van Veggel, D. N. Reinhoudt, M. MÄ¶ller, and D. I. Gittins, "Fluorescence Quenching of Dye Molecules near Gold Nanoparticles: Radiative and Nonradiative Effects," *Physical Review Letters* **89**, 203002 (2002).